ORNL/

Stress Analysis of Cylindrical Pressure Vessels with Closely Spaced Nozzles by the Finite-Element Method

Volume 1. Stress Analysis of Vessels with Two Closely Spaced Nozzles Under Internal Pressure

F. K. W. Tso
J. W. Bryson
R. A. Weed
S. E. Moore

MASTER

for the U.S. Nuclear Regulatory Com
of Nuclear Regulatory Resea
Interagency Agreement
-551-75 and 40-55

ORNL/NUREG-18/V1
Dist. Category NRC-5

Contract No. W-7405-eng-26

Engineering Technology Division

STRESS ANALYSIS OF CYLINDRICAL PRESSURE VESSELS WITH CLOSELY SPACED NOZZLES BY THE FINITE-ELEMENT METHOD

Volume 1. Stress Analysis of Vessels with Two Closely Spaced Nozzles Under Internal Pressure

F. K. W. Tso R. A. Weed
System Development Corporation

J. W. Bryson S. E. Moore
Oak Ridge National Laboratory

Manuscript Completed — October 4, 1977
Date Published — November 1977

Prepared for the
U.S. Nuclear Regulatory Commission
Office of Nuclear Regulatory Research
under Interagency Agreements
ERDA 40-551-75 and 40-552-75

Prepared by
OAK RIDGE NATIONAL LABORATORY
Oak Ridge, Tennessee 37830
operated by
UNION CARBIDE CORPORATION
for the
DEPARTMENT OF ENERGY

CONTENTS

BLANK PAGE

FOREWORD

The work reported here was performed at the Oak Ridge National Laboratory (ORNL) and at System Development Corporation (formerly Mechanics Research, Inc.) under Union Carbide Corporation, Nuclear Division, Subcontract No. 7012 with consulting assistance from Profs. G. H. Powell and D. P. Mondkar at the University of California, Berkeley. This work is in support of the ORNL Design Criteria for Piping and Nozzles Program being conducted for the U.S. Nuclear Regulatory Commission (USNRC), Office of Nuclear Regulatory Research. E. K. Lynn of the Metallurgy and Materials Branch, Division of Reactor Safety Research, USNRC, is the cognizant RSR engineer, and S. E. Moore of ORNL, Division of Engineering Technology (formerly Reactor Division) is the program manager.

The objectives of the ORNL program are to conduct integrated experimental and analytical stress analysis studies of piping system components and pressure vessel nozzles in order to confirm and/or improve the adequacy of structural design criteria and analytical methods used to assure the safe design of nuclear power plants. Activities under the program are coordinated with other safety-related piping and pressure vessel research through the Design Division, Pressure Vessel Research Committee (PVRC) of the Welding Research Council, and through the ASME Boiler and Pressure Vessel Code Committees. Results from the ORNL program are used by appropriate codes and standards groups in drafting new or improved design rules and criteria.

The following reports have been issued under U.S. Nuclear Regulatory Commission sponsorship:

J. W. Bryson, J. P. Callahan, and R. C. Gwaltney, *Stress Analyses of Flat Plates with Attached Nozzles, Vol. 1. Comparison of Stresses in a One-Nozzle-to-Flat-Plate Configuration and in a Two-Nozzle Configuration with Theoretical Predictions*, ORNL-5044, Vol. 1 (July 1975).

R. L. Battiste, W. H. Peters, W. F. Ranson, and W. F. Swinson, *Stress Analysis of Flat Plates with Attached Nozzles, Vol. 2. Experimental Stress Analyses of a Flat Plate with One Nozzle Attached*, ORNL-5044, Vol. 2 (July 1975).

E. C. Rodabaugh and S. E. Moore, *Stress Indices for ANSI Standard B16.11 Socket-Welding Fittings*, ORNL/TM-4929 (August 1975).

R. C. Gwaltney, J. W. Bryson, and S. E. Bolt, *Theoretical and Experimental Stress Analyses of ORNL Thin-Shell Cylinder-to-Cylinder Model 2*, ORNL-5021 (October 1975).

S. E. Moore, "Contributions of the ORNL Piping Program to Nuclear Piping Design Codes and Standards," *Proceedings of the Technology Information Meeting on Methods for Analyzing Piping Integrity, Nov. 11-12, 1975*, ERDA 76-50; also in *J. Press. Vessel Technol., Trans. ASME* 99, 224-30 (February 1977).

W. L. Greenstreet, "Summary and Accomplishments of the ORNL Program for Nuclear Piping Design Criteria," *Proceedings of the Technology Information Meeting on Methods for Analyzing Piping Integrity, Nov. 11-12, 1975*, ERDA 76-50.

J. W. Bryson and W. F. Swinson, *Stress Analyses of Flat Plates with Attached Nozzles, Vol. 3. Experimental Stress Analyses of a Flat Plate with Two Closely Spaced Nozzles of Equal Diameter Attached*, ORNL-5044, Vol. 3 (December 1975).

E. C. Rodabaugh, F. M. O'Hara, Jr., and S. E. Moore, *FLANGE: A Computer Program for the Analysis of Flanged Joints with Ring-Type Gaskets*, ORNL-5035 (January 1976).

R. E. Textor, *User's Guide for SHFA: Steady-State Heat Flow Analysis of Tee Joints by the Finite Element Method*, UCCND/CSD/INF-60, Oak Ridge Gaseous Diffusion Plant (January 1976).

E. C. Rodabaugh and S. E. Moore, *Flanged Joints with Contact Outside the Bolt Circle – ASME Part B Design Rules*, ORNL/Sub/2913-1, Battelle-Columbus Laboratories (May 1976).

E. C. Rodabaugh, *Appropriate Nominal Stresses for Use with ASME Code Pressure-Loading Stress Indices for Nozzles*, ORNL/Sub/2913-2, Battelle-Columbus Laboratories (June 1976).

S. E. Moore and J. W. Bryson, *Progress Report for the Design Criteria for Piping and Nozzles Program for the Two Quarterly Periods July 1 to Sept. 30 and Oct. 1 to Dec. 31, 1975*, ORNL/NUREG/TM-18 (June 1976).

R. L. Maxwell and R. W. Holland, *Experimental Stress Analysis of the Attachment Region of a Hemispherical Shell with a Radially Attached Nozzle, Zero Penetration*, ORNL/Sub/2203-4, University of Tennessee (July 1976).

J. P. Callahan and J. W. Bryson, *Stress Analyses of Perforated Flat Plates Under In-Plane Loadings*, ORNL/NUREG-2 (August 1976).

E. C. Rodabaugh and S. E. Moore, *Evaluation of the Bolting and Flanges of ANSI B16.5 Flanged Joints — ASME Part A Flanges*, ORNL/Sub/2913-3, Battelle-Columbus Laboratories (September 1976).

E. C. Rodabaugh and R. C. Gwaltney, *Elastic Stresses at Reinforced Nozzles in Spherical Shells with Pressure and Moment Loading*, ORNL/Sub/2913-4 (October 1976).

E. C. Rodabaugh, S. E. Moore, and J. N. Robinson, *Dimensional Control of Buttwelding Pipe Fittings for Nuclear Power Plant Class 1 Piping Systems*, ORNL/Sub/2913-5 (December 1976).

S. E. Moore and J. W. Bryson, *Design Criteria for Piping and Nozzles Program Quarterly Progress Report for April-June 1976*, ORNL/NUREG/TM-107 (April 1977).

E. C. Rodabaugh and S. E. Moore, *Flexibility Factors for Small (d/D < 1/3) Branch Connections with External Loadings*, ORNL/Sub/2913-6 (March 1977).

S. E. Moore and J. W. Bryson, *Design Criteria for Piping and Nozzles Program Quarterly Progress Report for July-September 1976*, ORNL/NUREG/TM-91 (February 1977).

P. G. Fowler and J. W. Bryson, *User's Manual for the CORTES Graphics Package GRFPAK*, ORNL/NUREG/TM-127 (August 1977).

B. R. Bass, J. W. Bryson, and S. E. Moore, "Validation of the Finite Element Stress Analysis Computer Program CORTES-SA for Analyzing Piping Tees and Pressure Vessel Nozzles," *Pressure Vessels and Piping Computer Program Evaluation and Qualification*, PVP-PB-024, pp. 9-25, ASME (1977).

J. K. Hayes and S. E. Moore, "Experimental Stress Analysis for Four 24-in. ANSI Standard B16.9 Tees," Paper 77-PVP-4, presented at the ASME Energy Technology Conference and Exhibition, Houston, Texas, Sept. 18-23, 1977.

J. W. Bryson, W. G. Johnson, and B. R. Bass, *Stresses in Reinforced Nozzle-Cylinder Attachments Under Internal Pressure Loading Analyzed by the Finite-Element Method — A Parameter Study*, ORNL/NUREG-4 (October 1977).

STRESS ANALYSIS OF CYLINDRICAL PRESSURE VESSELS WITH CLOSELY SPACED NOZZLES BY THE FINITE-ELEMENT METHOD

Volume 1. Stress Analysis of Vessels with Two Closely Spaced Nozzles Under Internal Pressure

F. K. W. Tso R. A. Weed
System Development Corporation

J. W. Bryson S. E. Moore
Oak Ridge National Laboratory

ABSTRACT

A finite-element computer program, MULT-NOZZLE, was developed for the stress analysis of cylindrical pressure vessels with two or three closely spaced reinforced nozzles. MULT-NOZZLE consists of two modules which may be operated independently. The first module, FEMG, automatically prepares a finite-element mesh including the nodal point coordinates, finite-element connectivities, mesh options, and boundary value specifications for input to the finite-element solution module SAP3M. SAP3M, which is a modified and improved version of the SAP3 computer program, computes the nodal point displacements and stress tensor components, and prints and/or stores the results for later postprocessing. The accuracy of the SAP3M module is demonstrated by comparison studies of two classical theory-of-elasticity problems: a simply supported beam and a thick-walled ring under internal pressure loading.

A complete discussion of MULT-NOZZLE is presented in four volumes. The present volume develops the finite-element idealization for pressure vessels with two identical radially attached closely spaced nozzles for internal pressure loading. The nozzles may be unreinforced or fully reinforced accordding to the rules of the ASME Boiler and Pressure Vessel Code and may be located in either a longitudinal or a transverse plane of the vessel. Validation of the program for analyzing this type of structure is demonstrated by the analysis of three two-nozzle pressure vessel models and comparison of results with experimental data. In general, quite satisfactory results were obtained.

Volumes 2, 3, and 4 (to be published later) discuss the analysis of two-nozzle vessels with external loadings on the nozzles, three-nozzle vessels with internal pressure loading, and input instructions and operating procedures for the programs.

Keywords: stress analysis, pressure vessels, pressure vessel nozzles, ASME BPVC, design criteria, design rules, ORNL Piping and Nozzles Program, nozzle analysis

BLANK PAGE

1. INTRODUCTION

Essentially all current generation nuclear power plant pressure vessels have working fluid penetrations in the cylindrical portion of the vessel which must be designed according to the rules of the ASME Boiler and Pressure Vessel Code, Section III, Div. 1, for Nuclear Power Plant Components.*[1] According to these rules, the pressure vessel penetrations (i.e., "nozzles") must satisfy a set of clearly defined structural safety criteria. The Code design criteria include minimum reinforcement requirements, maximum stress requirements, and instructions for calculating stresses under the various loading conditions expected during the life of the vessel.

The Code rules have evolved over a number of years and are adequate for most design situations. However, questions have recently been raised on two specific issues. These concern maximum calculated stresses for nozzles that are reinforced according to the Code rules given in NB-3330 and for nozzles spaced "close" together. As pointed out by Mershon and Rodabaugh[2] in a preliminary evaluation of the Code rules, insufficient information, either analytical or experimental, is currently available to properly support a "rule" governing how close two or more nozzles may be placed without exceeding established safe maximum stress limits. Indeed, the present rule, which distinguishes between "isolated" and "closely spaced" nozzles, is rather poorly supported by sound technical information. There is evidence that, under some design conditions, nozzles may be safely placed closer than presently permitted while for other conditions the opposite may be true.

The studies discussed here, as well as in subsequent volumes of this report,[3-5] were undertaken to develop and validate a finite element computer program capable of analyzing cylindrical pressure vessels with two or three closely spaced nozzles for internal pressure and/or externally applied pipe reaction or support-type loadings. The present volume is concerned with the stress analysis of vessels with two identical radially

*For brevity, "Code" will refer to Section III, Div. 1, of the ASME Boiler and Pressure Vessel Code (Ref. 1). Specific portions of the Code are referred to by the appropriate code designation (e.g., NB-3300).

attached nozzles for internal pressure loading. The nozzles may be unreinforced, may have fillet radius reinforcement, or may be fully reinforced with one of the standard ASME configurations illustrated in Fig. NB-3338.2-2 and shown here as Fig. 1.1.

Volume 2 of this report is also concerned with the stress analysis of cylindrical pressure vessels with two identical nozzles but with force and moment loadings applied through the nozzles. Volume 3 will consider three nozzles and internal pressure. Volume 4 will contain a complete set of user instructions for operating the computer program MULT-NOZZLE. We plan to use this computer program to develop sufficient stress analysis information to properly assess the current Code design qualification rules and

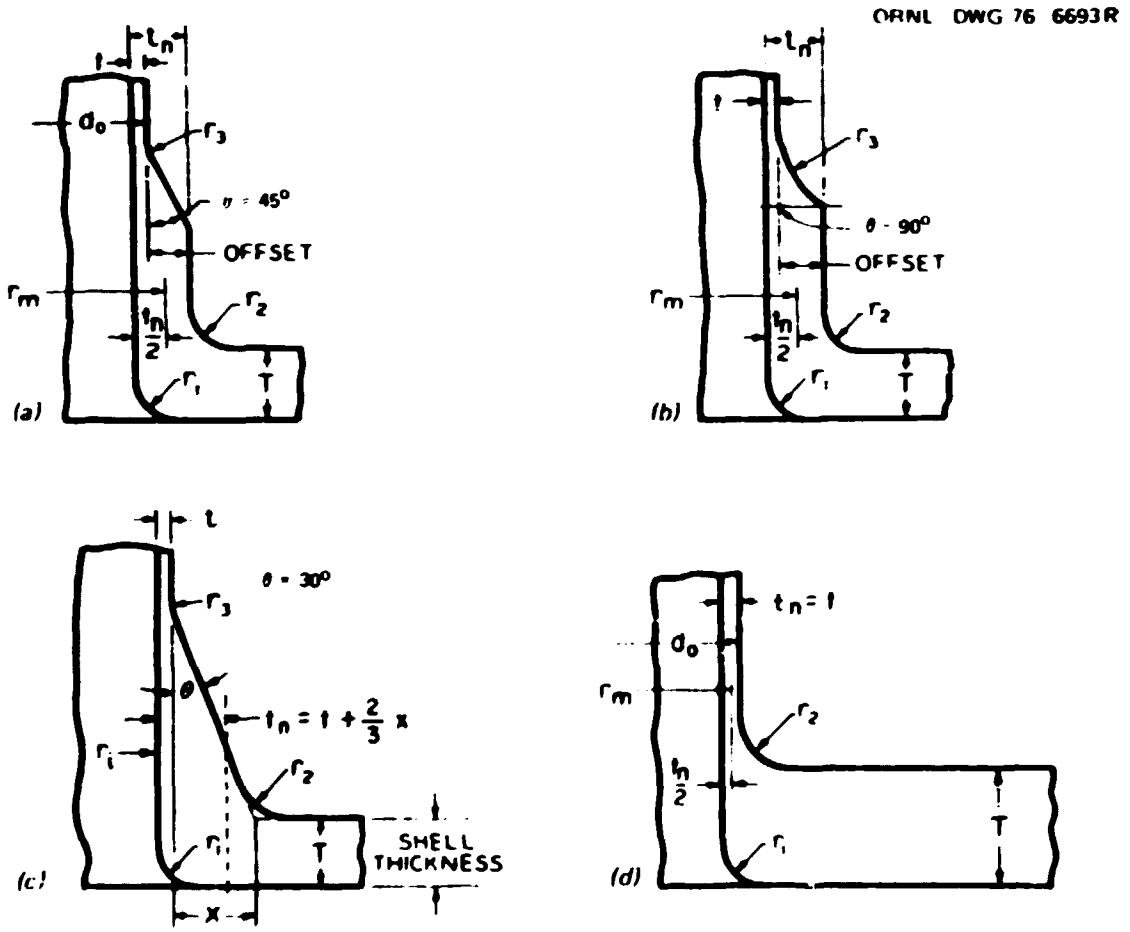

Fig. 1.1. Nozzle configurations for various ASME standard reinforcement designs.

to support proposed modifications to the rules in answer to the questions posed earlier.

The computer program MULT-NOZZLE is capable of analyzing cylindrical pressure vessels with a single nozzle or with two or three nozzles spaced arbitrarily close together, subject to the restrictions discussed in the next chapter for two nozzles and in volume 3 for three nozzles. The program is capable of automatically generating a suitable finite-element model composed entirely of hexahedral elements. Isoparametric solid brick-type elements, which may have from 8 to 21 nodes each, are used throughout. The program computes stresses, strains, and nodal point displacements that may be saved along with the mesh geometry for later postprocessing (i.e., the preparation of grid plots, selected output formatting, etc.).

MULT-NOZZLE consists of two major parts or modules that may be operated independently. The first, FEMG (Finite-Element Mesh Generator), automatically prepares a finite-element mesh including the nodal point coordinates, finite-element connectivities, mesh options, and boundary value specifications for input to the finite-element solution module. FEMG, discussed in the next chapter, uses many of the features of an existing program (HSST-NODES) developed earlier by Krishnamurthy[6] to generate finite-element models for thick-walled nozzle-vessel structures. All the input data required by FEMG can be specified on fewer than 15 data cards.

Stresses and nodal point displacements are calculated using a modified and improved version of the SAP3 finite-element program, originally developed by Wilson[7] at the University of California. SAP3M computes nodal point displacements and the stress tensor components at specified data points for the entire finite-element model. The stress components, in the global Cartesian coordinate system, are calculated initially at the second-order Gaussian integration points and then extrapolated to the node points (or any other set of specified points in the element) using a bilinear local smoothing scheme proposed by Hinton and Campbell.[8] At present, SAP3M contains only the variable 8- to 21-node solid isoparametric hexahedral finite element.[9,10] This element enables modeling the structure with a high element density in regions of high stress gradients

and a lower element density in regions of more uniform stresses. SAP3M also contains an improved and more efficient matrix equation solution routine developed by Mondkar and Powell.[11,12]

Application of MULT-NOZZLE is demonstrated in this report by analyzing five models: two classical problems — a simply supported beam in plane strain bending and a thick-walled ring loaded with internal pressure — and three two-nozzle cylindrical pressure vessel configurations for internal pressure loading. Validation of the program accuracy is demonstrated by comparison of the calculated results with theoretical solutions[13,14] and with experimental data.[15,16]

The basic assumptions and mathematical formulations used for the automatic finite-element mesh generation are discussed briefly in the next chapter. Chapter 3 contains a discussion of the finite-element theory and solution algorithms employed in MULT-NOZZLE. Studies of the two classical problems for validating the SAP3M finite element-module are presented in Chap. 4. Chapter 5 presents the analysis of a relatively thick-walled pressure vessel with two closely spaced nozzles located in a longitudinal plane and includes comparisons with experimental results. Chapter 6 gives similar results for a thin-walled two-nozzle pressure vessel.

The analysis of a two-nozzle vessel configuration with the nozzles located in a circumferential plane is presented in Chap. 7. The results predicted in this volume of the report are summarized and discussed in Chap. 8. Throughout the verification sections of the report, results of the stress calculations are presented graphically. Numerical values shown in these graphs are presented in tabular form in the appendix.

2. FINITE-ELEMENT MESH GENERATION

Generation of the finite-element model for analyzing a three-dimensional double-nozzle junction in a cylindrical pressure vessel would be difficult and time consuming if performed manually and would be virtually impossible for conducting parameter studies. Therefore, an automated mesh generator and input data preparation module, FEMG (Finite-Element-Model Generation), was developed. The basic assumptions, terminology, and mathematical formulas for constructing the finite-element model for two-nozzle cylindrical pressure vessel analyses are discussed in this chapter. The finite-element model for a single-nozzle vessel is a special case of the two-nozzle model and consequently will not be discussed separately. The model for three-nozzle problems is discussed in volume 3 (Ref. 4).

2.1 Basic Considerations

The basic assumptions for automated construction of finite-element models for two-nozzle pressure vessels are as follows:

1. The two nozzles are geometrically identical.
2. The nozzle configurations are either unreinforced or fully reinforced, as illustrated in Figs. NB-3338.2-2 (a) through (d) of Section III of the *ASME Boiler and Pressure Vessel Code*[1] (shown earlier in Fig. 1.1).
3. The nozzles are radially attached to the cylindrical vessel and are positioned either on a longitudinal plane or on a transverse (circumferential) plane.
4. The models may or may not have inner and/or outer surface transitions (r_1 and r_2 of Fig. 1.1) between the vessel and nozzle.
5. The transitions are circular arcs; i.e., r_1 and r_2 are constants and connect tangentially with the cylindrical vessel and a cylindrical nozzle.
6. For pad reinforcement, Fig. 1.1(*c*), $r_2 \equiv 0.0$.

The two-nozzle configuration has two planes of symmetry, one through the centerlines of the two nozzles and one midway between the two nozzles as shown in Fig. 2.1. The symmetric-quadrant model for the nozzle-cylinder

ORNL-DWG 77-12937

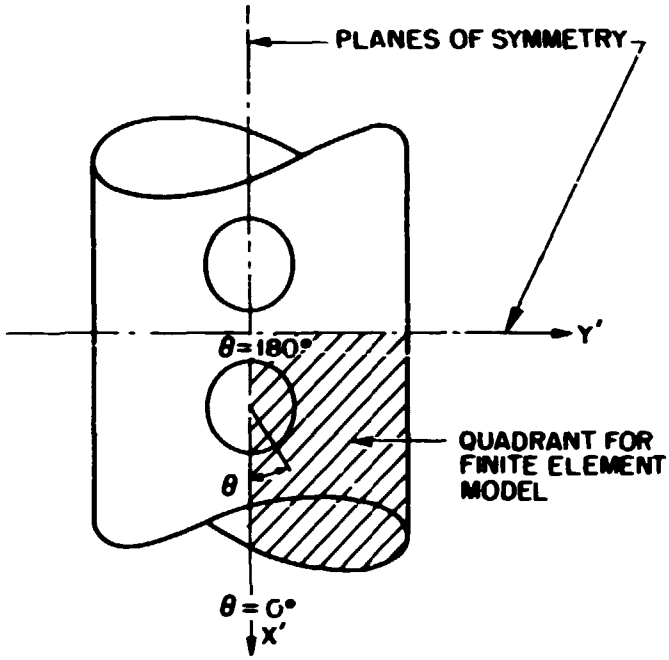

(a) TWO NOZZLES ON A LONGITUDINAL PLANE

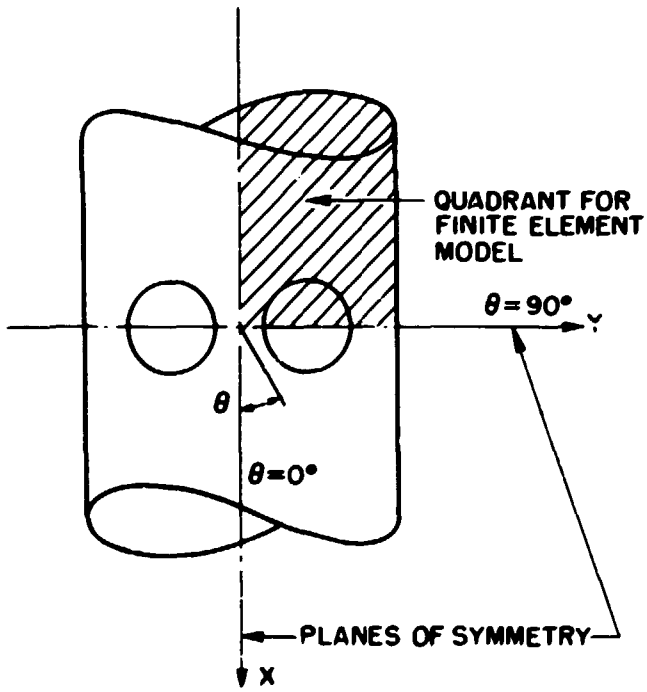

(b) TWO NOZZLES ON A CIRCUMFERENTIAL PLANE

Fig. 2.1. Two-nozzle configuration layout.

junction in which the nozzles are longitudinally aligned is shown in Fig. 2.2. A similar one-quarter model is used in the analyses of the circumferential configuration as shown in Fig. 2.3. The one-quarter model is then idealized by dividing it into a three-dimensional array of elements, calculating coordinate values for each of the nodes in that array, and defining the connectivity of the elements.

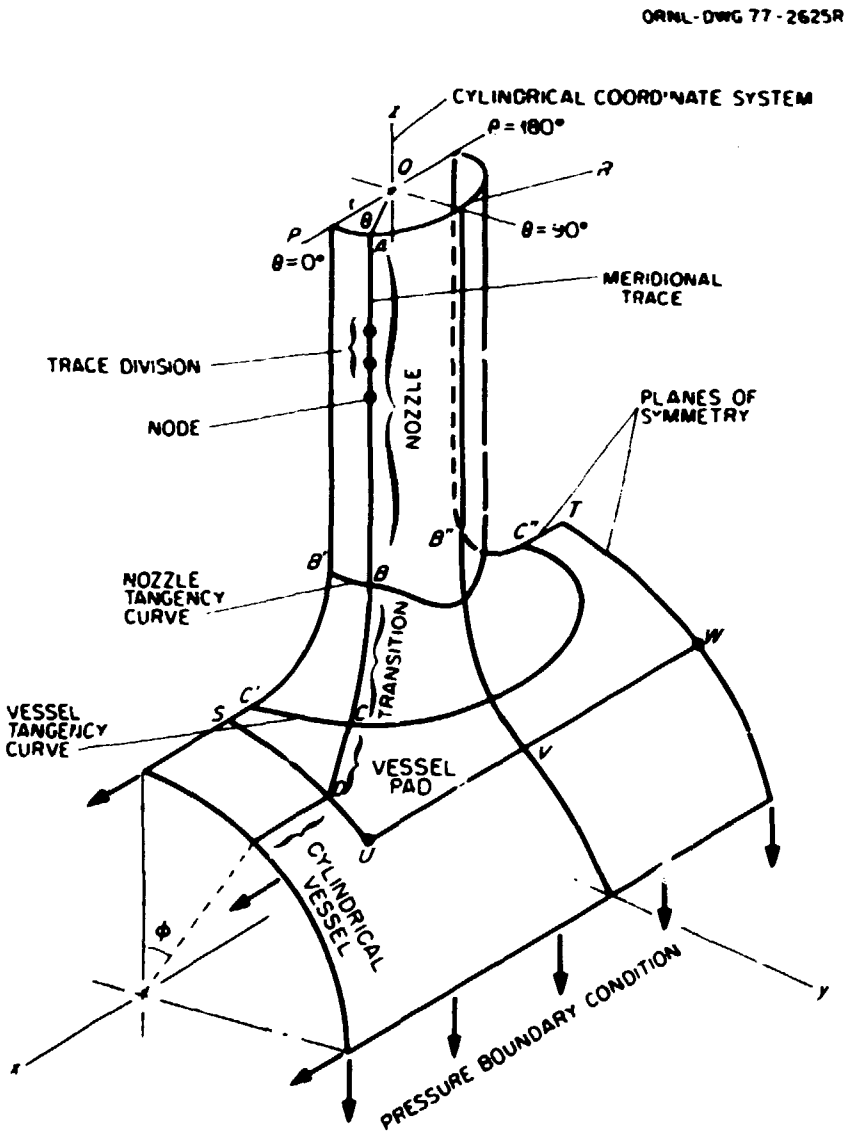

Fig. 2.2. Symmetric quadrant for the longitudinal two-nozzle configuration.

ORNL-DWG 77-12936

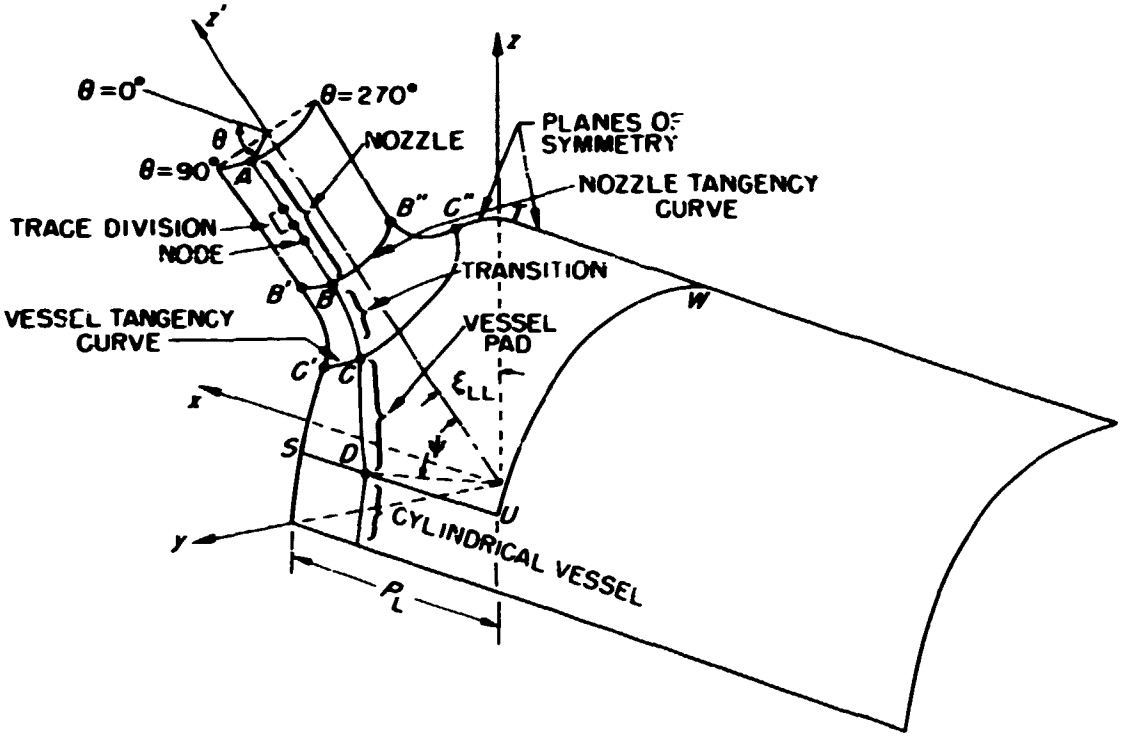

Fig. 2.3. Symmetric quadrant for the circumferential two-nozzle configuration.

2.2 Terminology of Mesh Generation

The ensuing discussion involves frequent reference to the geometry and topology of the junction. To maintain a concise and consistent terminology, the following special definitions and conventions will be used.

For the longitudinal model shown in Fig. 2.2, the z-axis of the reference global Cartesian coordinate system is along the centerline of the nozzle. The x-axis is along the centerline of the vessel, and the y-axis is perpendicular to the intersection of the two centerlines. Angles around the z-axis are defined by the variable θ, with $\theta = 0$ and 180° lying in the x-z (longitudinal) plane. The outboard side of the nozzle is in

the longitudinal plane at $\theta = 0°$ and the inboard side is at $\theta = 180°$, between the two nozzles.

Radial planes, identified by the angle θ, are perpendicular to the x-y plane and include the nozzle centerline. The radial plane at $\theta = 90°$ is called the transverse plane.

Several different surfaces are identified with respect to the model. These include the inner surface, intermediate surfaces, outer surface, and various cross sections. The line formed by the intersection between a radial plane and a model surface is called a meridional trace, or simply a trace. The line ABCD in Fig. 2.2 is a typical meridional trace marked into divisions by nodes. The cross section formed by a radial plane and the inner and outer model surfaces is called a meridional section. The regions between the model surfaces are called layers.

Each model surface is identified by four geometrically distinct zones: (1) the nozzle, which may be further divided into as many as three regions depending on the reinforcement details shown earlier in Fig. 1.1; (2) the circular transition zone, which may be absent if the nozzle is not reinforced or if pad reinforcement is used; (3) the vessel pad; and (4) the cylindrical vessel. At present, the wall thicknesses of the model in the pad and vessel zones must be equal. These two zones are distinguished only by the coordinate system used to lay out the finite-element mesh.

The boundary between the nozzle and transition zones, shown as the line $B'B''$ in Fig. 2.2, is the nozzle tangency curve. The vessel tangency curve is the boundary between the transition zone and the vessel pad ($C'C''$ in Fig. 2.2). These two tangency curves form the natural topological boundaries between the three zones of the nozzle intersection region. A cylindrical (r,θ,z) coordinate system referenced to the nozzle is used in this region to define the finite-element mesh layout. The finite-element mesh layout for the vessel zone is referenced to the r,ϕ,x coordinates of the vessel, where ϕ is the angle from the x-z plane as shown in Fig. 2.2.

A similar conceptualization and terminology is used for the circumferentially spaced nozzle model illustrated in Fig. 2.3, except that the centerline of the nozzle (z' axis) is displaced from the global z axis by the angle ξ_{LL} in the y-z plane.

2.3 Finite-Element Idealization

The mathematical basis for the finite-element mesh, developed automatically by FEMG for two closely spaced nozzle problems, is discussed in this section. A suitable mesh is characterized as consisting entirely of solid hexahedral isoparametric elements with 8 to 16 node points on their surface edges. In the nozzle, transition, and vessel pad zones, every node point will lie on one of the model surfaces formed by dividing the wall thickness into layers and on one of the meridional traces formed by the intersection of a radial plane with the model surfaces. In the vessel region, the nodes lie on one of the model surfaces and on trace line extensions either along the vessel or around the circumference of the vessel.

FEMG considers each surface independently and determines coordinate locations for a preliminary fine-mesh layout for the entire model. Under option control, FEMG then systematically selects or skips nodes for assignment to the elements and constructs the final variable density finite element model, complete with element connectivities.

2.3.1 Equations for a meridional trace

Consider a typical meridional trace defined by a radial plane intersection with one of the model surfaces as shown in Figs. 2.4 and 2.5. Let (r,θ,z) or (r',θ,z') be the set of cylindrical coordinates for the nozzle with its origin at the intersection of the vessel and nozzle axes. In the following, no distinction will be made between (r,θ,z) and (r',θ,z') except where it is necessary to discuss the two types of models separately.

The equation for the meridional trace in the vessel pad region (the line CD in Fig. 2.6) may be written as

$$\frac{r^2}{a^2} + \frac{z^2}{b^2} = 1 \ , \qquad (2.1)$$

where a is the semimajor axis of the ellipse and b is the semiminor axis. For both the longitudinal and circumferential nozzle models, the values of

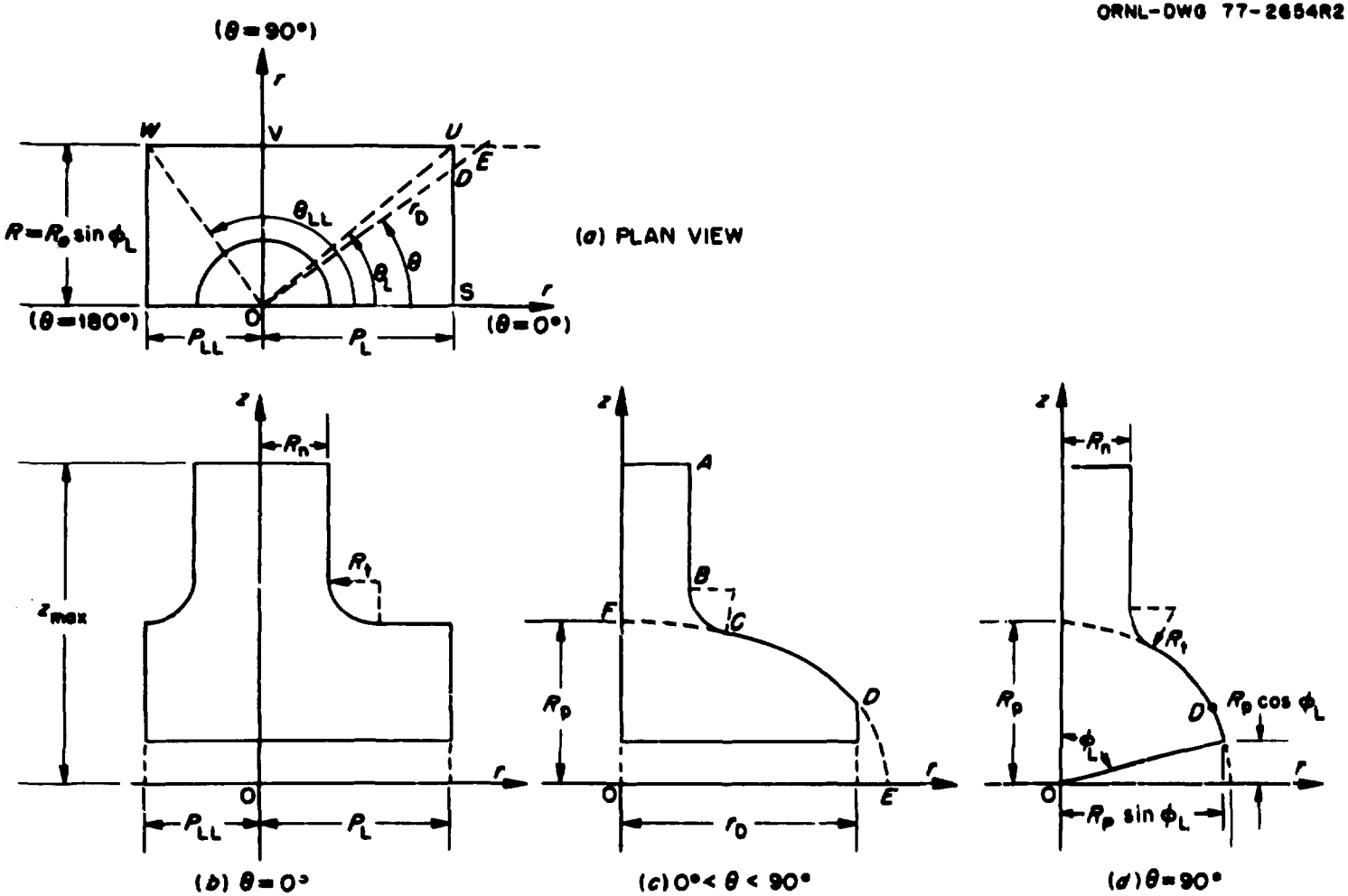

Fig. 2.4. Plan view and typical radial plane intersections (meridional traces) for two nozzles in the longitudinal plane of the vessel.

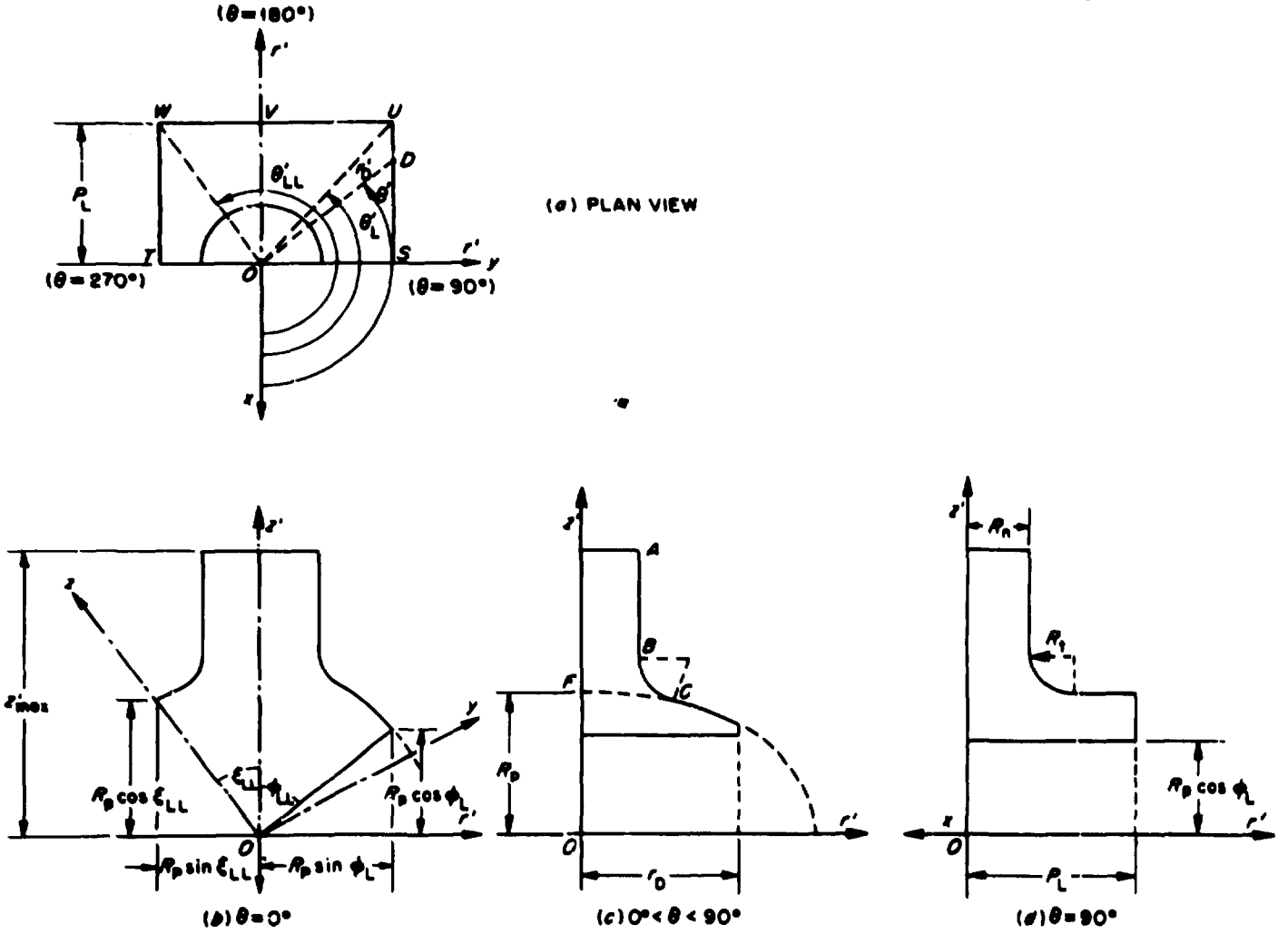

Fig. 2.5. Plan view and typical radial plane intersections (meridional traces) for two nozzles in the circumferential plane of the vessel.

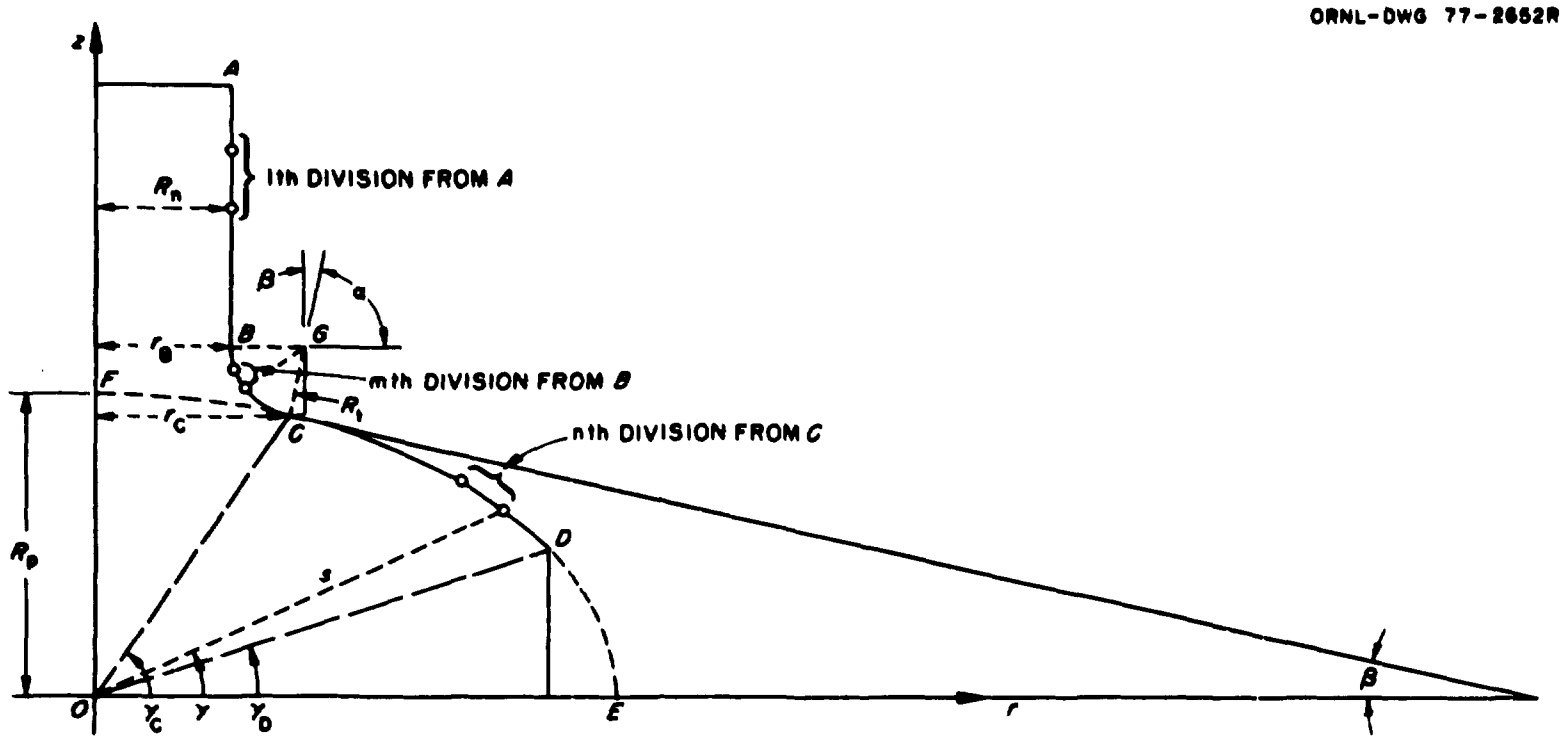

Fig. 2.6. Elevation view of a typical meridional trace.

a and b are

$$a = R_p/\sin\theta \ ,$$
$$b = R_p \ , \tag{2.2}$$

where R_p is the radius to the vessel surface under consideration.

Substituting Eq. (2.2) into Eq. (2.1), the equation for the elliptical curve becomes

$$r^2\sin^2\theta + z^2 = R_p^2 \ . \tag{2.3}$$

To locate the vessel tangency point C, consider the equality

$$\sin\beta = (R_n + R_t - r_C)/R_t \ , \tag{2.4}$$

where R_n is the radius to the nozzle surface under consideration, R_t is the radius of the transition, and r_C is the radial distance from the nozzle axis to the point C.

Furthermore, using Eq. (2.3), the expression for the slope of the trace at C may be written as

$$\tan\beta = -\left.\frac{dz}{dr}\right|_{r=r_C} = \frac{r_C \sin^2\theta}{(R_p^2 - r_C^2 \sin^2\theta)^{1/2}} \ . \tag{2.5}$$

Also,

$$\sin\beta = \frac{r_C \sin^2\theta}{[R_p^2 - r_C^2 (\sin^2\theta \cos^2\theta)]^{1/2}} \ . \tag{2.6}$$

When the values of $\sin\beta$ given by Eqs. (2.4) and (2.6) are set equal, the equation for the unknown, r_C, is

$$A r_C^4 + B r_C^3 + C r_C^2 + D r_C + E = 0 \ , \tag{2.7}$$

where

$$A = -\sin^2\theta \cos^2\theta \ ,$$
$$B = -2A(R_n + R_t) \ ,$$

$$C = A(R_n + R_t)^2 + R_p^2 - R_t^2 \sin^4 \theta \ ,$$

$$D = -2R_p^2 \ (R_n + R_t) \ ,$$

$$E = R_p^2 (R_n + R_t)^2 \ .$$

Equation (2.7) may be conveniently solved for r_C to the desired precision by numerical techniques. Here, the Newton-Raphson iteration method was used.

The z-coordinate of the vessel tangency point C for any meridional trace θ is obtained from

$$z_C = (R_p^2 - r_C^2 \sin^2\theta)^{1/2} \ . \tag{2.8}$$

Equations (2.7) and (2.8) give the coordinates of the vessel tangency point C for any meridional trace. For the nozzle tangency point (point B of Fig. 2.6) we have

$$r_B = R_n \ ; \tag{2.9}$$

and using Eq. (2.4) to define the angle β,

$$\begin{aligned} z_B &= z_C + R_t \cos \beta \\ &= z_C + [2R_t \ (r_C - R_n) - (r_C - R_n)^2]^{1/2} \ . \end{aligned} \tag{2.10}$$

With the value of r_C determined from Eq. (2.7), the coordinate locations for the tangency points B and C are defined by Eqs. (2.8) to (2.10).

2.3.2 Determination of nodal coordinates

Assume that the nozzle, transition, and vessel-pad portions of the trace are divided into L, M, and N parts, respectively, by node points. There will then be $L + M + N + 1$ nodes on the trace, i.e., one more than the total number of divisions.

For an unreinforced nozzle divided into L parts, like the one depicted earlier in Fig. 1.1(d) and in Fig. 2.6, the coordinates for the

node at the end of the ith division are

$$r = R_n \ ,$$
$$z = z_A - (z_A - z_B)(i/L)^{c_1} \ , \tag{2.11}$$

where z_A and z_B are the axial coordinates for the points A and B shown in Fig. 2.6 and c_1 is a node point crowding index for the nozzle.

If the nozzle is reinforced, like those shown earlier in Figs. 1.1(a), (b), and (c) and in Fig. 2.7, the nozzle will be further divided into two parts by L_1 divisions above the reinforcement and L_2 divisions in the reinforcement above the circular transition. Note that the number of trace divisions on the nozzle will vary from surface to surface for reinforced nozzles. This is illustrated in Fig. 2.7 on a five-layer example.

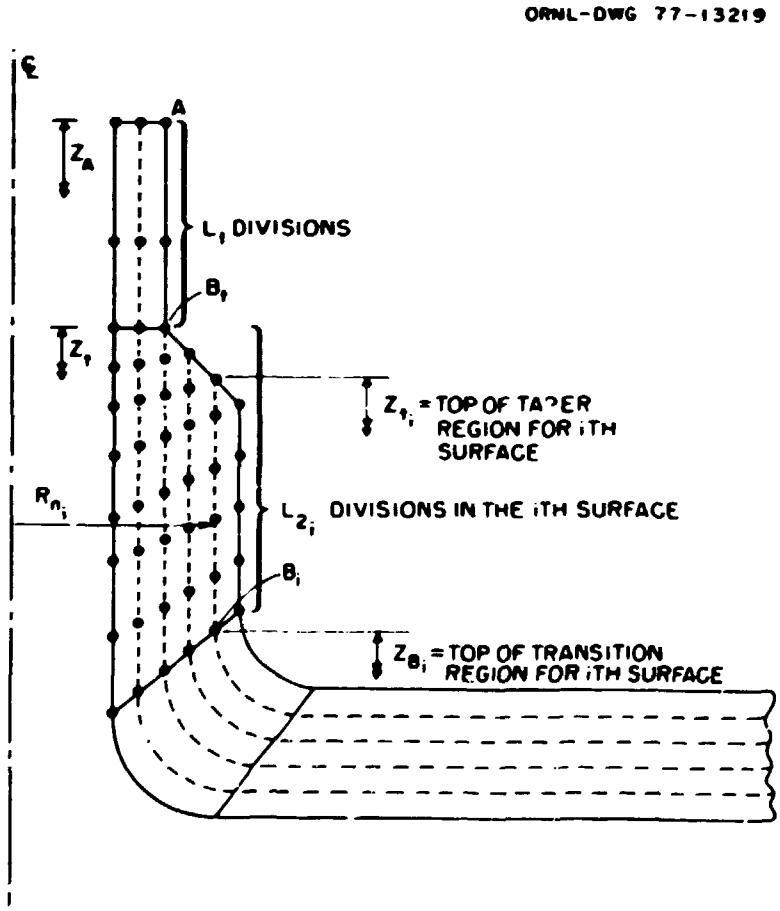

Fig. 2.7. Node identification for reinforcement nozzles.

Since the maximum value of z for each layer is input to FEMG independently, it is possible to define a straight taper as in Figs. 1.1(a) and 1.1(c) or a curved taper as in Fig. 1.1(b). If a curved taper is being modeled, the trace is approximated by a series of straight chord segments. For each surface the coordinates for nodes above the taper are

$$r = R_n \ ,$$
$$z = z_A - (z_A - z_T)(\ell_1/L_1)^{c_1} \ ; \qquad \ell_1 = 1 \text{ to } L_1 \ , \tag{2.12}$$

where z_T is the axial coordinate to the top of the taper. Between the top of the taper and the top of the circular transition, the node coordinates are

$$r = R_n \ ,$$
$$z = z_t - (z_t - z_B)(\ell_2/L_2) \ ; \qquad \ell_2 = 1 \text{ to } L_2 \ , \tag{2.13}$$

where $z_t \leq z_T$ is measured to the top of the taper region for the ith surface, as shown in Fig. 2.7. R_n is the radius to the ith surface.

For the nozzle-vessel transition region, the coordinates for the node at the end of the mth division are

$$r = R_n + R_t \ [1 - \cos(m/M)\alpha] \ ,$$
$$z = z_B - R_t \sin \ (m/M)\alpha \ , \tag{2.14}$$

where R_t is the transition radius and the angle α, subtended by the arc BGC in Fig. 2.6, is defined by

$$\alpha = \sin^{-1} \ [(z_B - z_C)/R_t] \ . \tag{2.15}$$

The nodal coordinates in the vessel pad zone at the end of the nth division are

$$r = s \cos \gamma \ ,$$
$$z = s \sin \gamma \ , \tag{2.16}$$

where s is the polar distance to the node and can be evaluated from Eqs.

(2.1), (2.2), and (2.16) as

$$s = R_p/(\sin^2\gamma + \cos^2\gamma \sin^2\theta)^{1/2} . \tag{2.17}$$

The angle γ, measured from the equatorial plane, has the value

$$\gamma = \gamma_C - (\gamma_C - \gamma_D) \{1 - [1 - (n/N)]^{c_2}\} , \tag{2.18}$$

where c_2 is the nodal point crowding index for the vessel.

The values of γ_C and γ_D are given by the expressions

$$\begin{aligned} \gamma_C &= \tan^{-1} (z_C/r_C) , \\ \gamma_D &= \tan^{-1} (z_D/r_D) , \end{aligned} \tag{2.19}$$

where r_D and z_D are the radial and axial coordinates, respectively, of the point D on the trace where it intersects the lower boundary of the vessel-pad zone.

In order to compute values for r_D and z_D, a distinction must be made between the longitudinal and the circumferential two-nozzle configurations. Referring to Figs. 2.2 and 2.4 for the longitudinal configuration, the coordinate values will be given by the following. If D lies on the line SU in the first quadrant,

$$\begin{aligned} r_D &= [(R_p \sin \phi)^2 + P_L^2]^{1/2} , \\ z_D &= R_p \cos \phi , \end{aligned} \tag{2.20}$$

where $\phi = \sin^{-1}[P_L \tan \theta/R_p]$ and $0 \leq \theta \leq \theta_L$. P_L is the length of the vessel pad on the outboard side along the line $\theta = 0°$, as shown in Fig. 2.4(*a*). If D lies on the line UW in the first and second quadrants, i.e., $\theta_L \leq \theta \leq \theta_{LL}$, then

$$\begin{aligned} r_D &= R_p \sin \phi_L/\sin \theta , \\ z_D &= R_p \cos \phi_L , \end{aligned} \tag{2.21}$$

where ϕ_L is the circumferential cutoff angle for the vessel pad. If D

lies on the line *WT* in the second quadrant,

$$r_D = [(R_p \sin \phi)^2 + P_{LL}^2]^{1/2} ,$$
$$z_D = R_p \cos \phi , \tag{2.22}$$

where $\phi = \sin^{-1} [(P_{LL}/R_p) \tan (\theta - 90°)]$ and $\theta_{LL} \leq \theta \leq 180°$. P_{LL} is the length of the vessel pad on the inboard side, i.e., half the distance between the two nozzles along the line $\theta = 180°$, as shown in Fig. 2.4 (*a*).

For the circumferential two-nozzle configuration, the vessel-pad region is located in the second and third quadrants, i.e., $90° \leq \theta \leq 270°$, where θ is measured around the axis of the nozzle in the counterclockwise direction as shown in Figs. 2.3 and 2.5. Note that the (r',θ,z') coordinate system for the nozzle is a simple rotation of the z' axis about the vessel centerline (x axis) so that the x and x' ($\theta = 0°$) axes coincide. If the point *D* lies on the line *SU* in the second quadrant as shown in Fig. 2.5(*a*), then for each surface,

$$r'_D = R_p \sin \phi_L / \sin \theta ,$$
$$z'_D = R_p \cos \phi_L , \tag{2.23}$$
$$90° \leq \theta \leq \tan^{-1} (P_L/R_p \sin \theta_L) + 90° ,$$

where ϕ_L is the right-hand cutoff angle and P_L is the length of the pad along the vessel; R_p is the radius of the surface, as before.

If *D* lies on the line *UV*, then

$$r'_D = [(R_p \sin \phi)^2 + P_L^2]^{1/2} ,$$
$$z'_D = R_p \cos \phi , \tag{2.24}$$

where $\phi = \sin^{-1} [(P_L/R_p) \tan (180° - \theta)]$, and $\tan^{-1} P_L/(R_p \sin \phi_L) + 90° \leq \theta \leq 180°$.

If *D* lies on the line *VW*, then

$$r'_D = [(R_p \sin \xi)^2 + P_L^2]^{1/2} ,$$
$$z'_D = R_p \cos \xi , \tag{2.25}$$

where $\xi = \sin^{-1}[(P_L/R_p)\tan(\theta - 180°)]$ and $180° \leq \varepsilon \leq \tan^{-1}[R_p \sin \xi_{LL}/P_L] + 180°$, where ξ_{LL} is the angle between the z and z' axes, or one-half the angle between the centerlines of the two nozzles.

If D lies on the line WT, then

$$r'_D = R_p \sin \xi_{LL}/\cos(270° - \theta) ,$$
$$z'_D = R_p \cos \xi_{LL} , \tag{2.26}$$

where $\tan^{-1}[R_p \sin \xi_{LL}/P_L] + 180° \leq \theta \leq 270°$.

2.3.3 Global coordinate system transformation

After the nodal coordinates are properly generated in either of the cylindrical coordinate systems, a coordinate transformation is performed to express all the nodal locations in the global Cartesian coordinate system. For the longitudinal nozzle configuration, this is done by setting

$$x = r \cos \theta ,$$
$$y = r \sin \theta , \tag{2.27}$$
$$z = z .$$

For the circumferential nozzle configuration, the equations used are

$$x = r' \cos \theta ,$$
$$y = r' \sin \theta \sin(90° - \xi_{LL}) + z' \cos(90° - \xi_{LL}) , \tag{2.28}$$
$$z = z' \sin(90° - \xi_{LL}) - r' \sin \theta \cos(90° - \xi_{LL}) .$$

2.3.4 Nodal locations on the vessel

When the diameter of the vessel is very large relative to the diameter of the nozzle, the elements remote from the nozzle attachment may be considered too coarse to be practical. In such cases, the above procedure is used to develop the mesh in the nozzle, transition, and vessel-pad zones, but a special rectangular mesh pattern is developed for the

remaining cylindrical part of the vessel. The nodes for this region are generated directly in the global Cartesian coordinate system.

Consider the cylindrical vessel region to be divided into *NN* parts in the longitudinal and circumferential directions of the vessel as shown in Fig. 2.8. If $(\bar{x}, \bar{y}, \bar{z})$ denotes the last nodal station on any meridional

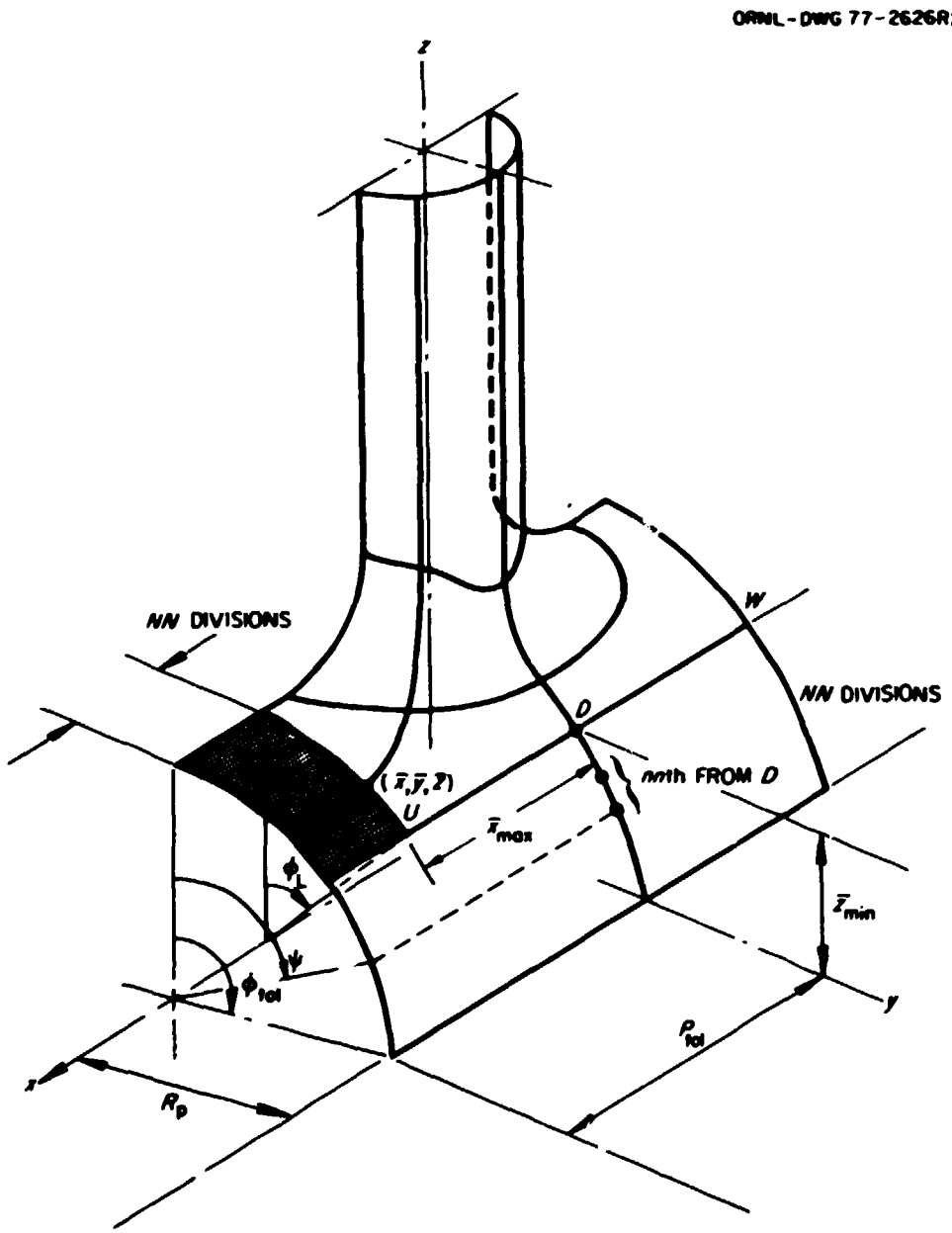

Fig. 2.8. Vessel rectangular mesh zone.

trace from the previous calculation, e.g., at point D, then for the node at the end of the "nnth" division on the cylindrical vessel region, the coordinates are derived as follows. For the longitudinal nozzle configuration, let $\bar{x}_{max}$ be the largest $\bar{x}$ and let $\bar{z}_{min}$ be the smallest $\bar{z}$ for all the meridional traces in the previous computation. Then for the shaded region above $\bar{z}_{min}$ in Fig. 2.8,

$$\begin{aligned} x &= P_{tol} - (P_{tol} - \bar{x}) \left(1 - \frac{nn}{NN}\right)^{c_2} , \\ y &= \bar{y} , \\ z &= \bar{z} , \end{aligned} \tag{2.29}$$

where P_{tol} is the total vessel length and c_2 is the nodal point crowding index for the vessel.

For the region in the unshaded portion below $\bar{z}_{min}$, the coordinates are as follows.

For $x \leq \bar{x}_{max}$:

$$\begin{aligned} x &= \bar{x} , \\ y &= R_p \sin \psi , \\ z &= R_p \cos \psi , \end{aligned} \tag{2.30}$$

where $\psi = \phi_{tol} - (\phi_{tol} - \phi_L)(1 - nn/NN)^{c_2}$ and ϕ_{tol} is the total cutoff angle for the vessel; ϕ_L is the cutoff angle for the vessel pad as before.

For $x > \bar{x}_{max}$:

$$\begin{aligned} x &= P_{tol} - (P_{tol} - \bar{x})(1 - nn/NN)^{c_2} , \\ y &= R_p \sin \psi , \\ z &= R_p \cos \psi , \\ \psi &= \phi_{tol} - (\phi_{tol} - \phi_L)(1 - nn/NN)^{c_2} . \end{aligned} \tag{2.31}$$

Different equations must be used for the circumferential nozzle configuration. For the region above $\bar{z}_{min}$ (point U on Fig. 2.3),

$$x = -P_{tol} + (P_{tol} - |\bar{x}|)\left(1 - \frac{nn}{NN}\right)^{c_2} ,$$

$$y = \bar{y} , \tag{2.32}$$

$$z = \bar{z} .$$

For the region below $\bar{z}_{min}$ and $|x| \leq |\bar{x}|_{max}$,

$$x = \bar{x} ,$$

$$y = R_p \sin \psi , \tag{2.33}$$

$$z = R_p \cos \psi ,$$

where $\psi = \phi_{tol} - (\phi_{tol} - \phi_L)(1 - nn/NN)^{c_2}$.

For the region below $\bar{z}_{min}$ and $|x| > |\bar{x}|_{max}$,

$$x = -P_{tol} + (P_{tol} - |\bar{x}|)(1 - nn/NN)^{c_2} ,$$

$$y = R_p \sin \psi , \tag{2.34}$$

$$z = R_p \cos \psi ,$$

$$\psi = \phi_{tol} - (\phi_{tol} - \phi_L)(1 - nn/NN)^{c_2} .$$

2.4 FEMG Features

Since the stresses in and near the region of the nozzle attachment are highly localized and may vary nonlinearly through the wall thickness, a fine mesh with a greater concentration of elements should be used there, whereas a coarser mesh will be satisfactory in the more remote regions where the stresses vary less rapidly. To accommodate this type of mesh layout, a general three-dimensional isoparametric solid element which may have from 8 to 21 nodes is used. This range of nodes allows for omitting or including selected midside nodes along the boundary between regions of high and lower element density without the need to use wedge elements, as illustrated in Figs. 2.9 and 2.10. The variable-node element has 3 degrees

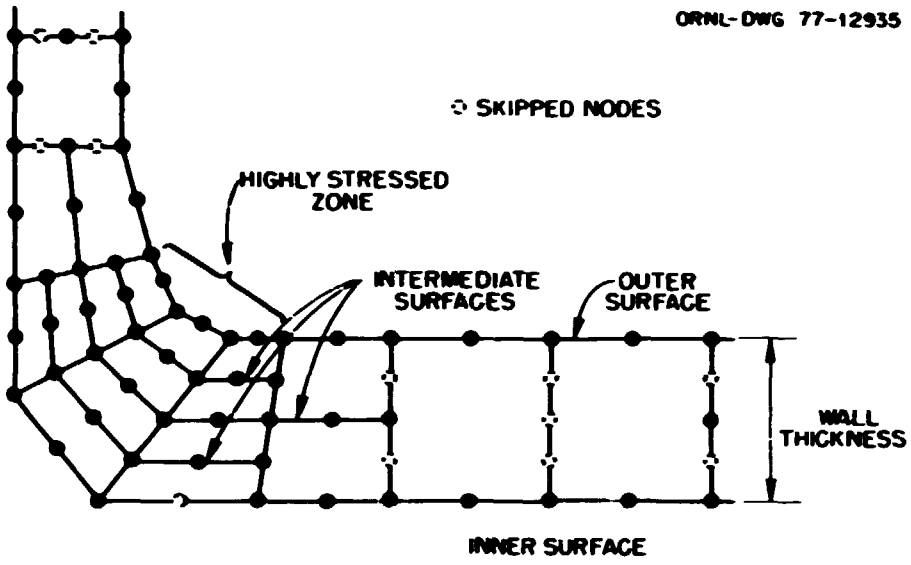

Fig. 2.9. Cross-sectional transition between regions of higher and lower element densities.

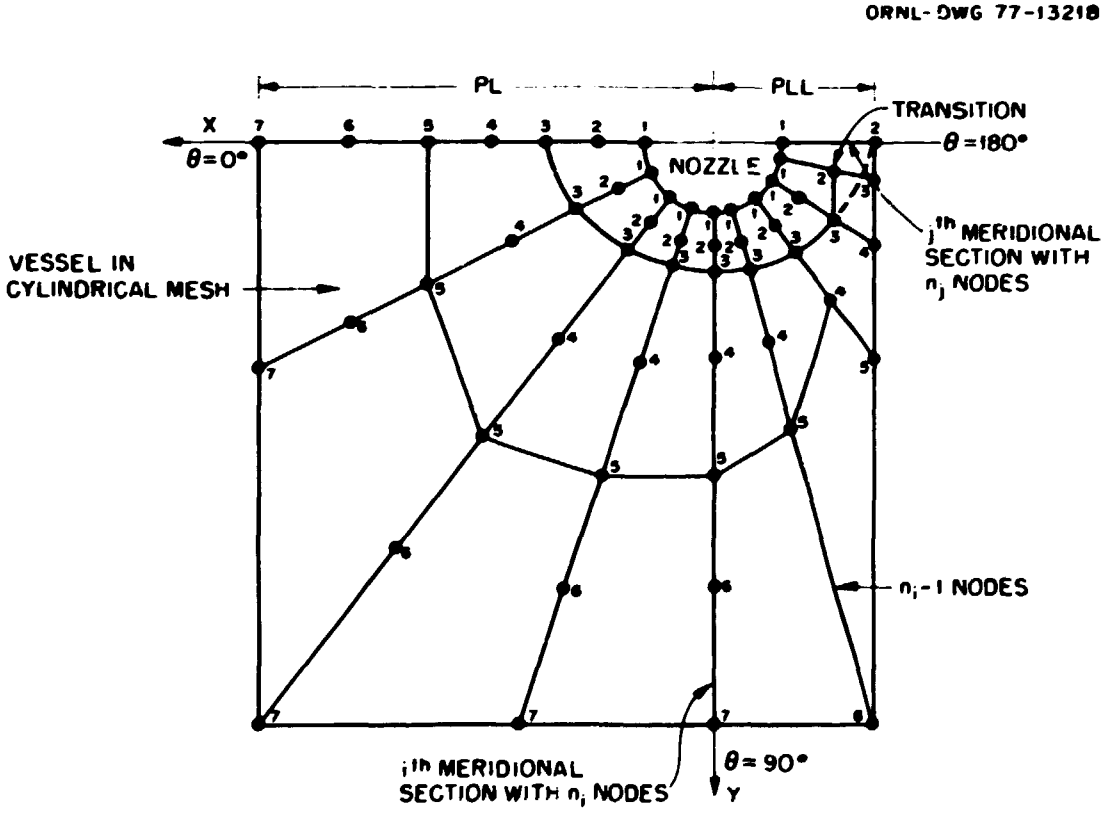

Fig. 2.10. Plan view transition between regions of higher and lower element densities.

of translational freedom per node and thus has from 24 to 63 degrees of freedom per element.

A previous investigation by Clough[17] showed that the isoparametric hexahedral family of elements is distinctly superior to tetrahedral elements for solving three-dimensional problems. The disadvantages are that (1) the element is inherently more complex, (2) the midside nodes both increase the bandwidth of the stiffness matrix and tax the storage capacity and speed of even the largest computers, and (3) automatic mesh generation is more difficult because of the possible variations in nodal connectivities for each element.

To develop a finite-element mesh for analyzing pressure-vessel nozzle models, FEMG first determines coordinate locations for a preliminary "fine-mesh" layout for the entire model. The node coordinate data calculated at this stage are stored in three-dimensional arrays where the dimensional subscripts correspond to surface number, meridional section, and trace division. In this preliminary fine mesh, the number of nodes must be the same for each surface (inside, intermediate, and outside), except for those surfaces originating in the nozzle taper which will have fewer nodes. The number of trace divisions, and consequently the number of nodes along a trace, however, may differ with the angular division θ as illustrated in Fig. 2.10. In this illustration each of the nodes 1, 2, ..., 7 along the trace at $\theta = 0$ will be located first, followed by those numbered 1, 2, ..., 7 on the next trace until all the points on the surface have been located. FEMG will then locate node points for the next surface, etc. When all the nodes in the preliminary fine mesh have been located, their coordinates may be printed if desired before the elements are generated.

At present, FEMG contains five element-indicator options. The first uses all the nodes to develop a mesh consisting entirely of 8-node elements. The second uses all the nodes but develops a mesh which may consist of elements with 8 to 16 nodes. For this type of mesh, illustrated in Fig. 2.10, element midside nodes are not assigned in the θ direction to form the 16-node elements. To form elements with less than 16 nodes, some or all of the midside nodes along the trace lines are not assigned.

A third option will produce a mesh consisting of elements with 20 or fewer nodes using all the nodal locations determined in the preliminary fine mesh operation.

The fourth and fifth element indicator options do not use all the nodal locations determined in the first pass, but selectively skip nodes in the thickness direction to form a mesh like the one illustrated in Fig. 2.9. The fourth option will give a mesh consisting of 8- to 16-node elements, whereas the fifth option will also include 20-node elements.

Whenever a node point is skipped, it is eliminated from the fine-mesh array described above. After the skipping process has been completed, nodes are numbered sequentially starting at the top of the nozzle's inside surface at the minimum value of θ. The numbering is then arranged in the order of (1) increasing angle θ, from 0 to 180° for the longitudinal nozzle configuration or from 90 to 270° for the circumferential nozzle configuration; (2) for each surface, from the inner surface to the outer surface; and (3) along each trace beginning at the top of the nozzle (or at the top of the respective surface when it originates in the nozzle taper). This numbering scheme minimizes the bandwidth of the stiffness matrix and thus reduces the cost of the computations. Element numbers are assigned in the same manner as the node numbers, beginning at $\theta = 0$ on the inside layer at the top of the nozzle and proceeding around, outward, and down the model.

If automated element connectivity generation is desired, several additional restrictions must be satisfied. First, 20 node elements may not be used because of the difficulty in developing an algorithm to account for all possible variations in the connectivities. This eliminates using the third and fifth element-indicator options discussed above for automatic connectivity generation, although for those cases the connectivities may be input manually.

Second, for an unreinforced nozzle the total number of divisions along each trace in a given meridional section must be equal. For a reinforced nozzle the portion of each trace above and below the taper must have the same number of divisions as every other trace on that section.

Third, if the number of trace divisions are not the same for every angular division θ, then the number of nodes may not differ by more than 1

for adjacent meridional sections. This is illustrated in Fig. 2.10, for example, where the meridional section at $\theta = 90°$ has 7 nodes, the one at $\theta = 108°$ has 6 nodes, etc., until the one at $\theta = 180°$ has 2 nodes. In general, if the meridional trace i has n_i nodes and the meridional trace j has n_j nodes, then the following relation must be satisfied:

$$n_j = n_i \pm (j - i) \ , \tag{2.35}$$

where the positive sign is used for an increasing number of nodes, and the negative sign is used for a decreasing number. This restriction implies that the number of elements along adjacent strips will either be the same or will differ by one. The number of surface nodes per element will depend on the element-indicator option used.

3. THREE-DIMENSIONAL FINITE-ELEMENT ANALYSIS

The MULT-NOZZLE program module SAP3M is a modified and improved version of the SAP3 finite-element program originally developed by Wilson[7] at the University of California. The major modifications to SAP3 include (1) replacement of the original library of elements with the variable 8- to 21-node solid isoparametric hexahedral element,[10] (2) incorporation of an improved matrix-equation solving routine[12] to increase the program efficiency, and (3) the addition of a local-smoothing extrapolation algorithm[8] to improve the stress calculation accuracy at the element surface points and to reduce the program sensitivity to Poisson's ratio. Each of these items is discussed more fully below.

3.1 Isoparametric Finite-Element Mapping

Formulation of the equations for an isoparametric finite element is greatly simplified by describing the behavior of the element in a local (or natural) coordinate system in which the element is a perfect cube, as shown in Fig. 3.1(*b*). For a 21-node element, the mapping of the element coordinates from this natural coordinate system to the global Cartesian coordinate system [see Fig. 3.1(*a*)] of the original structure is accomplished with the following relations:

$$x = \sum_{m=1}^{21} N_m(r,s,t)\, x_m ,$$

$$y = \sum_{m=1}^{21} N_m(r,s,t)\, y_m , \qquad (3.1)$$

$$z = \sum_{m=1}^{21} N_m(r,s,t)\, z_m ,$$

where (x, y, z) are the global system coordinates, (x_m, y_m, z_m) for $m = 1, 2, \ldots, 21$ are the global coordinates of the node points m, and $N_m(r,s,t)$ for $m = 1, 2, \ldots, 21$ are the mapping functions (also called

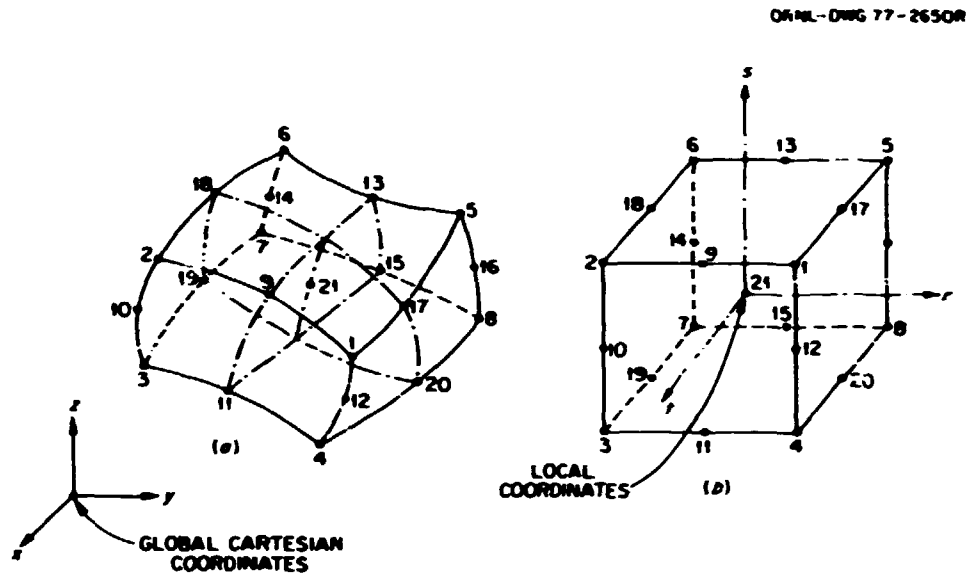

Fig. 3.1. Coordinate systems for (a) parent and (b) mapped elements.

shape functions) expressed in the local (r,s,t) coordinate system. Using the node numbering sequence indicated in Fig. 3.1, the shape functions are as follows:

$$
\begin{aligned}
N_1 &= h_1 - \tfrac{1}{2}(h_9 + h_{17} + h_{12}) - \tfrac{1}{8}h_{21} \ , \\
N_2 &= h_2 - \tfrac{1}{2}(h_{10} + h_{18} + h_9) - \tfrac{1}{8}h_{21} \ , \\
N_3 &= h_3 - \tfrac{1}{2}(h_{11} + h_{19} + h_{10}) - \tfrac{1}{8}h_{21} \ , \\
N_4 &= h_4 - \tfrac{1}{2}(h_{12} + h_{20} + h_{11}) - \tfrac{1}{8}h_{21} \ , \\
N_5 &= h_5 - \tfrac{1}{2}(h_{13} + h_{17} + h_{16}) - \tfrac{1}{8}h_{21} \ , \\
N_6 &= h_6 - \tfrac{1}{2}(h_{14} + h_{18} + h_{13}) - \tfrac{1}{8}h_{21} \ , \\
N_7 &= h_7 - \tfrac{1}{2}(h_{15} + h_{19} + h_{14}) - \tfrac{1}{8}h_{21} \ , \\
N_8 &= h_8 - \tfrac{1}{2}(h_{16} + h_{20} + h_{15}) - \tfrac{1}{8}h_{21} \ , \\
N_m &= h_m - \tfrac{1}{4}h_{21} \text{ for } m = 9,\ 10,\ \ldots,\ 20 \ , \\
N_{21} &= h_{21} \ ,
\end{aligned}
\qquad (3.2)
$$

where

$$h_m = H(r,r_m)H(s,s_m)H(t,t_m) \; ; \qquad m = 1, 2, \ldots, 21 \; , \tag{3.3}$$

and (r_m, s_m, t_m) are the local coordinates for the node points. If a particular node point m is skipped (see Section 2.4), $h_m \equiv 0$. The functions $H(r,r_m)$, $H(s,s_m)$, and $H(t,t_m)$ in Eq. (3.3) are defined by the general expression

$$H(\beta,\beta_i) = \begin{cases} \frac{1}{2}(1 + \beta\beta_i), & \text{for } \beta_i = \pm 1 \\ 1 - \beta^2 \; , & \text{for } \beta_i = 0 \end{cases} \; , \tag{3.4}$$

where

$$\beta = r,s,t \; ; \qquad \beta_i = r_m,s_m,t_m \; . \tag{3.5}$$

3.2 Displacement Function

The assumed displacement distribution for the 21 node isoparametric hexahedral finite element is

$$\begin{Bmatrix} u \\ v \\ w \end{Bmatrix} = \begin{bmatrix} N_m & 0 & 0 \\ 0 & N_m & 0 \\ 0 & 0 & N_m \end{bmatrix} \{U\} \; , \tag{3.6}$$

where the shape functions N_m $(m = 1, 2, \ldots, 21)$ are row vectors given by Eqs. (3.2) to (3.5). The nodal displacement vector $\{U\}$ is defined by

$$\{U\}^T = [u_1, u_2, \ldots, u_{21}, v_1, v_2, \ldots, v_{21}, w_1, w_2, \ldots, w_{21}] \; , \tag{3.7}$$

where the u's, v's, and w's are the global coordinate system displacements of the 21 node points.

3.3 Stress-Strain Relations

The constitutive equations used in SAP3M are the usual orthotropic linear elastic relations given by the general expression

$$\{\sigma\} = [C]\ \{\varepsilon\} \ , \tag{3.8}$$

where the stress and strain vectors $\{\sigma\}$ and $\{\varepsilon\}$ are defined in rectangular Cartesian coordinates by

$$\{\sigma\}^T = [\sigma_{xx},\ \sigma_{yy},\ \sigma_{zz},\ \tau_{yz},\ \tau_{xz},\ \tau_{xy}] \tag{3.9}$$

and

$$\{\varepsilon\}^T = [\varepsilon_{xx},\ \varepsilon_{yy},\ \varepsilon_{zz},\ \gamma_{yz},\ \gamma_{xz},\ \gamma_{xy}] \ . \tag{3.10}$$

The coefficient matrix $[C]$ contains the elastic moduli and Poisson's ratios. Sufficient generality is permitted to accommodate any material with simple symmetry; thus

$$[C] = \begin{bmatrix} C_{11} & C_{12} & C_{13} & 0 & 0 & 0 \\ & C_{22} & C_{23} & 0 & 0 & 0 \\ & & C_{33} & 0 & 0 & 0 \\ & & & C_{44} & 0 & 0 \\ \text{symmetric} & & & & C_{55} & 0 \\ & & & & & C_{66} \end{bmatrix} \ . \tag{3.11}$$

In terms of the elastic moduli E_i, Poisson's ratios ν_{ij}, and shear moduli G_{ij} for orthotropic materials behavior, the C_{ij} coefficients take the forms

$$\begin{aligned} C_{11} &= (1 - \nu_{23}\ \nu_{32})\ E_1/V \ , \\ C_{22} &= (1 - \nu_{31}\ \nu_{12})\ E_2/V \ , \\ C_{33} &= (1 - \nu_{12}\ \nu_{21})\ E_3/V \ , \\ C_{12} &= (\nu_{21} + \nu_{23}\ \nu_{31})\ E_1/V \ , \\ C_{23} &= (\nu_{32} + \nu_{12}\ \nu_{32})\ E_2/V \ , \\ C_{13} &= (\nu_{13} + \nu_{23}\ \nu_{12})\ E_3/V \ , \\ C_{44} &= G_{23} \ , \\ C_{55} &= G_{13} \ , \\ C_{66} &= G_{12} \ , \end{aligned} \tag{3.12}$$

where

$$V = 1 - \nu_{12}\nu_{21} - \nu_{23}\nu_{32} - \nu_{31}\nu_{13} - 2\nu_{12}\nu_{23}\nu_{31} \ . \tag{3.13}$$

The following reciprocity relationships hold because of symmetry:

$$\frac{E_1}{E_2} = \frac{\nu_{12}}{\nu_{21}} \ ,$$

$$\frac{E_2}{E_3} = \frac{\nu_{23}}{\nu_{32}} \ , \tag{3.14}$$

$$\frac{E_3}{E_1} = \frac{\nu_{31}}{\nu_{13}} \ .$$

For isotropic materials behavior,

$$E_i = E \ ,$$

$$\nu_{ij} = \nu \ , \tag{3.15}$$

$$G_{ij} = G = E/2(1 + \nu) \ ,$$

with

$$C_{ii} = E(1 - \nu)/(1 - 2\nu)(1 + \nu) \qquad (ii = 11, 22, 33) \ ,$$

$$C_{ij} = E\nu/(1 - 2\nu)(1 + \nu) \qquad (i,j = 1, 2, 3), \tag{3.16}$$

$$C_{ii} = G = E/2(1 + \nu) \qquad (ii = 44, 55, 66) \ .$$

3.4 Strain-Displacement and Stress-Displacement Relations

The general expression governing the geometry of deformation has the form

$$\{\varepsilon\} = [L]\ \{u\} + \{\varepsilon_0\} \ , \tag{3.17}$$

where $\{u\}$ is the displacement vector $\{u, v, w\}$ and $[L]$ is a linear differential operator. The term $\{\varepsilon_0\}$ in Eq. (3.17) represents any type of initial strain. Usually this term accounts for thermal expansions. The

operator $[L]$ has the form

$$[L] = \begin{bmatrix} \frac{\partial}{\partial x} & 0 & 0 \\ 0 & \frac{\partial}{\partial y} & 0 \\ 0 & 0 & \frac{\partial}{\partial z} \\ 0 & \frac{\partial}{\partial z} & \frac{\partial}{\partial y} \\ \frac{\partial}{\partial z} & 0 & \frac{\partial}{\partial x} \\ \frac{\partial}{\partial y} & \frac{\partial}{\partial x} & 0 \end{bmatrix} . \tag{3.18}$$

Substituting Eq. (3.6) into Eq. (3.17) gives

$$\{\varepsilon\} = [L] \begin{bmatrix} N_m & 0 & 0 \\ 0 & N_m & 0 \\ 0 & 0 & N_m \end{bmatrix} \{U\} + \{\varepsilon_0\} , \tag{3.19}$$

or

$$\{\varepsilon\} = [B]\{U\} + \{\varepsilon_0\} , \tag{3.20}$$

where

$$[B] = [L] \begin{bmatrix} N_m & 0 & 0 \\ 0 & N_m & 0 \\ 0 & 0 & N_m \end{bmatrix} , \tag{3.21}$$

or

$$[B] = \begin{bmatrix} \frac{\partial N_m}{\partial x} & 0 & 0 \\ 0 & \frac{\partial N_m}{\partial y} & 0 \\ 0 & 0 & \frac{\partial N_m}{\partial z} \\ 0 & \frac{\partial N_m}{\partial z} & \frac{\partial N_m}{\partial y} \\ \frac{\partial N_m}{\partial z} & 0 & \frac{\partial N_m}{\partial x} \\ \frac{\partial N_m}{\partial y} & \frac{\partial N_m}{\partial x} & 0 \end{bmatrix} . \tag{3.22}$$

The derivatives in the matrix $[B]$ are evaluated as follows:

$$\begin{Bmatrix} \frac{\partial N_m}{\partial r} \\ \frac{\partial N_m}{\partial s} \\ \frac{\partial N_m}{\partial t} \end{Bmatrix} = \begin{bmatrix} \frac{\partial x}{\partial r} & \frac{\partial y}{\partial r} & \frac{\partial z}{\partial r} \\ \frac{\partial x}{\partial s} & \frac{\partial y}{\partial s} & \frac{\partial z}{\partial s} \\ \frac{\partial x}{\partial t} & \frac{\partial y}{\partial t} & \frac{\partial z}{\partial t} \end{bmatrix} \begin{Bmatrix} \frac{\partial N_m}{\partial x} \\ \frac{\partial N_m}{\partial y} \\ \frac{\partial N_m}{\partial t} \end{Bmatrix} = [J] \begin{Bmatrix} \frac{\partial N_m}{\partial x} \\ \frac{\partial N_m}{\partial y} \\ \frac{\partial N_m}{\partial z} \end{Bmatrix} , \tag{3.23}$$

where $[J]$ is the Jacobian. The inverse relation gives the appropriate chain-rule differentiation needed in Eq. (3.22):

$$\begin{Bmatrix} \frac{\partial N_m}{\partial x} \\ \frac{\partial N_m}{\partial y} \\ \frac{\partial N_m}{\partial z} \end{Bmatrix} = [J]^{-1} \begin{Bmatrix} \frac{\partial N_m}{\partial r} \\ \frac{\partial N_m}{\partial s} \\ \frac{\partial N_m}{\partial t} \end{Bmatrix} . \tag{3.24}$$

The stress-displacement relation is obtained by substituting Eq. (3.20) into Eq. (3.8):

$$[\sigma] = [C][B]\{U\} + [C]\{\epsilon_0\} \ . \tag{3.25}$$

3.5 Element Stiffness

The element stiffness, which defines the relation between nodal displacements and corresponding nodal forces for a given finite element, is obtained by applying the work-energy principle,

$$\{R\} = \int_{\text{vol}} [B]^T [C][B] \, dv \, \{U\} + \int_{\text{vol}} [B]^T [C]\{\epsilon_0\} \, dv \ , \tag{3.26}$$

where $\int [B]^T [C]\{\epsilon_0\} \, dv$ is the initial nodal load-vector and $\{R\}$ is a nodal force vector. The element stiffness matrix is defined by

$$[k] = \int_{\text{vol}} [B]^T [C][B] \, dv \ . \tag{3.27}$$

Since the strain matrix is expressed in natural coordinates, a change in variables is needed; thus

$$dv = dx \, dy \, dz = |J| \, dr \, ds \, dt \ , \tag{3.28}$$

where $|J|$ is the determinant of the Jacobian defined in Eq. (3.23). The element stiffness matrix then takes the form

$$[k] = \int_{-1}^{1} \int_{-1}^{1} \int_{-1}^{1} [B]^T [C][B] |J| \, dr \, ds \, dt \ . \tag{3.29}$$

For hexahedral finite elements, the integrals in Eq. (3.29) are too complex to evaluate in closed form, and Gaussian quadrative numerical integration is normally used. Equation (3.29) may be expressed approximately in numerical form as

$$[k] = \sum_{i=1}^{n_i} \sum_{j=1}^{n_j} \sum_{k=1}^{n_k} s_i s_j s_k \, \{[B]^T [C][B]\}_{ijk} \, |J|_{ijk} \ , \tag{3.30}$$

where n_i, n_j, n_k are the integration orders and s_i, s_j, s_k are independent weighting coefficients in r,s,t at the Gaussian integration points.

3.6 Equilibrium Equations

By summing the element stiffnesses from Eq. (3.30) for each node point in the finite-element model and accounting for the interface compatibility between elements (i.e., connectivities), one obtains a set of algebraic equilibrium equations in terms of unknown nodal point displacements for the entire computational model. Thus

$$\{F\} = [K]\{\bar{U}\} , \tag{3.31}$$

where $\{F\}$ is the total nodal force vector, $[K]$ is the structural stiffness matrix, and $\{\bar{U}\}$ is the complete set of nodal displacements.

For three-dimensional finite-element structural analyses, Eq. (3.31) consists of several thousand linear simultaneous equations which must be solved for the unknown displacements $\{\bar{U}\}$. Normally the major fraction of computer time required for the analysis is consumed in the solution to these equations. Any improvement in the numerical algorithms required to solve these equations will thus significantly reduce the total cost of the analysis. Recently, an improved matrix equation solution algorithm, which is particularly well suited to the SAP series of finite-element programs, was developed by Mandkar and Powell[12] at the University of California. Their algorithm is based on a modified Crout reduction scheme[11] and compacted column vector storage, and eliminates almost all unnecessary arithmetic operations. The matrix equation solution routine currently in SAP3M was written and installed under Professor Powell's direction.

3.7 Stress-Smoothing Technique

Since stresses are proportional to the derivatives of displacements, the calculated stress values will be less accurate than the displacements determined from the solution of Eq. (3.31). Recently, several investigators[8,18-23] have attempted to improve the stress calculation accuracy for isoparametric finite-element models by calculating stresses at optimal locations in the elements and then extrapolating to obtain stresses at the desired node positions. Generally, the optimal locations are the Gaussian integration points[24] on the interior of the element. Eight such points, identified as S_1, S_2, ..., S_8, are shown in Fig. 3.2 for second-order

ORNL-DWG 77-2627

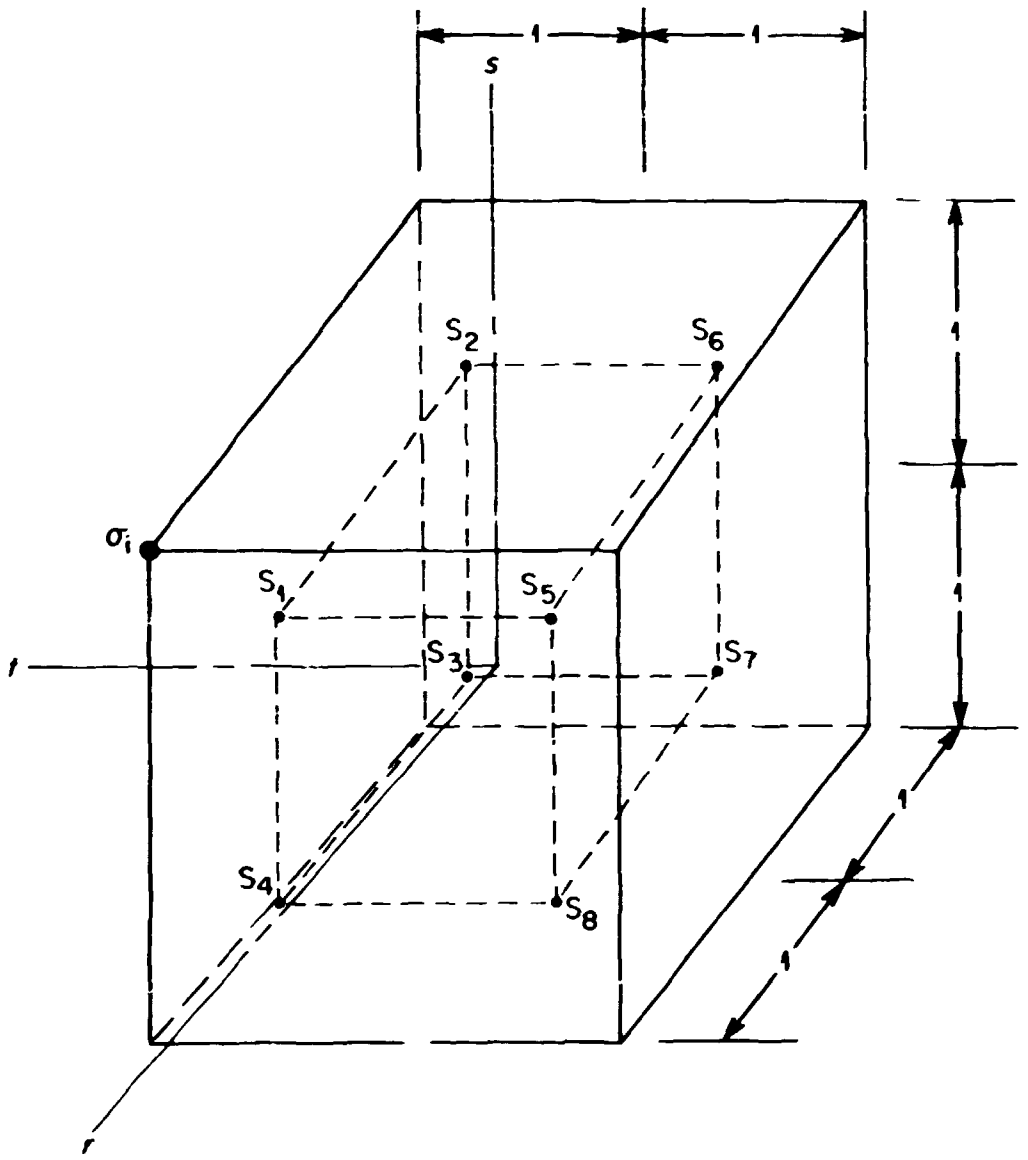

Fig. 3.2. Stresses at 2×2×2 Gauss integration points.

(2×2×2) Gaussian integration. In 1974, Hinton and Campbell[8] proposed a local smoothing technique using a bilinear cubic relation to extrapolate the 2×2×2 Guassian point stresses to the element surfaces (or to any arbitrary point within the element). An algorithm based on their technique was developed and installed in SAP3M. The following bilinear cubic

equation is used for extrapolation:

$$\begin{aligned}\sigma_i(r_p,s_p,t_p) = \frac{1}{8}\Big[& (1 + r_p')(1 + s_p')(1 + t_p')\, S_{1i} \\ & + (1 - r_p')(1 + s_p')(1 + t_p')\, S_{2i} \\ & + (1 - r_p')(1 - s_p')(1 + t_p')\, S_{3i} \\ & + (1 + r_p')(1 - s_p')(1 + t_p')\, S_{4i} \\ & + (1 + r_p')(1 + s_p')(1 - t_p')\, S_{5i} \\ & + (1 - r_p')(1 + s_p')(1 - t_p')\, S_{6i} \\ & + (1 - r_p')(1 - s_p')(1 - t_p')\, S_{7i} \\ & + (1 + r_p')(1 - s_p')(1 - t_p')\, S_{8i}\Big] \ ,\end{aligned} \tag{3.32}$$

where $\sigma_i(r_p, s_p, t_p)$ is a given stress component ($i = 1, 2, \ldots, 6$) at the desired arbitrary point (r_p, s_p, t_p) and $S_{1i}, S_{2i}, \ldots, S_{8i}$ are the corresponding stress components at the 2×2×2 Gaussian integration points. The parameters r_p', s_p', t_p' are defined by

$$(r_p', s_p', t_p') = \sqrt{3}\ (r_p, s_p, t_p) \ . \tag{3.33}$$

4. SAP3M VALIDATION

As stated earlier, the MULT-NOZZLE computer program consists of two major modules that may be operated more or less independently. FEMG automatically prepares the finite-element mesh, including nodal point coordinates, finite-element connectivities, mesh options, and boundary value specifications (subject to the restrictions discussed in Chapter 2) for input to the finite-element solution module SAP3M. SAP3M computes the nodal point displacements and stress tensor components at specified data points for the entire finite-element model and prints and/or stores the results for later postprocessing.

Two types of loading conditions, element-load and structural-load cases, can be specified for SAP3M. Acceptable element-load cases include thermal expansion, gravity, and surface pressure, where the pressure may be constant, hydrostatic, or arbitrarily distributed depending on the input parameter specified. Structural-load cases include applied nodal forces. Element-load case multipliers are used to provide linear combinations of element-load types; and structural-load case multipliers provide a way of combining element-load with structural-load cases.

SAP3M outputs tabulations of both the input and solution data. The input data tables include all the information necessary to define the problem. Specifically, these are the geometric and modeling data such as node coordinates, element connectivities, constraints, material properties, and load information. Information affecting the solution procedure such as integration orders and stress recovery points is also included in the printout. The solution data consists of equilibrium equation numbers, nodal displacements, and stress tables. The stress tables show the six stress components in global coordinates and the three principal stresses at up to eight different points for each element. The output data may also be written onto a permanent storage device for future postprocessing.

The programs will be available in CDC 6400/6600/7600 and IBM 360/370 versions through the Argonne Code Center. The IBM version uses double-precision arithmetic and provides for plotting the finite-element meshes. Because of the computer time involved in a normal run, it is strongly

suggested that the finite-element mesh developed by FEMG be plotted and thoroughly examined before executing the SAP3M analysis.

To demonstrate the basic accuracy of the SAP3M module, two classical problems for which theoretical solutions exist were solved: a simply supported beam with a uniformly distributed load[19] and a thick-walled ring under internal pressure (Lamé's problem[14]). Stresses were computed using different values for Poisson's ratio ν and both a 2×2×2 and a 3×3×3 Gaussian integration scheme to investigate their influence on the accuracy of the numerical algorithm. Theoretically, Poisson's ratio should not affect the stresses for these two problems but may be important for the nozzle problem. As discussed more fully below, the numerical results for both classical problems gave excellent agreement with the theoretical solutions. Variations in Poisson's ratio from $\nu = 0$ to $\nu = 0.485$ had a negligible influence on the calculated stresses (less than 1/2%). The different integration schemes gave results which differed by about 1%.

4.1 Studies of the Simply Supported Beam

The simply supported beam model used in the analysis is shown in Fig. 4.1. Because of symmetry, a finite-element model was constructed for only half the beam, using five 12-node solid elements and 44 nodal points. All the nodal displacements were restrained in the z direction (plane strain), and roller support boundary conditions for the simple supports and symmetric constraints were specified. Two values of Poisson's ratio, $\nu = 0.0$ and $\nu = 0.485$, for photoelastic epoxy were considered.

The following material properties were considered (ρ is the material density):

Material I	Material II
$\nu = 0.0$	$\nu = 0.485$
$E = 12 \times 10^6$ psi	$E = 12 \times 10^6$ psi
$G = 6 \times 10^6$ psi	$G = 4.04 \times 10^6$ psi
$\alpha = 10^{-6}\ {}^\circ F^{-1}$	$\alpha = 10^{-6}\ {}^\circ F^{-1}$
$\rho = 0$ or 24,000 lb/in.^{3}	$\rho = 0$ or 24,000 lb/in.^{3}

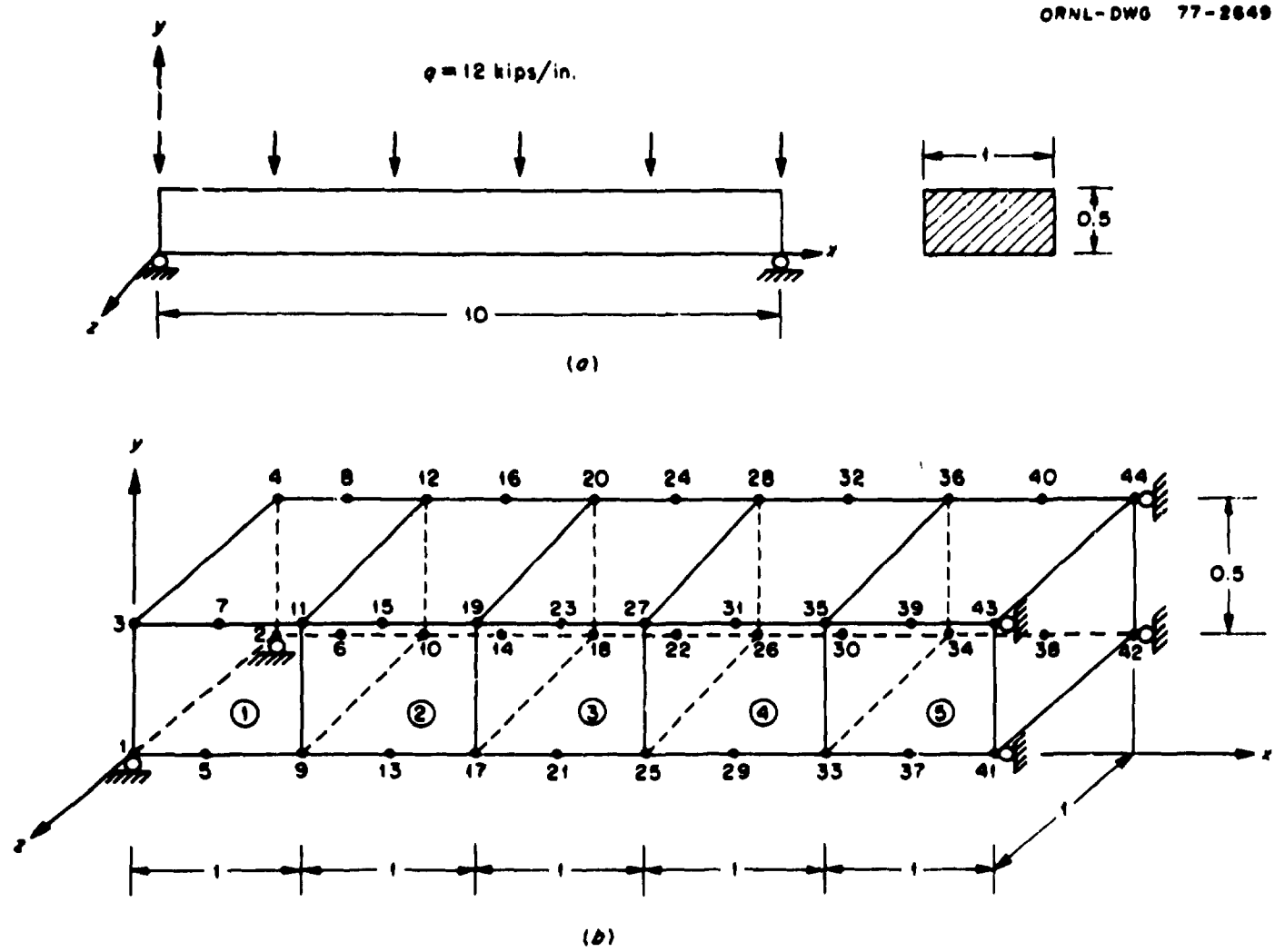

Fig. 4.1. Beam model: (*a*) simply supported beam in plane strain bending; (*b*) finite-element model. Dimensions are in inches.

The beam was analyzed for a uniformly distributed load of 12,000 lb/in. and for a uniform temperature increase of 100°F. For the uniformly distributed load, three load cases which should give identical results were calculated: load case 1, for which the load was idealized as a set of uniform nodal forces on the top surface of the beam; load case 2, where the loading was a gravity (body) force in the negative y direction equal to the weight of the beam (24,000 lb/in.^{3}); and load case 3, where the load was specified as a constant pressure equal to 12,000 psi on the top surface. Load case 4 was for the thermal loading. Load case 1 was set up as a structural-load case with nodal forces; load cases 2, 3, and 4 were assigned as element-load cases A, B, and C, respectively. For Material I with $\nu = 0.0$, only the 2×2×2 Gauss integration rule was used in evaluating the stiffness matrix, but for Material II ($\nu = 0.485$), both the 2×2×2 and 3×3×3 Gauss rules were used.

In all, nine separate cases for the uniformly distributed load and two cases for uniform temperature expansion were analyzed. The maximum stresses for each case and the corresponding theoretical values are given in Table 4.1. All the computed results are in excellent agreement with

Table 4.1. Stresses for the beam model

Method	Load case[a]	ν	Gauss rule	Maximum σ_x stresses (ksi)				
				Distance (in.) from left support				
				1	2	3	4	5
Theoretical	1-3	0, 0.485		1296.0	2304.0	3024.0	3456.0	3600.0
Finite element	1	0, 0.485	2×2×2	1296.0	2304.0	3024.0	3456.0	3600.0
	1	0.485	3×3×3	1281.3	2292.5	3015.8	3451.1	3598.4
	2	0, 0.485	2×2×2	1320.0	2328.0	3048.0	3480.0	3624.0
	2	0.485	3×3×3	1305.3	2316.5	3039.8	3475.1	3622.4
	3	0, 0.485	2×2×2	1320.0	2328.0	3048.0	3480.0	3624.0
	3	0.485	3×3×3	1305.3	2316.5	3039.8	3475.1	3622.4
				σ_z stresses (ksi)				
Theoretical or finite element	4	0, 0.485	2×2×2	-1.2				
		0, 0.485	3×3×3	-1.2				

[a]Load case 1 was set up with uniform nodal forces on the top surface of the beam, 120,000 lb total; load case 2 was set up using a gravity force equal to the weight of the beam, 24,000 lb/in.^{3}; load case 3 was set up with a constant pressure equal to 12,000 psi on the top surface; and load case 4 was a uniform temperature increase of 100°F.

the theoretical predictions, with a maximum error of about 1.9% for load cases 2 and 3 using the 2×2×2 integration rule. In general, the 3×3×3 reduced integration rule seemed to give slightly more accurate results, although the most accurate results (zero error) were calculated for load case 1 using the 2×2×2 integration. The effect of Poisson's ratio was not detectable for this problem.

4.2 Studies of the Lamé Thick-Walled Ring

A ring structure with $\nu = 0.3$ and $\nu = 0.485$ loaded with a unit internal pressure was also analyzed, and the relative effects of the "reduced integration" (2×2×2 Gauss order) and the "exact integration" (3×3×3 Gauss order) techniques were investigated. This model was also used to investigate the effects of distorted elements. Since the ring has two planes of symmetry and is loaded axisymmetrically, only one quarter of the structure was modeled. The finite-element model consists of six 16-node isoparametric solid elements with a total of 66 nodal points, as shown in Fig. 4.2. Symmetric boundary conditions were assumed for the vertical and horizontal planes.

Material properties for the computational model were as follows:

Material I	Material II
$\nu = 0.3$	$\nu = 0.485$
$E = 7500$ psi	$E = 7500$ psi
$G = 2885$ psi	$G = 2525$ psi

For this model, stresses were computed for both values of Poisson's ratio using both integration rules. Stresses were also computed for two cases in which elements 3 and 4 were distorted using $\nu = 0.3$ in one case and $\nu = 0.485$ in the other. Both cases were run using the 2×2×2 integration rule.

The internal pressure was set up as load case A. The resulting circumferential stresses at the inner and outer surfaces are given in Table 4.2. For this model, the 2×2×2 integration rule gave the more accurate results and gave exactly the same values for the two Poisson's ratios.

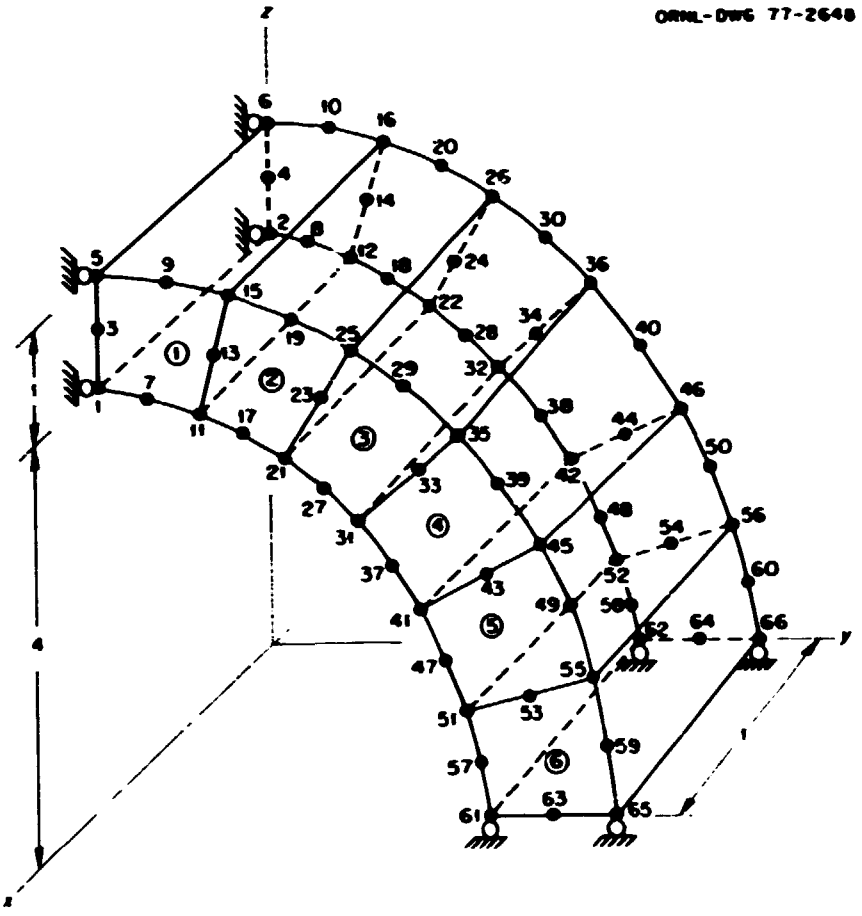

Fig. 4.2. Finite-element model for ring (Lamé's problem). Dimensions are in inches.

Table 4.2. Circumferential stresses for the ring model

Surface	Theoretical[a]	Finite element 2×2×2		Finite element 3×3×3		Distorted element 2×2×2	
		$\nu = 0.3$	$\nu = 0.485$	$\nu = 0.3$	$\nu = 0.485$	$\nu = 0.3$	$\nu = 0.485$
Inner	4.556	4.555	4.555	4.593	4.523	4.552	4.493
Outer	3.556	3.544	3.544	3.586	3.574	3.507	3.563

[a]From the solution to Lamé's problem (Ref. 14),

$$\sigma_0 = \frac{pr_1^2}{r_2^2 - r_1^2}\left(1 + \frac{r_2^2}{r^2}\right) .$$

In the present case, $r_2 = 5$ in.; $r_1 = 4$ in.; and $p = 1$ psi.

The 3×3×3 rule gave values which differed by about 1.5% (at the inner surface) for the two materials. The maximum error for the distorted element cases was about 1.4%.

4.3 Discussion of Classical Problem Results

The finite-element results for both verification problems considered in this chapter — the simply supported beam loaded with a uniformly distributed load and the thick-walled ring under internal pressure — gave excellent agreement with theoretical solutions. Different values for Poisson's ratio, from $\nu = 0$ to $\nu = 0.485$ (nearly incompressible material), apparently had very little influence on the calculated stresses. Theoretically, the stresses for these problems do not depend on ν. The Gaussian integration rule that was used to evaluate the stiffness matrix had some influence on the calculated stresses, but neither the 2×2×2 nor the 3×3×3 approximation could be claimed to be more accurate. Although the 3×3×3 rule tended to give higher stresses and was more accurate for the beam problem, the 2×2×2 rule gave more accurate results for the ring problem. The effect of distorting two of the elements apparently had less influence on the accuracy than the choice of integration rules. For all three problems, however, the maximum errors were less than 2%.

Basically, the analyses discussed here tend to confirm the accuracy of the finite-element method as expressed in the SAP3M module. Several variables, however, which may be important in the analysis of closely spaced nozzles in pressure vessels were not investigated with the beam or ring. Two of these are the number of elements and variable-element density using the variable-node element. Rather than investigate the effects of these variables with classical problems, more meaningful results (for the problem at hand) can be obtained by analyzing real structures and comparing the results with experimental data. Problems of this type are considered in Chapters 5 to 7.

5. ANALYSIS OF PRESSURE VESSEL MODEL WC-12DD

This chapter describes the finite-element analysis of a thick-walled cylindrical pressure vessel with two closely spaced thick-walled nozzles located in a longitudinal plane, identifed as Westinghouse photoelastic model WC-12DD and analyzed experimentally by Leven.[15] A sketch of the model, showing important geometric details, is shown in Fig. 5.1.

5.1 Finite-Element Model

There are two planes of symmetry in WC-12DD — the longitudinal x-z plane that passes through the centerlines of both nozzles and a transverse plane midway between the nozzles and normal to the centerline of the vessel parallel to the y-z plane (Fig. 5.2). The x-y plane, which contains the centerline of the vessel, may also be considered a symmetry plane since it is far enough from the nozzles to behave like a longitudinal plane in a long circular cylinder. It is thus possible to investigate the elastic behavior of the entire structure by modeling only the one-eighth section of the vessel illustrated in Fig. 5.3 and constraining all the nodal points lying in the three symmetry planes to remain in those planes.

The finite-element model for WC-12DD generated by FEMG has 2351 nodes and 715 elements. The elements are three-dimensional isoparametric bricks with 8 to 16 nodes each. Figure 5.4 shows an isometric view of the model, and Figs. 5.5 and 5.6 show side and top views of the model, respectively. At the ends of the nozzle and the run, the model has one element through the wall thickness. As the transition region is approached, this representation is increased to four elements. The standard transition between the regions of higher and lower element densities is illustrated in Figs. 5.7 and 5.8.

The nodal mesh was generated in two stages. The first stage was for points on or near the nozzle, and the second was for points located on the vessel away from the nozzle. The first portion uses the r,θ,z coordinate system of Fig. 5.2 for locating nodal points. The second portion lays out a regular, rectangular gridwork on the surface of the vessel.

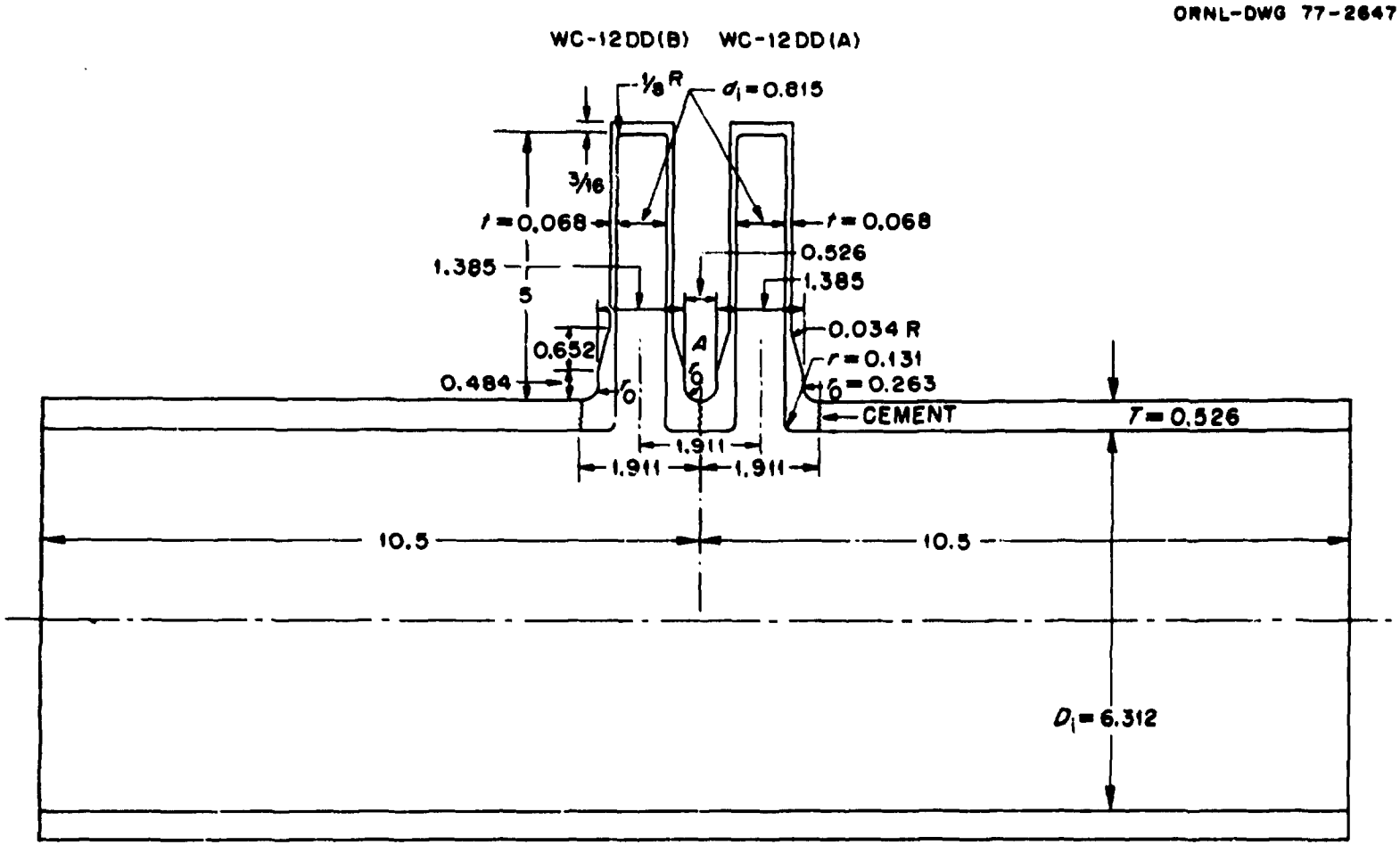

Fig. 5.1. Shape and dimensions for WC-12DD; dimensions are in inches.

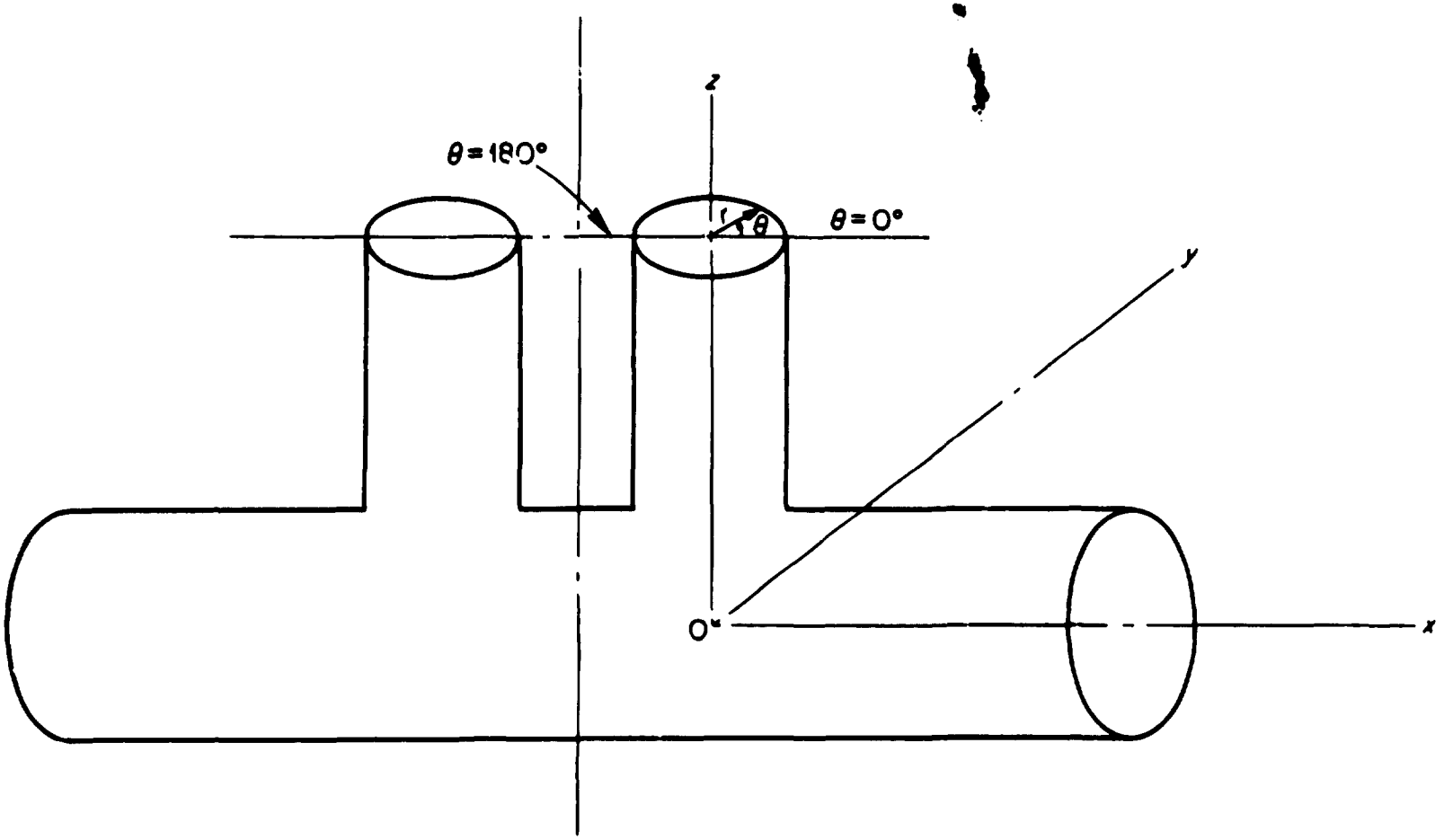

Fig. 5.2. Coordinate system used for WC-12DD and WC-100DD.

ORNL-DWG 77-2646

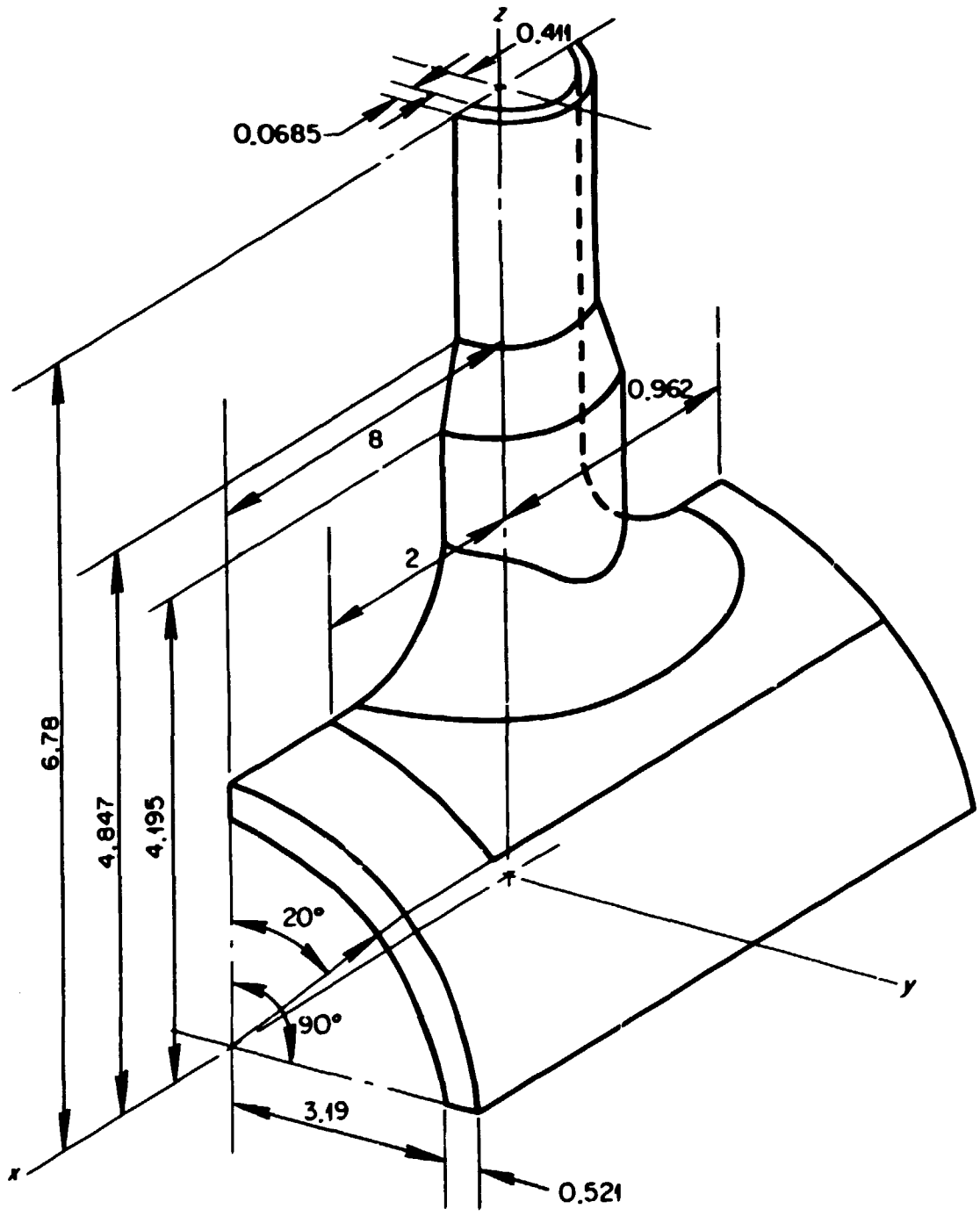

Fig. 5.3. Sector of WC-12DD for finite-element model. Dimensions are in inches.

ORNL-DWG 77-2675

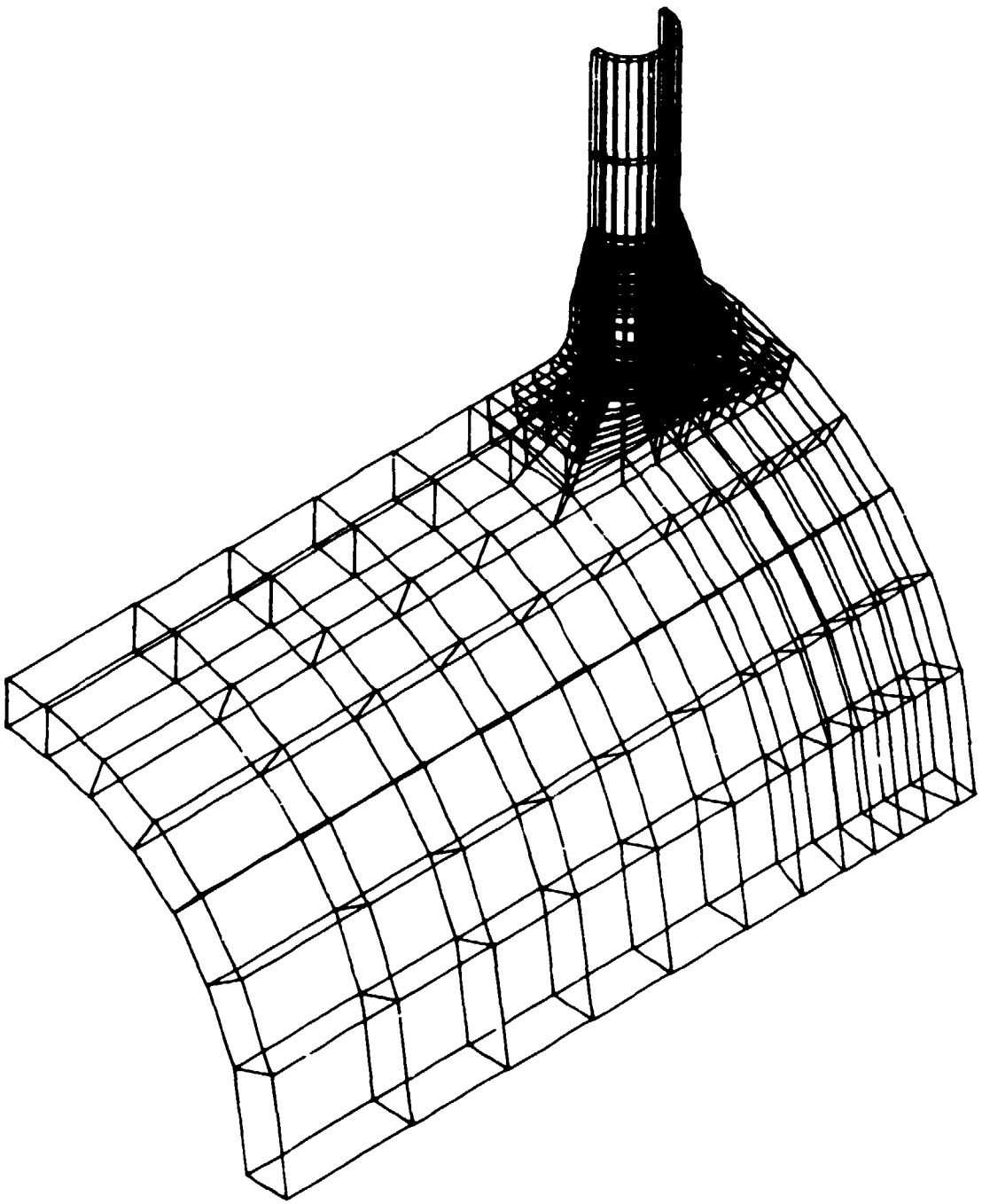

Fig. 5.4. Isometric view of the finite-element model for WC-12DD.

ORNL-DWG 77-2674

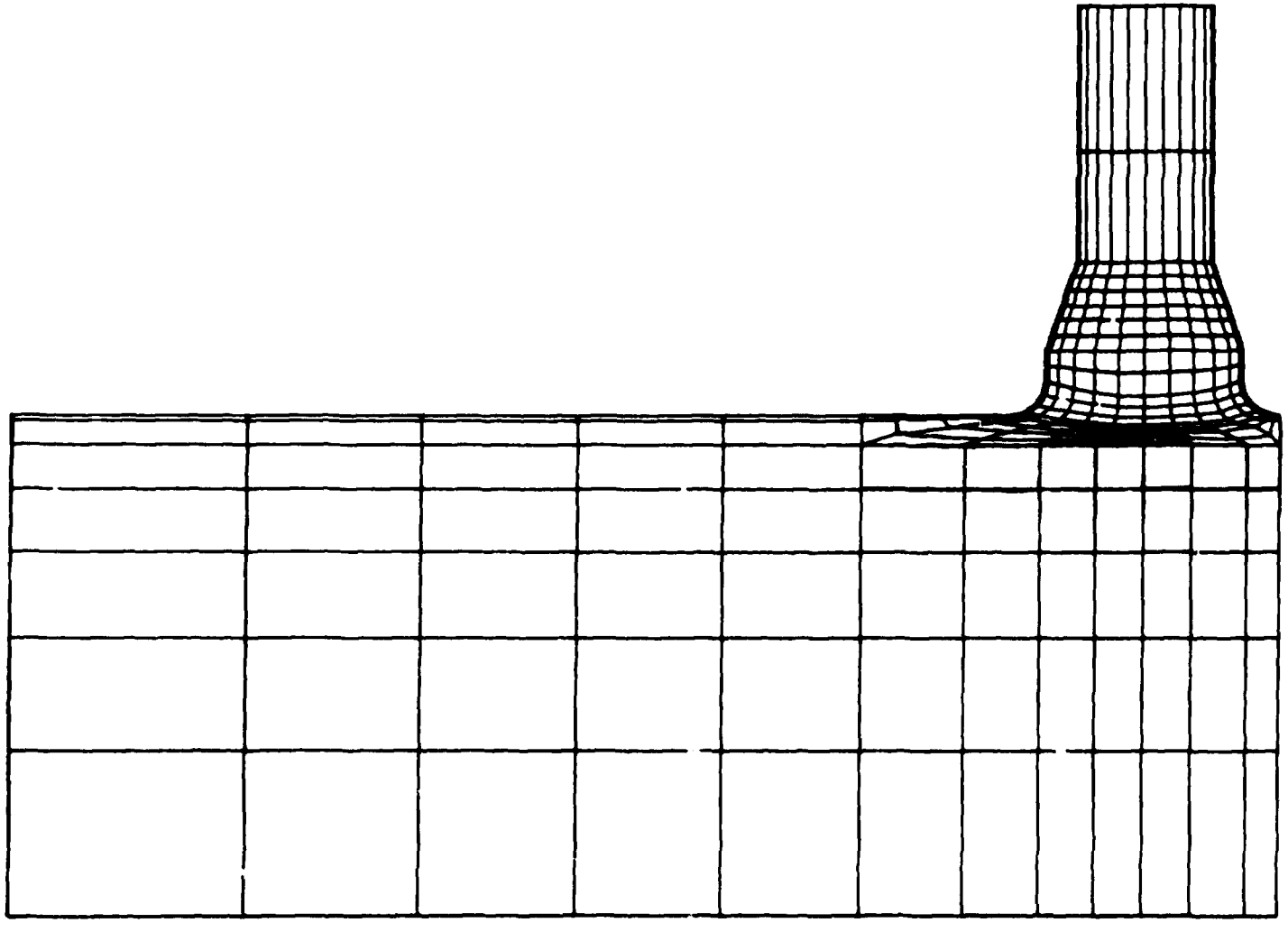

Fig. 5.5. Side view of the finite-element model for WC-12DD.

ORNL-DWG 77-2673

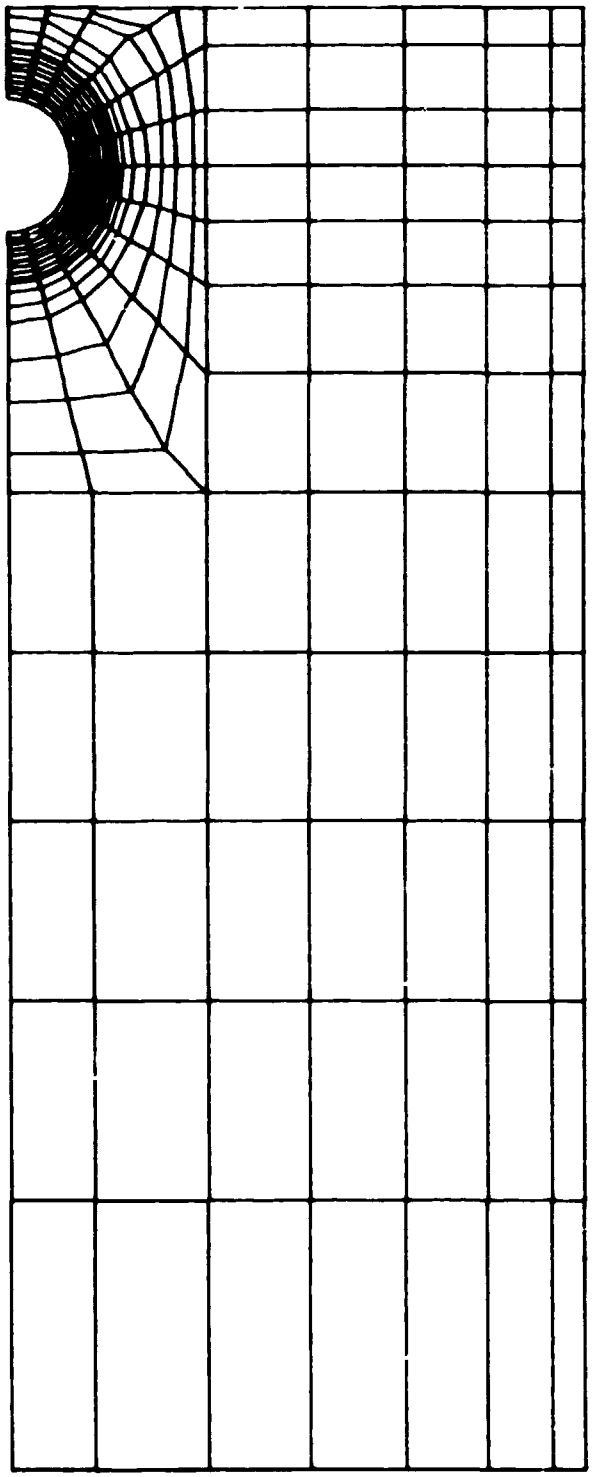

Fig. 5.6. Top view of the finite-element model for WC-12DD.

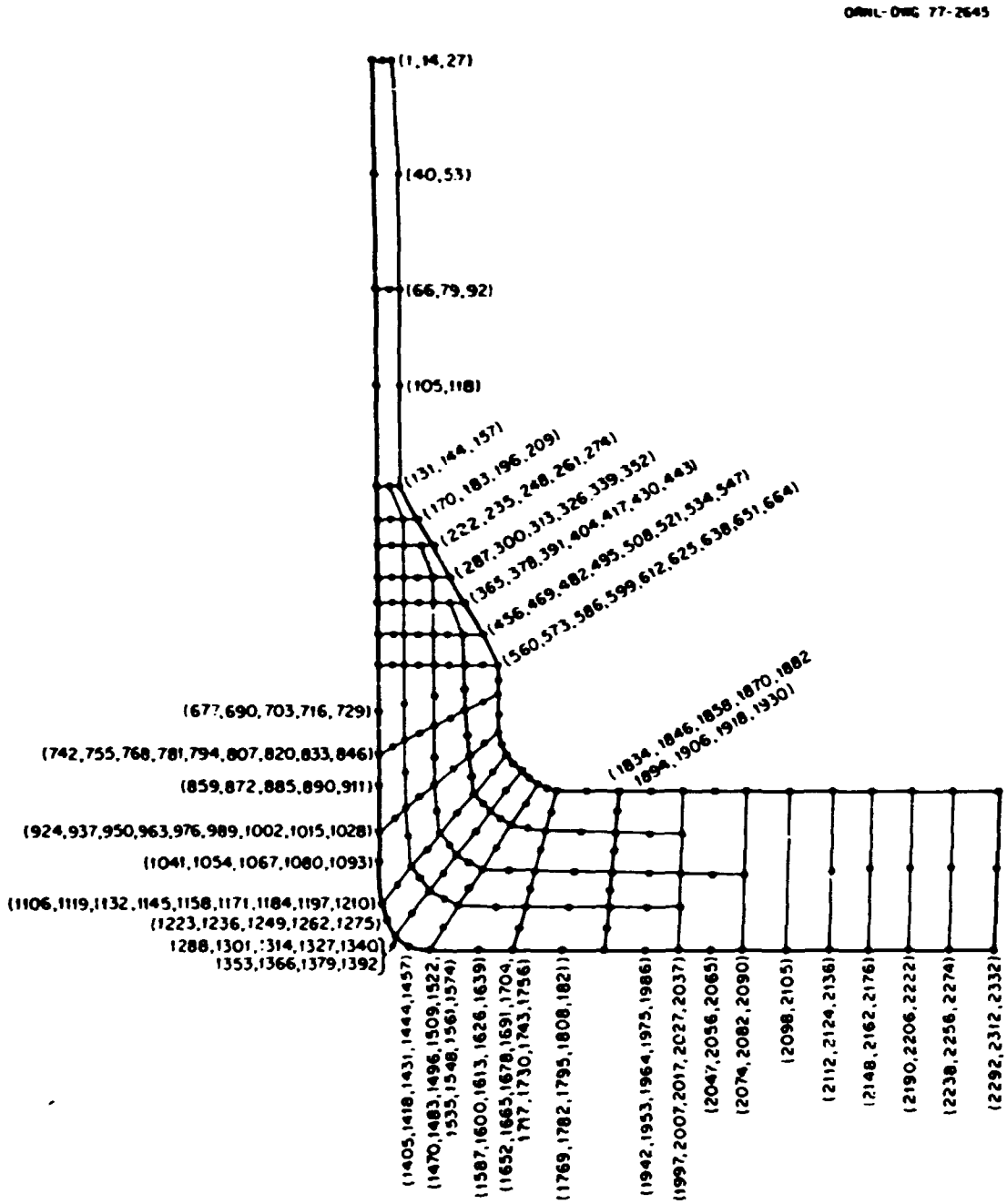

Fig. 5.7. Numbering of nodes for WC-12DD in the longitudinal plane (0°).

ORNL-DWG 77-2629

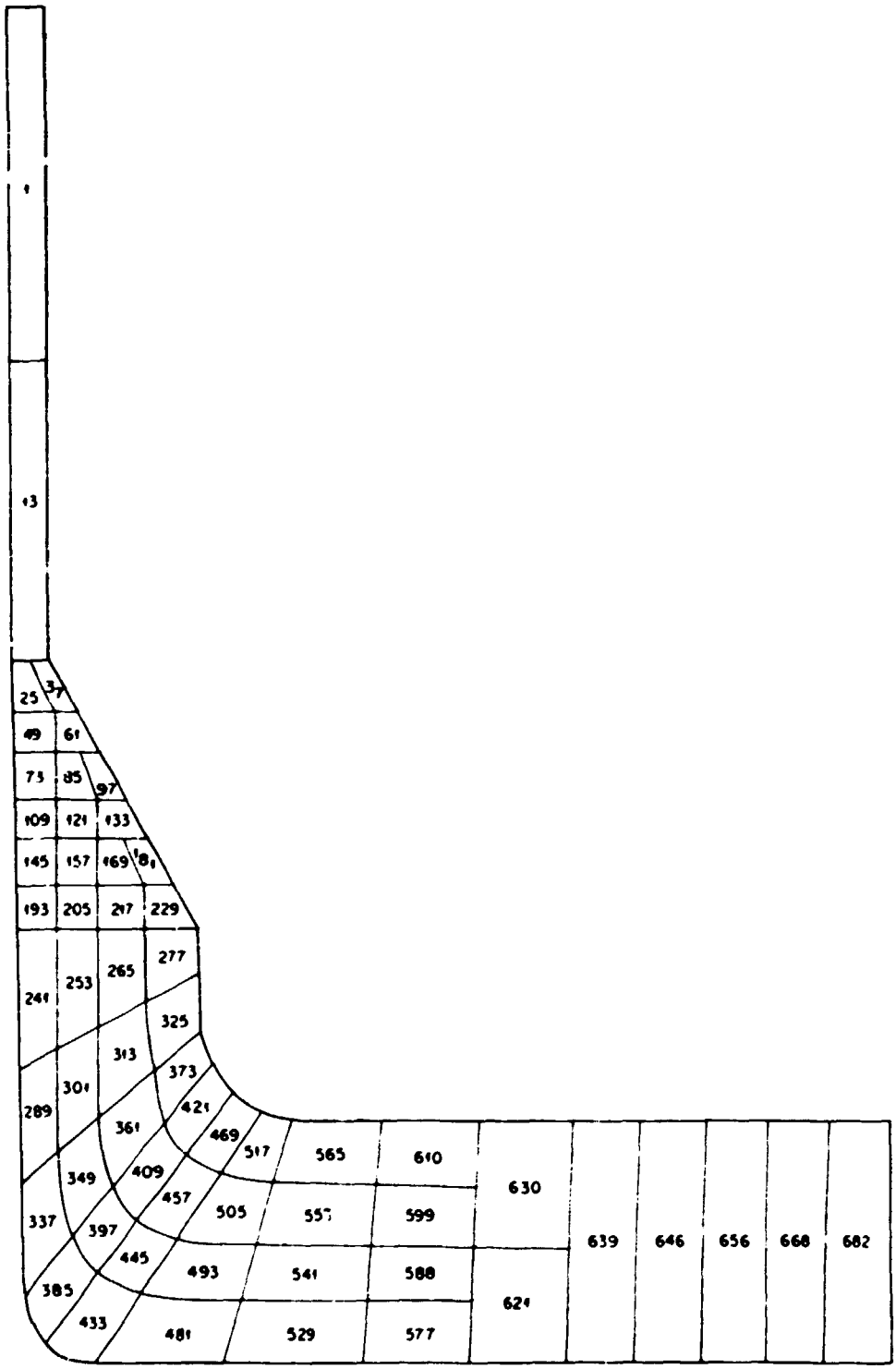

Fig. 5.8. Numbering of elements for WC-12DD in the longitudinal plane (0°).

The node numbering begins at the top of the nozzle at $\theta = 0°$ on the inside surface. Node identification numbers are then incremented for increasing values of θ, increasing values of r, and decreasing values of z, respectively. This radial numbering scheme is then extrapolated onto the rectangular mesh of the vessel. Element identification numbers are assigned in the same manner. Figures 5.7 and 5.8 illustrate the numbering of nodes and elements, respectively, in part of a cross section of the model. Figure 5.9 shows the local node point numbering scheme for the different elements in the two portions of the mesh.

5.2 Stress Analysis

The vessel was analyzed for a uniform internal-pressure load of 0.151 psi, which is the load necessary to create a maximum principal stress of 1 psi in a long cylinder having the nominal dimensions of the vessel. The effect of placing pressure caps on the ends of the vessel and nozzle was simulated by applying statically equivalent sets of axial force loads on the open ends of the model.

Isotropic material properties were originally selected to approximate those of the photoelastic materials used by Leven.[25] These are a Young's modulus (E) of 7500 psi and a Poisson's ratio (ν) of 0.485. This value of Poisson's ratio is very large and corresponds to the behavior of a nearly incompressible material, whereas most materials of practical engineering value have a Poisson's ratio in the vicinity of 0.3. Furthermore, large values of Poisson's ratio often lead to numerical problems in finite-element analyses. Computationally, the global stiffness matrix becomes progressively more ill-conditioned as ν is increased until it becomes singular at $\nu = 0.5$.[26] Analyses were therefore made using both values of Poisson's ratio, $\nu = 0.3$ and $\nu = 0.485$.

Both 2×2×2 and 3×3×3 integration rules were used. The reduced integration rule gave essentially the same results as the 3×3×3 integration with slightly less computer time.

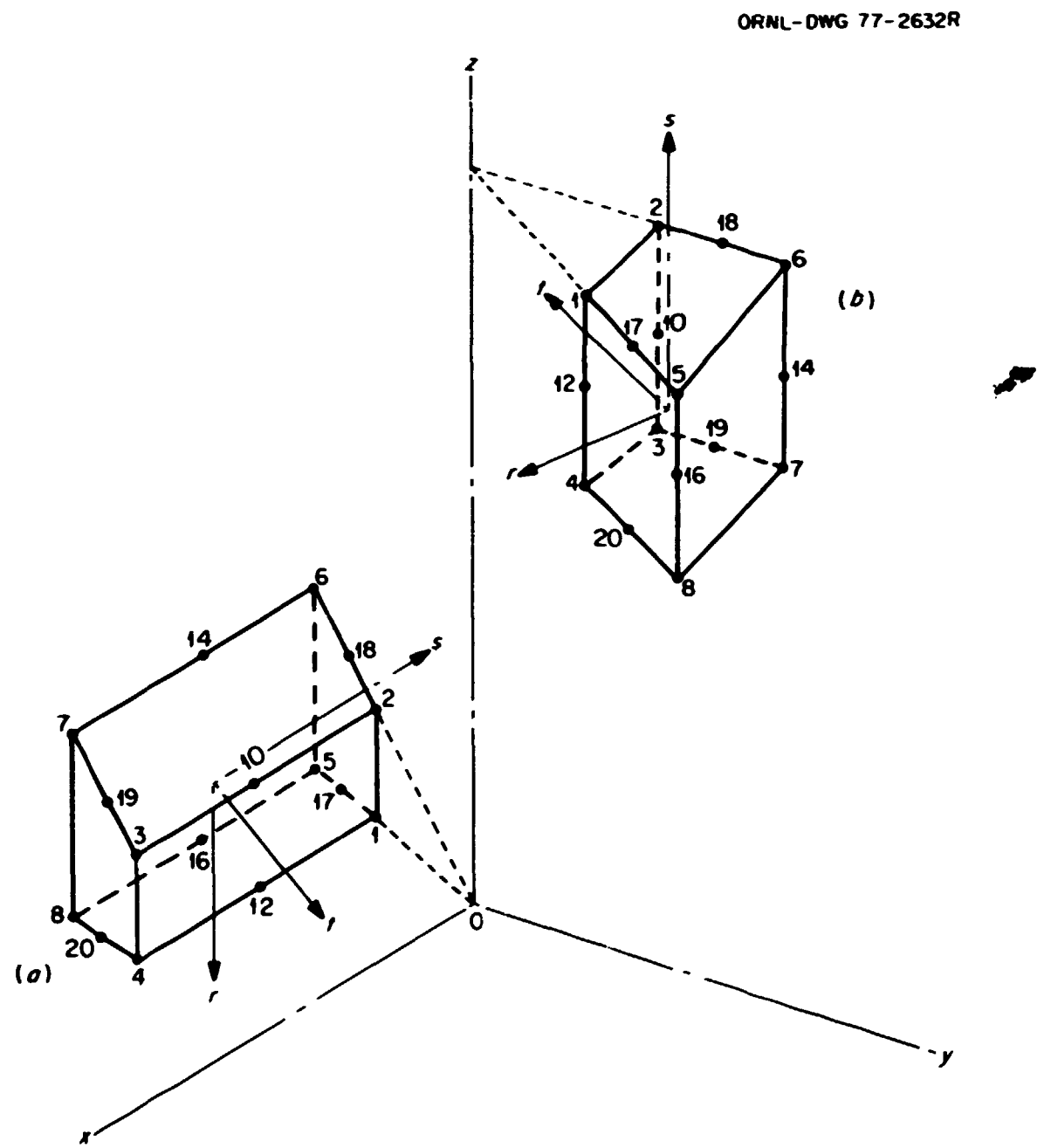

Fig. 5.9. Nodal sequence for elements (longitudinal nozzle configuration): (*a*) elements in vessel zone; (*b*) elements in nozzle zone.

5.3 Results

Selected summaries from the finite-element calculations for WC-12DD are shown in Fig. 5.10 for the 0° section, Fig. 5.11 for the 90° section, and Fig. 5.12 for the 180° section between the two nozzles along with data from Leven's photoelastic tests. Tabulations of the calculated stresses corresponding with the values plotted in the figures are given in the appendix. Calculated stresses normal to the plane of the sections (σ_n) shown in the figures are given for three cases: for $\nu = 0.3$ using 3×3×3 integration; for $\nu = 0.485$ using 2×2×2 integration; and for $\nu = 0.485$ using 3×3×3 integration.

Figures 5.10 through 5.12 show reasonably good agreement between all three of the finite-element analyses and the photoelastic data. In each case the general shape of the stress distributions and the locations of the maximum stresses were well represented. Better agreement, however, was obtained when $\nu = 0.3$ than when $\nu = 0.485$, both with respect to the overall smoothness and the maximum values. A comparison between the photoelastic and calculated maximum hoop stress at the inside corner of the nozzle (180° section) is shown in Table 5.1.

The two runs for $\nu = 0.485$ indicate that the results were not strongly dependent on the integration order. In general, however, the plots show

Table 5.1. Comparison between experimental and analytical maximum hoop stress index at inside nozzle corner for WC-12DD

	Photoelastic data	Finite-element results		
		$\nu = 0.3$ (2×2×2)	$\nu = 0.485$ (2×2×2)	$\nu = 0.485$ (3×3×3)
$(\sigma_n/S)^a$	2.96	2.96	2.34	2.38
Error		0%	21%	20%

[a] S = nominal stress = $p\,(D_i + T)/2T$, where D_i and T are the inside diameter and wall thickness of the vessel, respectively.

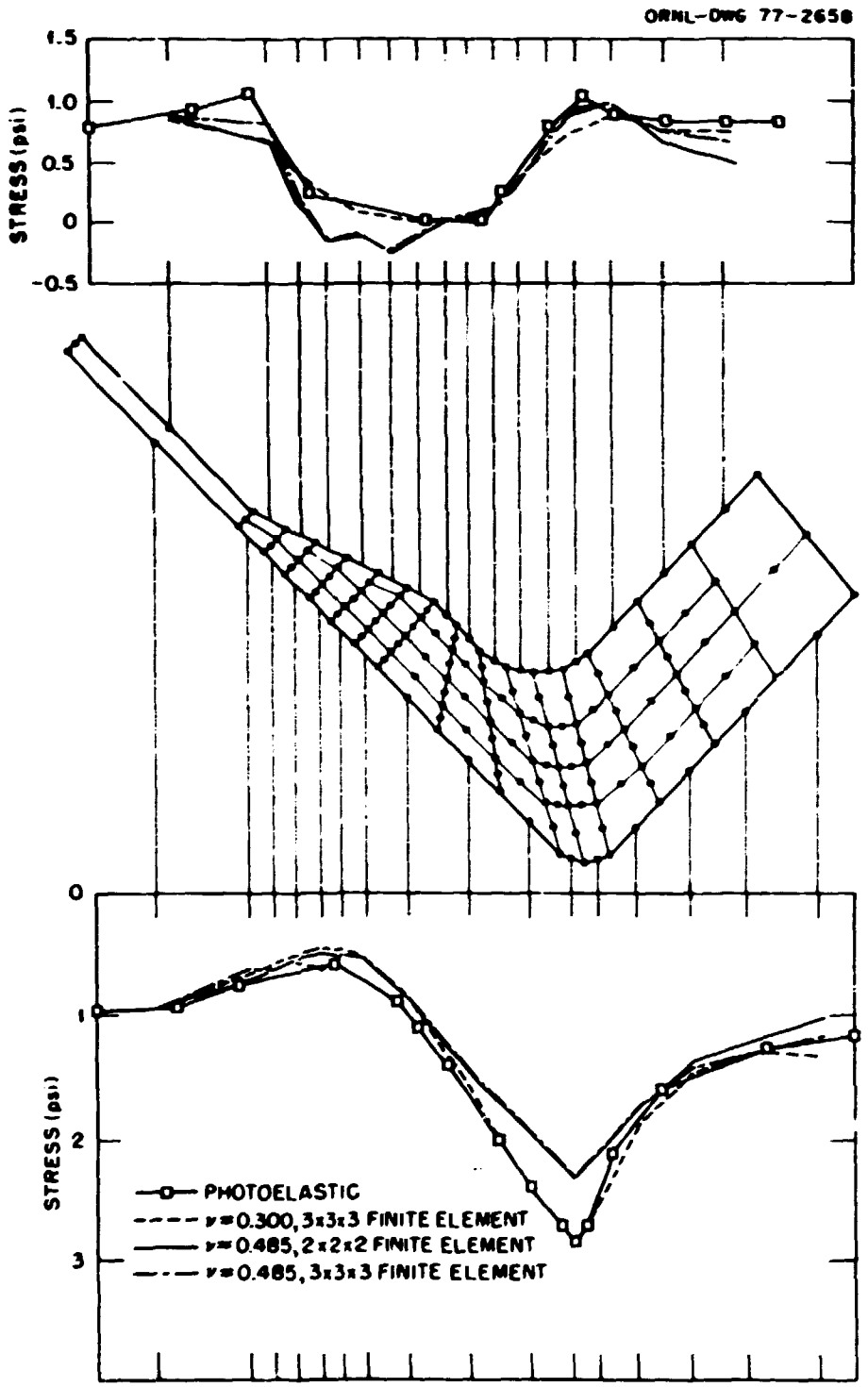

Fig. 5.10. Comparison of photoelastic and calculated normal stress distributions on WC-12DD for 0° section, internal pressure load = 0.151 psi.

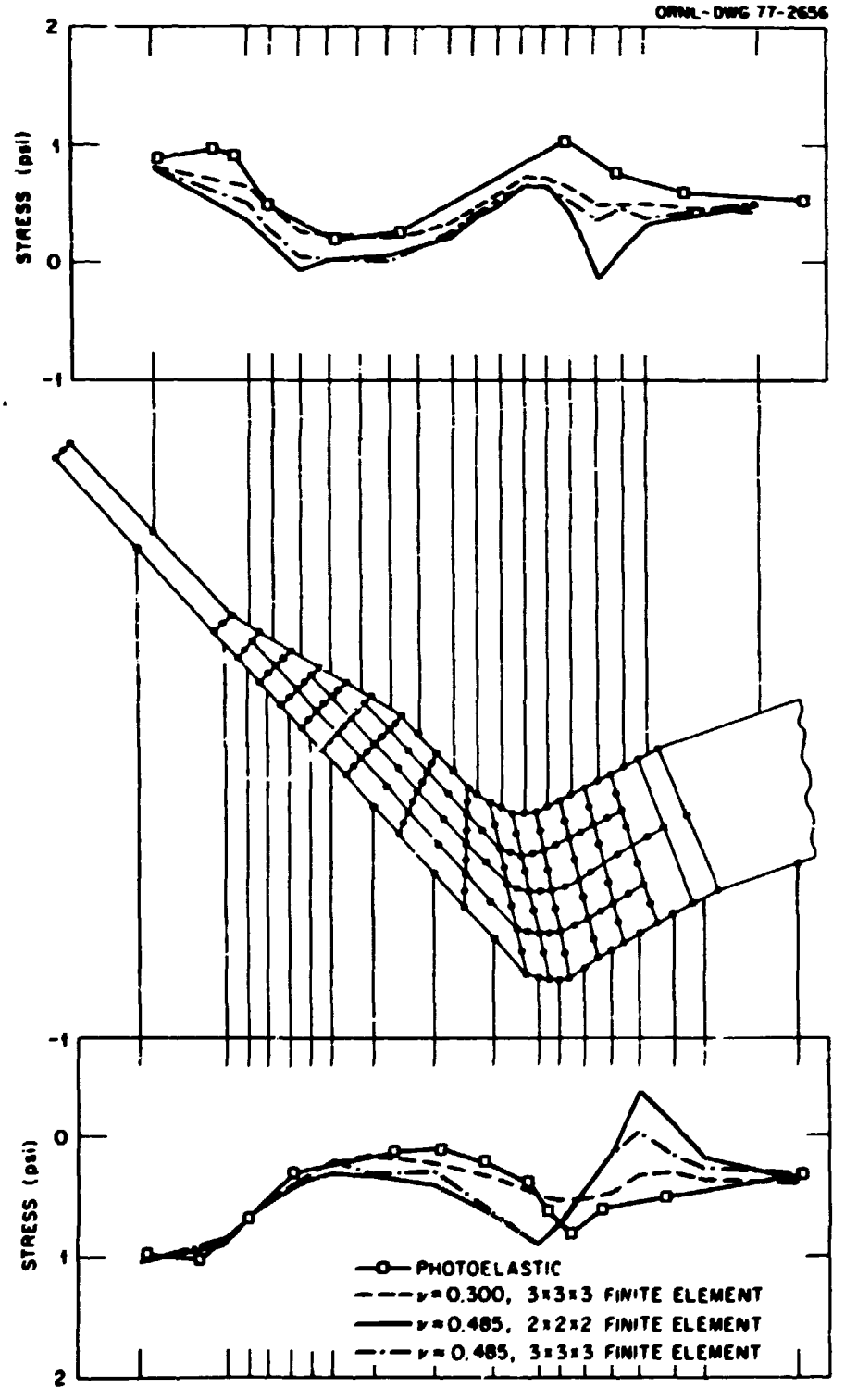

Fig. 5.11. Comparison of photoelastic and calculated normal stress distributions on WC-12DD for 90° section, internal pressure load = 0.151 psi.

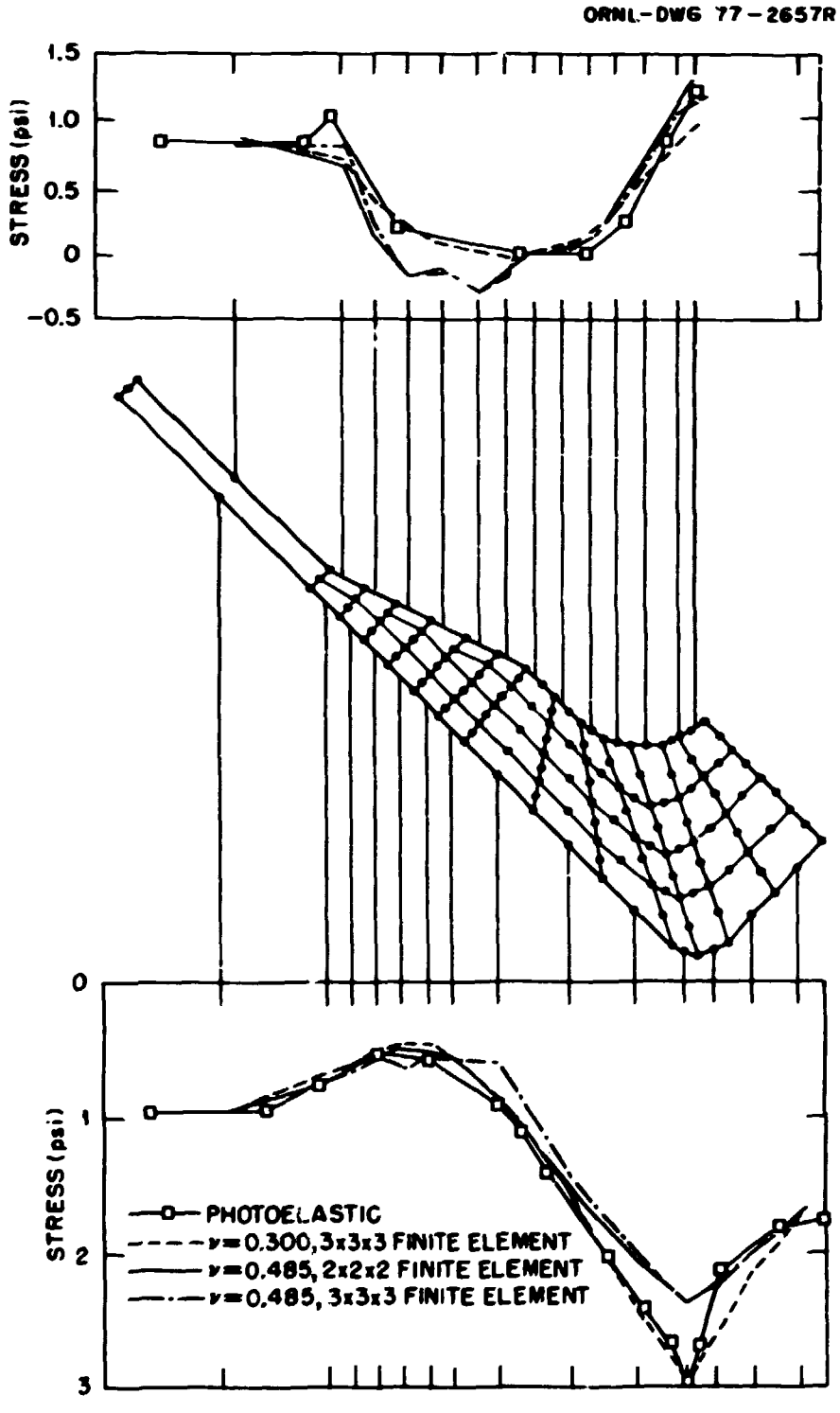

Fig. 5.12. Comparison of photoelastic and calculated normal stress distributions on WC-12DD for 180° section, internal pressure load = 0.151 psi.

smoother distributions and somewhat better agreement with the experimental data for the lower order integration. The exception is for the 90° section, where the 3×3×3 integration gave better agreement than the 2×2×2 integration. For both integration orders, when $\nu = 0.485$, the stress distributions along the outer surface at the nozzle taper appear to be irregular. This may have been caused (or exaggerated) by the incompatible displacement model introduced into the finite element model by reducing the element density in this region.

6. ANALYSIS OF PRESSURE VESSEL MODEL WC-100DD

This chapter describes the finite-element analysis of a thin-walled cylindrical vessel with two closely spaced thin-walled nozzles located in a longitudinal plane, identified as Westinghouse photoelastic model WC-100DD and analyzed experimentally by Leven.[15] A sketch of this model is shown in Fig. 6.1.

6.1 Finite-Element Model

The symmetry of WC-100DD is similar to that of WC-12DD discussed in the previous chapter and therefore, again, it is only necessary to model the one-eighth section of the vessel shown in Fig. 6.2. The finite-element model for WC-100DD generated by FEMG had 1131 nodes and 290 three-dimensional isoparametric 8- to 16-node elements. Figure 6.3 shows an isometric three-dimensional view of the model. Figures 6.4 and 6.5 are the side and top views of the model, respectively. Variable nodal densities were used, with one element representing the wall thickness at the nozzle and vessel ends and two elements representing the wall thickness in the junction region as indicated in Figs. 6.6 and 6.7.

The nodal mesh was generated in two stages, as was done for model WC-12DD. The same coordinate systems and similar schemes for numbering the nodes and elements were also used. Figures 6.6 and 6.7 illustrate the numbering of nodes and elements. Identification of the local nodal point numbering scheme for the elements in the two portions of the mesh is the same as for WC-12DD, shown earlier in Fig. 5.9.

6.2 Stress Analysis

The model was analyzed for an internal-pressure load of 0.0195 psi to normalize the maximum principal stress in the vessel to unity. The effect of placing pressure caps on the ends of the vessel and nozzle was simulated by applying statically equivalent nodal forces on the open ends of the model.

ORNL-DWG 77-2630

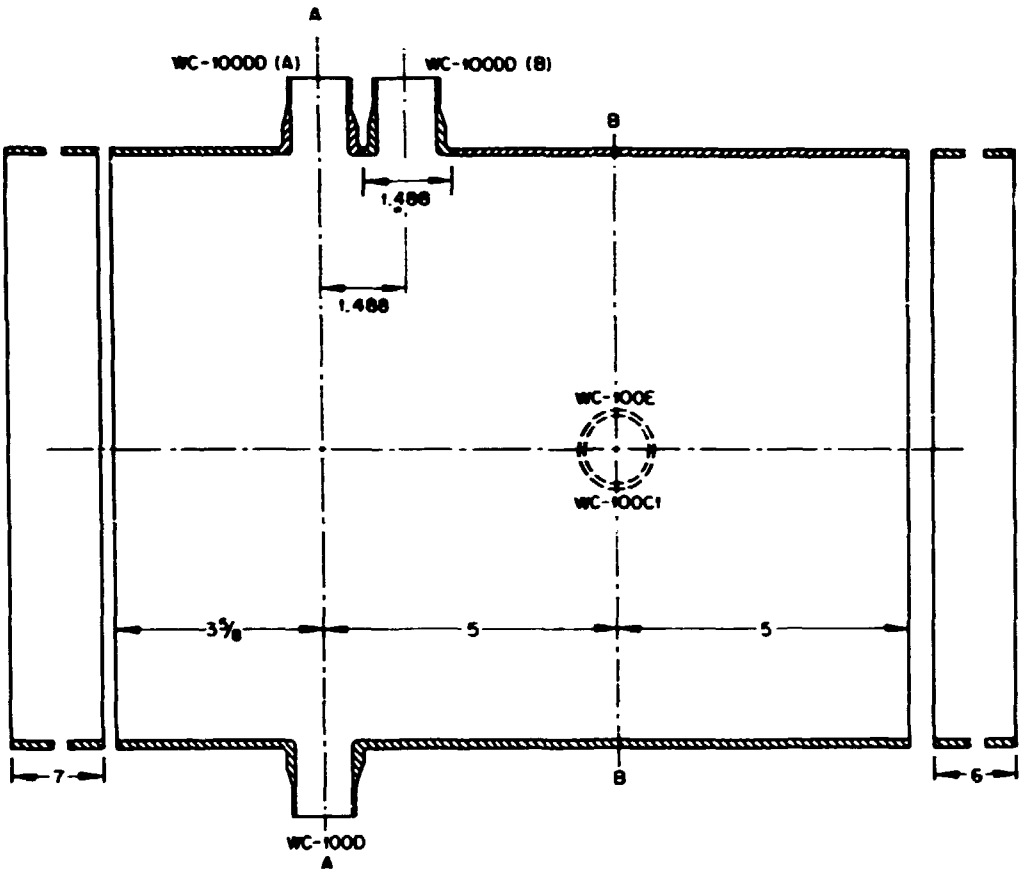

DIMENSIONS IN INCHES

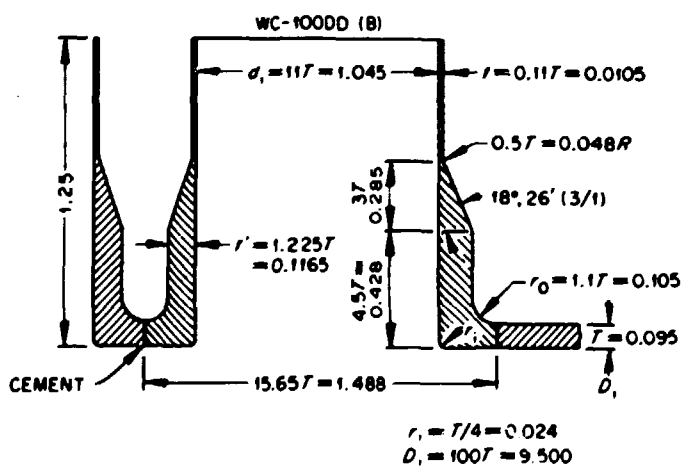

Fig. 6.1. Shape and dimensions for WC-100DD; dimensions are in inches.

ORNL-DWG 77-2631

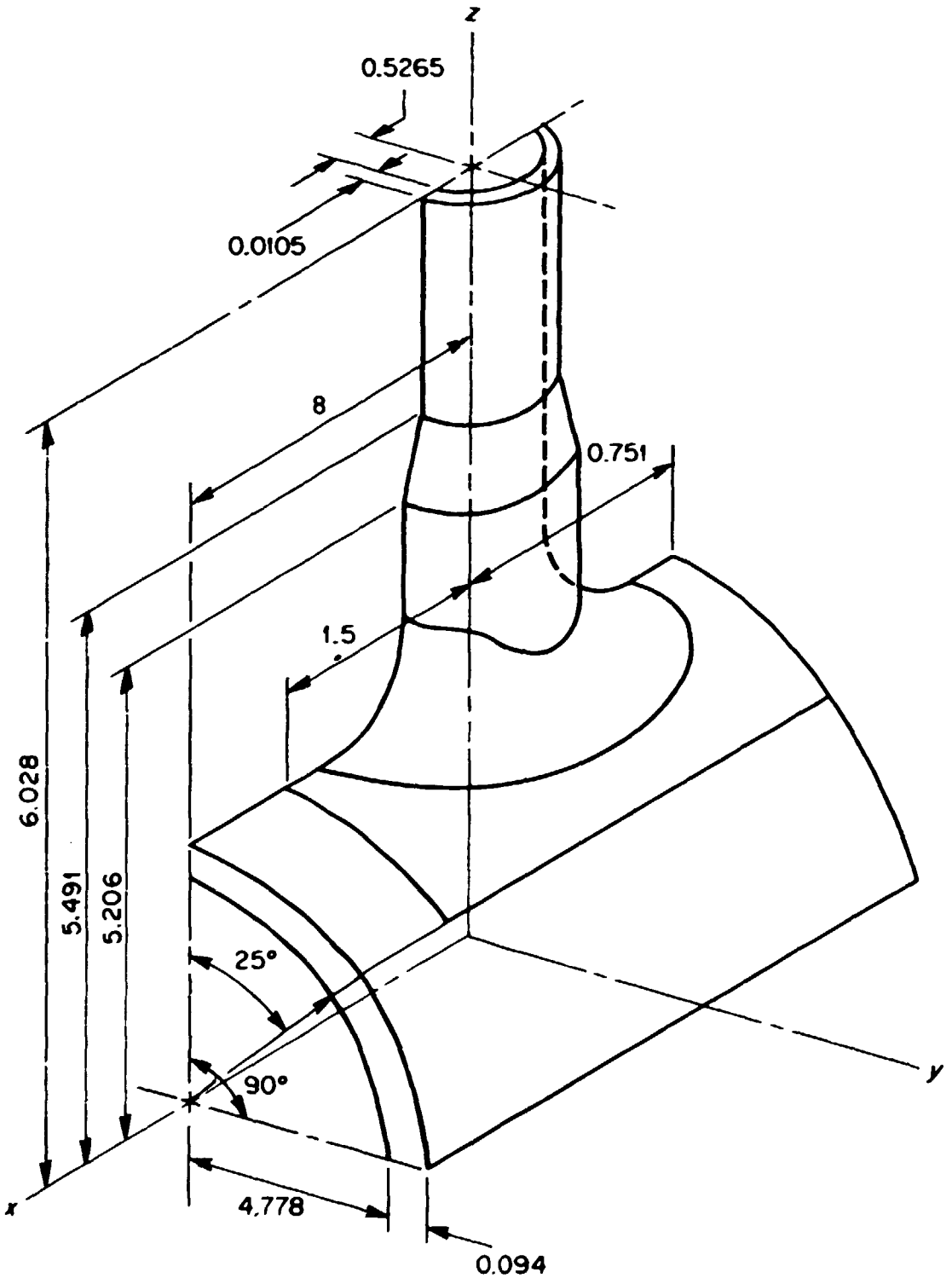

Fig. 6.2. Sector of WC-100DD for finite-element model. Dimensions are in inches.

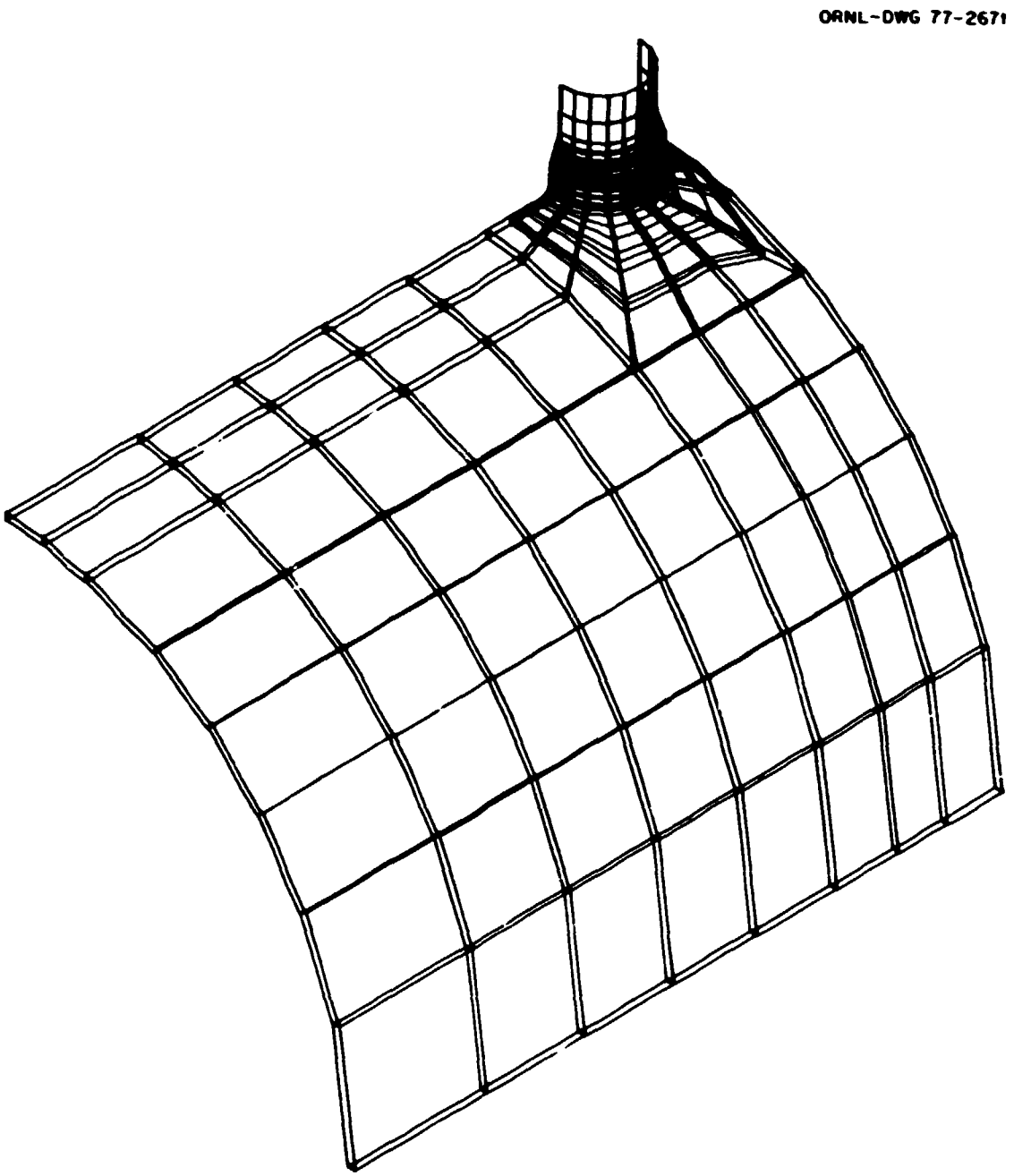

Fig. 6.3. Isometric view of the finite-element model for WC-100DD.

ORNL-DWG 77-2670

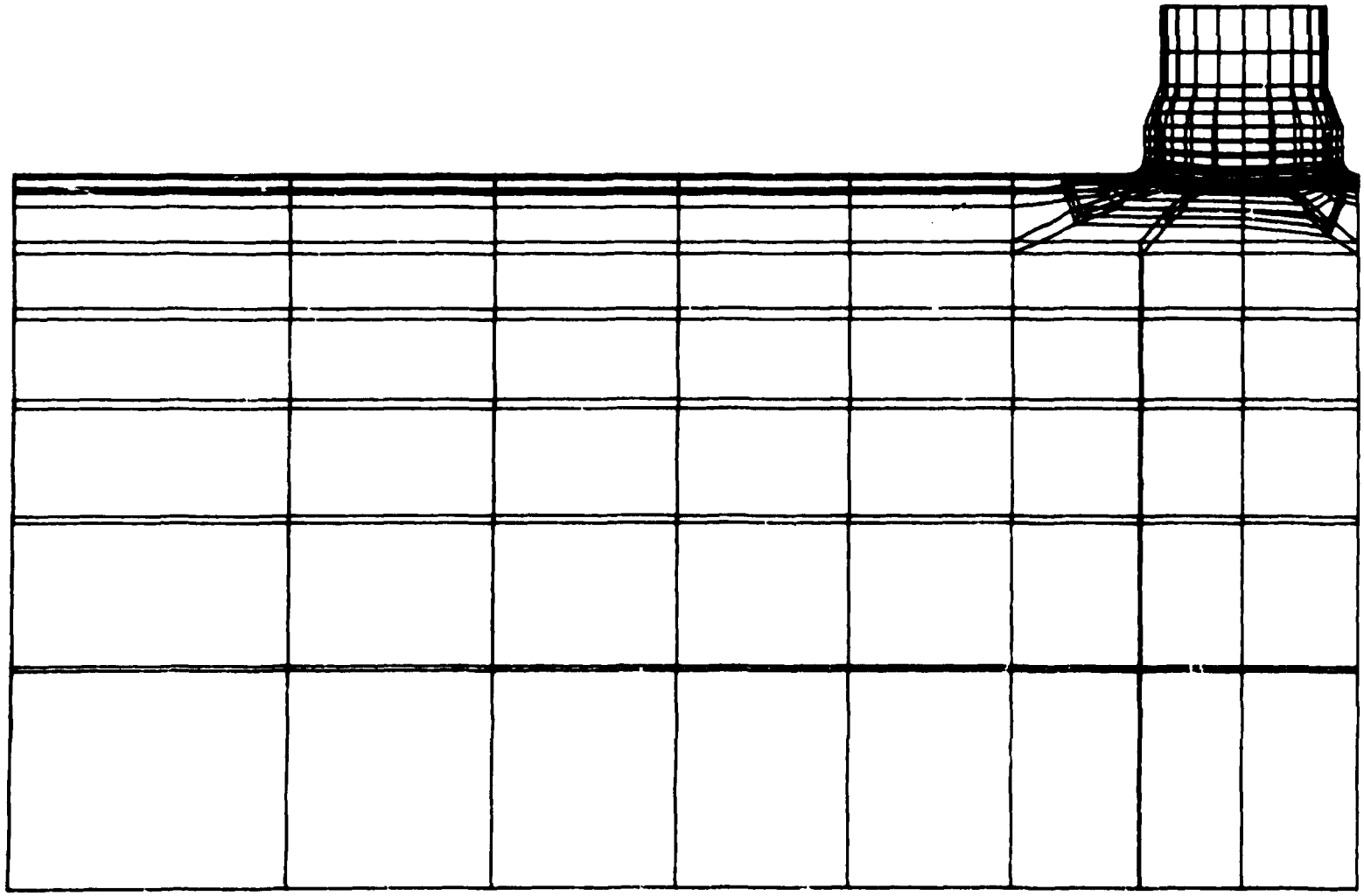

Fig. 6.4. Side view of the finite-element model for WC-100DD.

ORNL-DWG 77-2669R

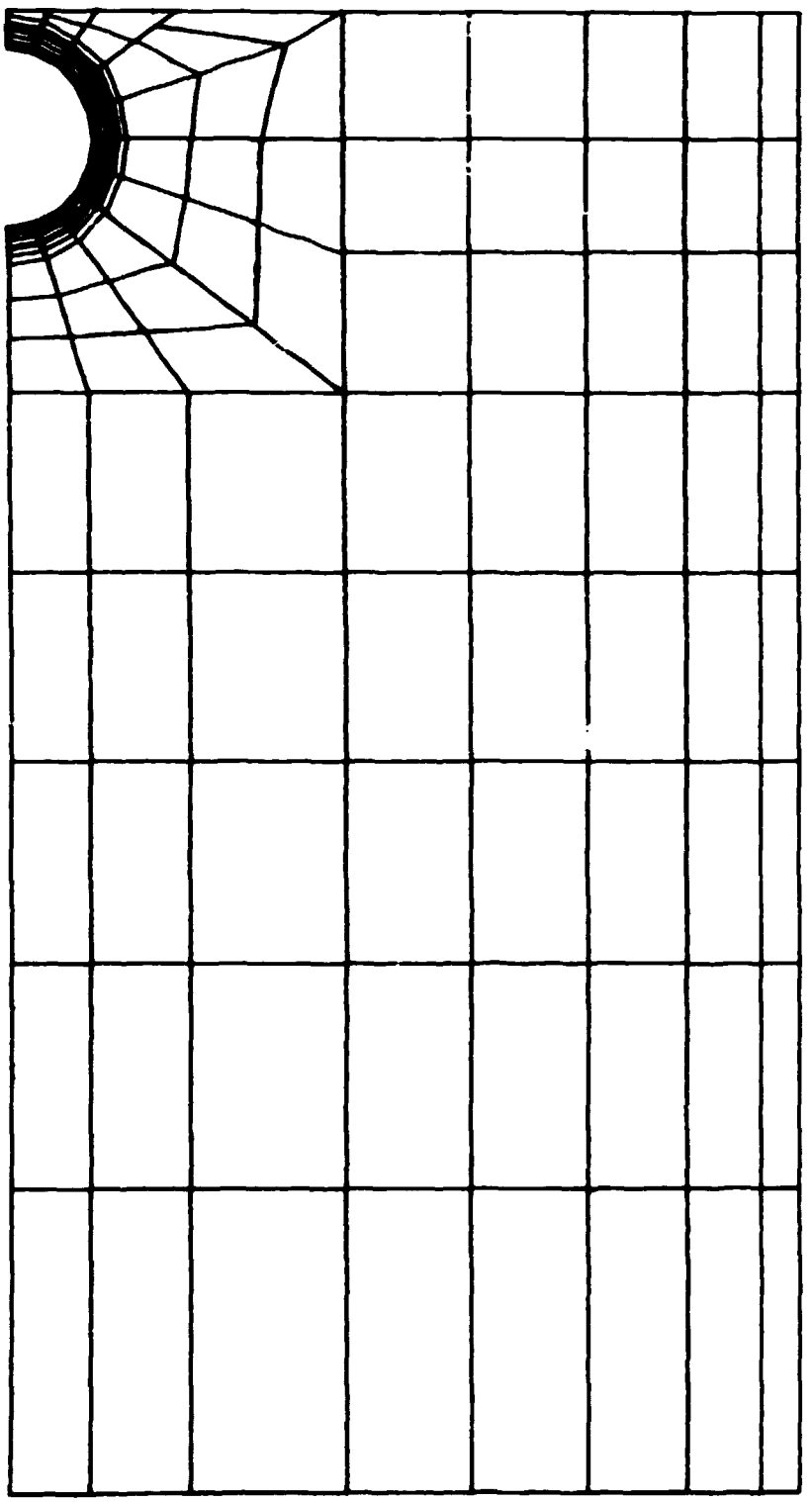

Fig. 6.5. Top view of the finite-element model for WC-100DD.

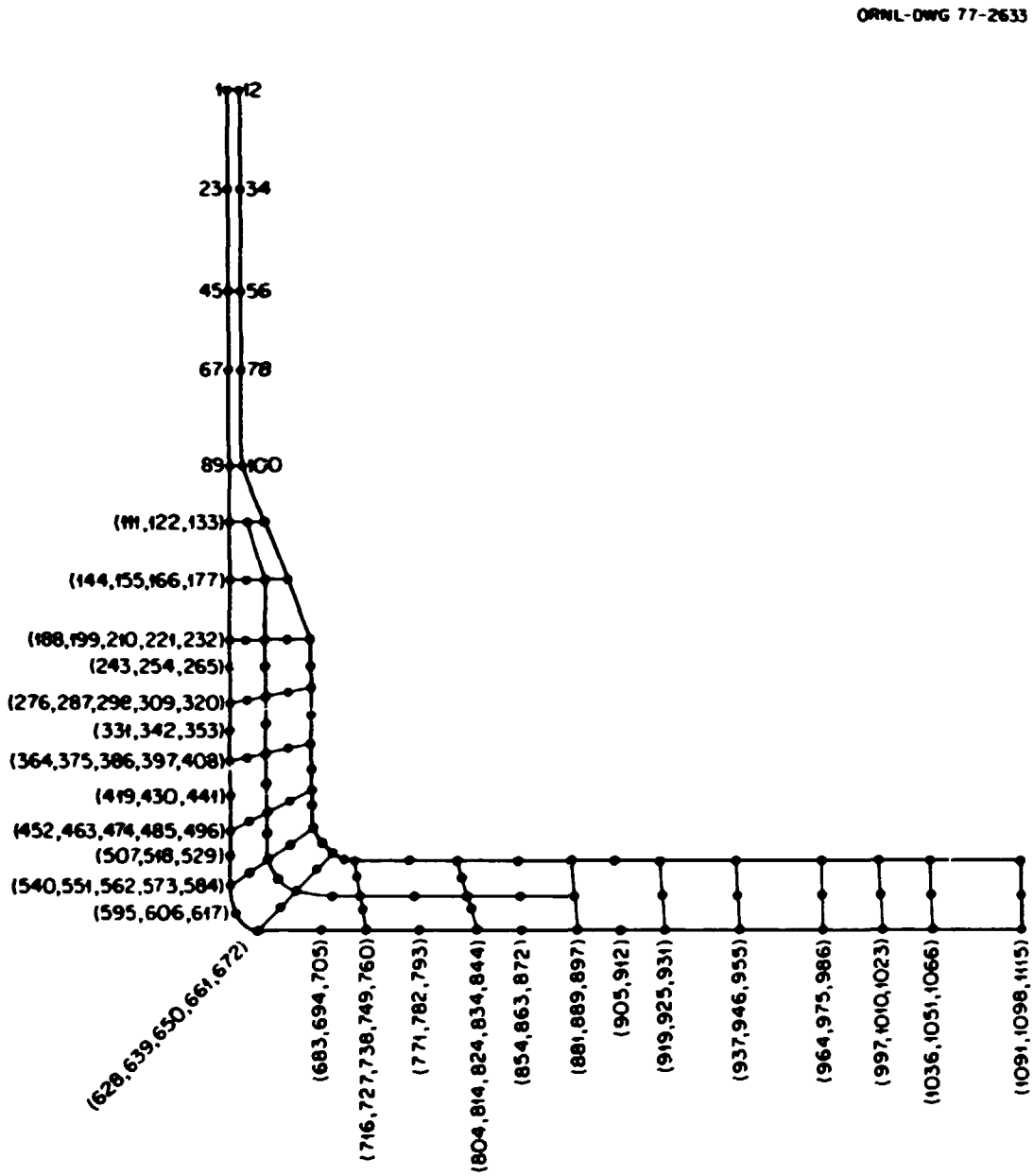

Fig. 6.6. Numbering of nodes for WC-100DD on the longitudinal plane (0°).

ORNL-DWG 77-2634

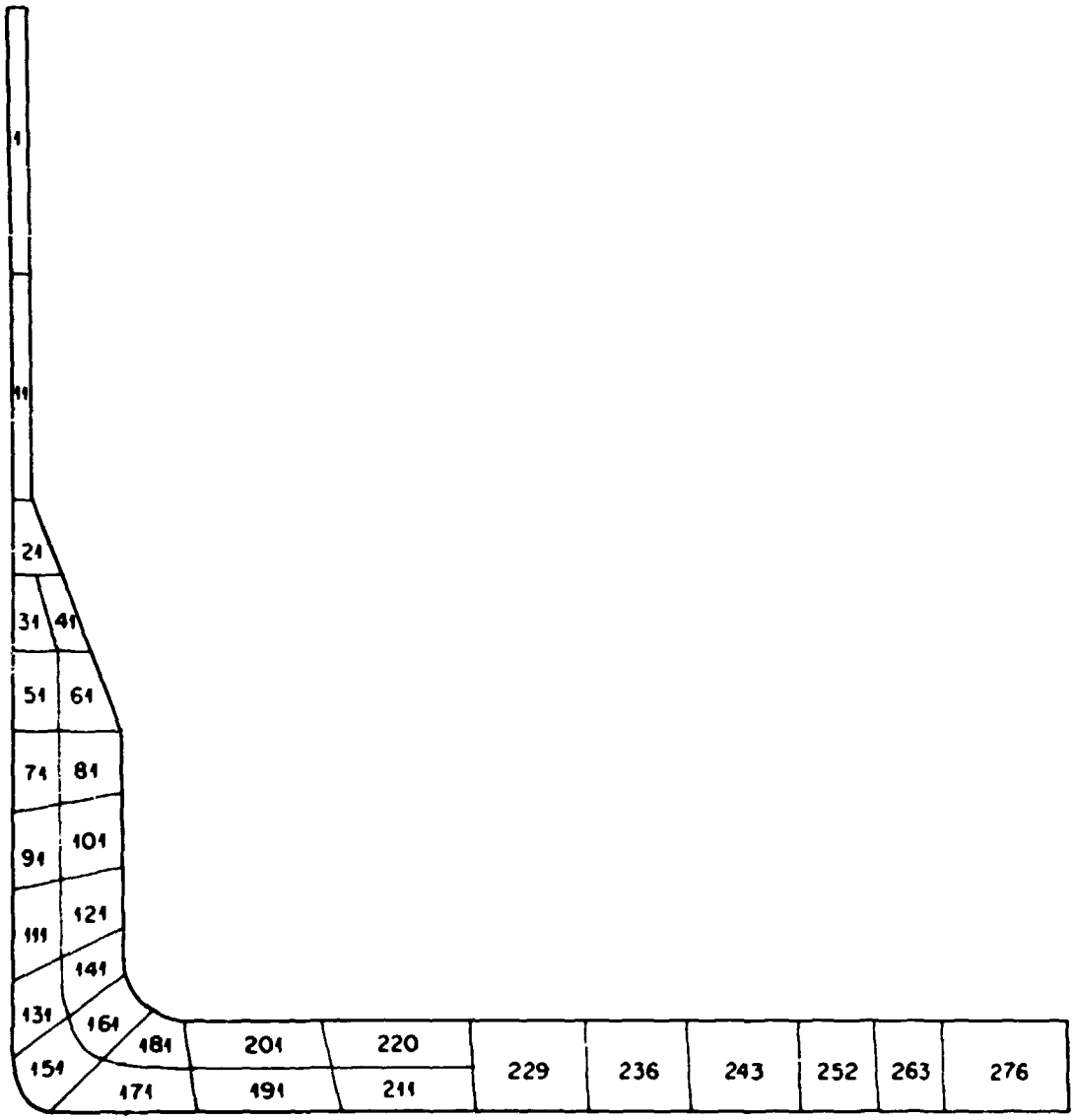

Fig. 6.7. Numbering of elements for WC-100DD on the longitudinal plane (0°).

In order to study the sensitivity of the computer code to the material compressibility, three values of Poisson's ratio were considered: 0.3, 0.4, and 0.485. A Young's modulus of 7500 psi was used for all three calculations. The photoelastic test material was reported[25] to have E = 7500 psi and ν = 0.485.

6.3 Results

Five sets of computations were made for WC-100DD: for ν = 0.3, 0.4, and 0.485 using the reduced (2×2×2) integration; and for ν = 0.3 and 0.485 using the 3×3×3 integration. Calculated values for the σ_n stresses normal to the 0 and the 90° sections, and to the 180° section between the two nozzles are tabulated in the appendix. Selected summaries are shown in Table 6.1 and in Figs. 6.8, 6.9, and 6.10 along with data from Leven's photoelastic tests.

In general, the finite-element results agree fairly well with the photoelastic data, as shown in Figs. 6.8 through 6.10. The two notable exceptions are for results obtained using ν = 0.485. These are for the inside surface at 90° (Fig. 6.9), where the calculated stresses near the

Table 6.1. Comparison between experimental and analytical maximum hoop stress index[a] at inside nozzle corner for WC-100DD

Experimental results	Integration order	Finite-element results		
		ν = 0.3	ν = 0.4	ν = 0.485
3.00	(2×2×2)	2.765 (7.8%)[b]	2.673 (10.9%)	2.110 (29.7%)
	(3×3×3)	2.759 (8.0%)		2.119 (29.4%)

[a]The hoop stress index = (σ_n/S), where the nominal stress $S = p(D_i + T)/2T$, and D_i and T are the inside diameter and wall thickness of the vessel, respectively.

[b]Percentage error for the calculated values are given in parentheses.

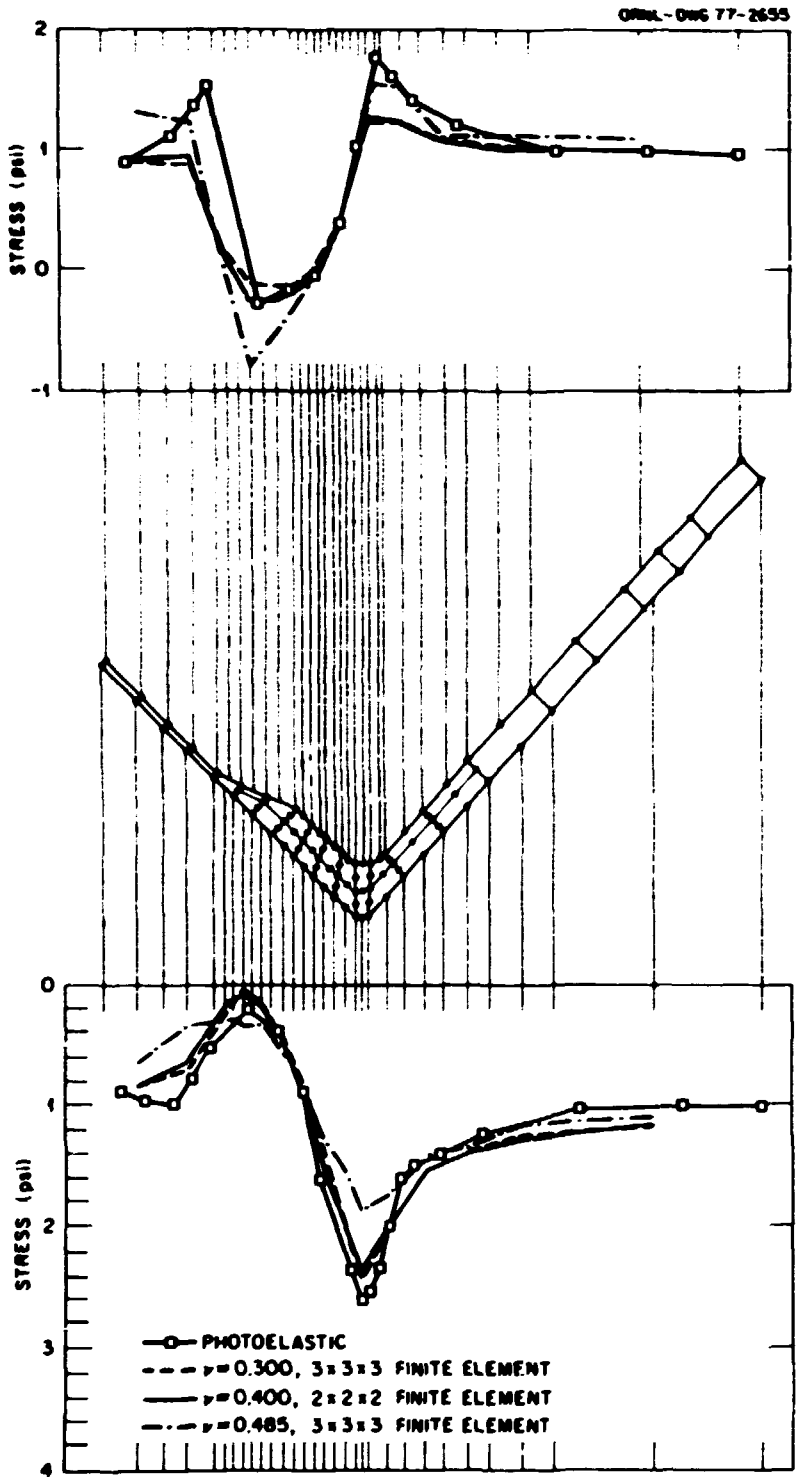

Fig. 6.8. Comparison of photoelastic and calculated normal stress distributions on WC-100DD for 0° section, internal pressure load = 0.0195 psi.

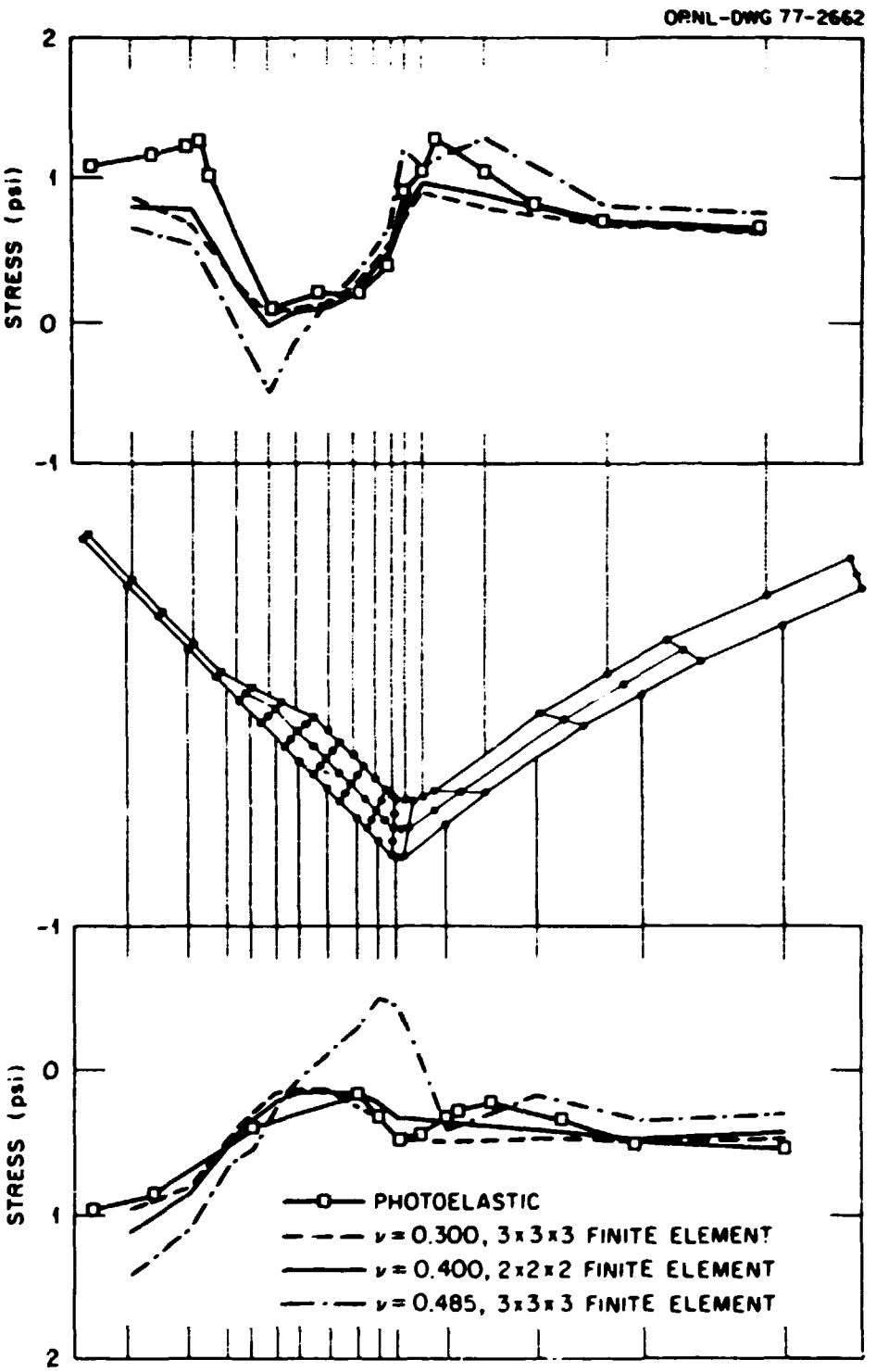

Fig. 6.9. Comparison of photoelastic and calculated normal stress distributions on WC-100DD for 90° section, internal pressure load = 0.0195 psi.

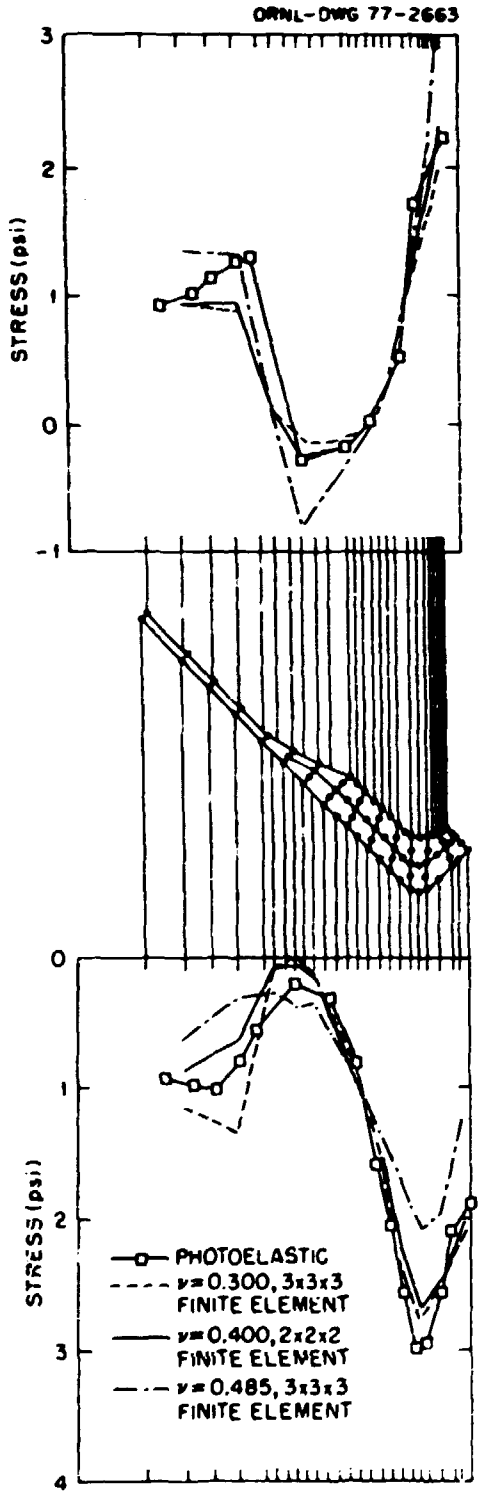

Fig. 6.10. Comparison of photoelastic and calculated normal stress distributions on WC-100DD for 180° section, internal pressure load = 0.0195 psi.

inside corner show a peculiar hump; and for the outside surface at 180° (Fig. 6.10), where the calculated maximum at the symmetry plane is considerably higher than the photoelastic data.

For $\nu = 0.3$, the finite-element data and the photoelastic data match very well. For this case, the discrepancy in the calculated maximum stress index is approximately 8% (2.77 vs 3.0) and occurs at the inside corner of the nozzle in the region between the two nozzles ($\theta = 180°$). Results for $\nu = 0.4$ also match well, where the calculated maximum stress index differed from the photoelastic data by approximately 11% (2.68 vs 3.0). For $\nu = 0.485$, the difference was about 30% (2.12 vs 3.0). As before, and as shown in Table 6.1, the integration order made very little difference.

Although the finite-element results for WC-100DD (using $\nu = 0.3$) generally agree with the photoelastic data, the overall agreement is not quite as good as was obtained for WC-12DD. This is the result of using three-dimensional isoparametric finite elements to analyze thin-walled structures, as pointed out in Refs. 27 and 28, and indicates that D/T ratios nearing 100 represent the upper limit for reliable application of the present program. The relatively large discrepancies in the finite-element results for $\nu = 0.485$ is undoubtedly due to the instability of the stiffness matrix as ν approaches 0.5 as discussed earlier. The relatively good agreement obtained for $\nu = 0.4$ (see Table 6.1), however, indicates that the behavior of the physical structure is not strongly affected by Poisson's ratio and thus tends to confirm the acceptability of using a value of $\nu = 0.3$ for analysis.

7. ANALYSIS OF PRESSURE VESSEL MODEL SH-23DD

This chapter describes the finite-element stress analysis of a cylindrical pressure vessel model with two identical closely spaced nozzles located in a circumferential, or transverse, plane. The model is intended to approximate the 26.4° spacing inlet-outlet pair of nozzles, identified as nozzles 24 and 23, respectively, in the photoelastic vessel analyzed by Stone and Hochschild.[16] Although nozzles 23 and 24 were not geometrically identical, as shown in Fig. 7.1, they were sufficiently alike that an analysis of an identical pair modeled after one or the other should compare reasonably well with the experimental data.

As shown in Table 7.1, the maximum experimental stresses reported by Stone and Hochschild for the two nozzles differed by about 10% in the longitudinal planes and by up to about 40% in the transverse plane. They

Table 7.1. Maximum experimental stresses[a] for Stone and Hochschild's nozzles 23 and 24

26.4° nozzle pair	Longitudinal plane				Transverse plane			
	Inside surface		Outside surface		Inside surface		Outside surface	
	σ_n/P	σ_t/P	σ_n/P	σ_t/P	σ_n/P	σ_t/P	σ_n/P	σ_t/P
Outlet (No. 23)	17.9	−1.0	9.6	6.2	4.4	−4.2	10.6	8.6
Inlet (No. 24)	16.1	−1.0	9.0	5.4	2.8	−4.4	12.1	12.1

[a] σ_n/P is the stress ratio normal to the plane of the photoelastic slice; σ_t/P is the stress ratio in the plane of the photoelastic slice. For the longitudinal plane, σ_n corresponds to a circumferential stress in both the nozzle and cylindrical vessel and σ_t corresponds to an axial stress. For the transverse plane, σ_n corresponds to a circumferential stress in the nozzle and an axial stress in the vessel whereas σ_t corresponds to an axial stress in the nozzle and a circumferential stress in the vessel.

ORNL DWG 77-16897

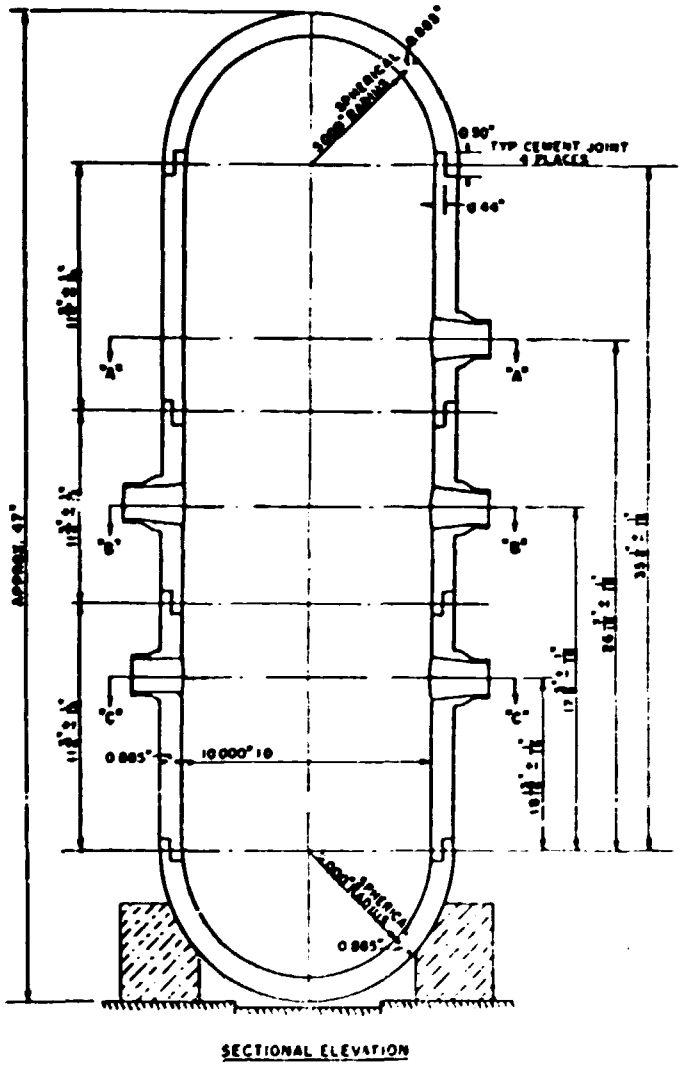

SECTIONAL ELEVATION

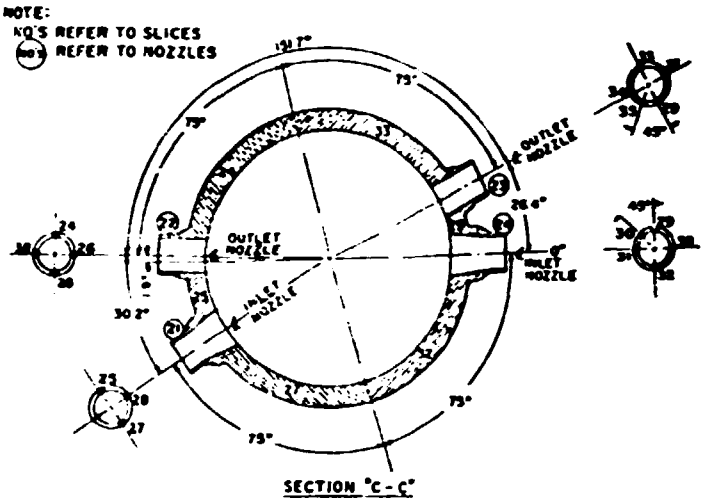

SECTION "C-C"

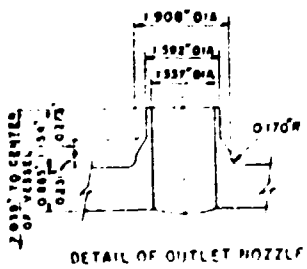

DETAIL OF OUTLET NOZZLE

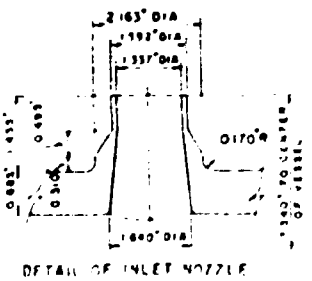

DETAIL OF INLET NOZZLE

Fig. 7.1. Dimensions for Stone and Hochschild photoelastic model.

estimated the experimental error to be about ±5% for the σ_t stresses and about 0 to −15% for the σ_η stresses.

Since the two nozzles are closely spaced in the transverse plane of the vessel, one might expect the interaction between them to affect the stresses in the transverse plane more than in the longitudinal plane. This appears to be the case since there is a greater difference between the stresses reported for the two nozzles in the transverse plane than in the longitudinal plane. Unfortunately, Stone and Hochschild did not test an isolated nozzle of either type, so it is not possible to determine whether the stresses are influenced more by the interaction between the nozzles or by the differences in their geometric detail. Nevertheless, the experimental values reported for both planes are sufficiently close to justify modeling the structure with two identical nozzles.

In addition to maximum values for both nozzles, Stone and Hochschild gave experimental stress distribution curves for nozzle 23 in the longitudinal plane (180°) of the vessel for both the inside and outside surfaces of the model. No other data were reported for the inlet nozzle, No. 24. The finite-element model and analyses discussed below are for a nozzle-vessel structure with two identical nozzles like the outlet nozzle 23 which we will designate as model SH-23DD.

7.1 Finite-Element Model

The finite-element model consisted of the one-eighth symmetry section shown in Figs. 7.2 to 7.4. The centerline of the nozzle is located 13.2° (half the nozzle spacing) from the global z coordinate direction, so that the model represents two identical nozzles spaced 26.4° apart in a transverse plane of the vessel. The model had 1894 nodes and 578 solid isoparametric elements, each having from 8 to 16 nodes. All nodes in the symmetry planes were constrained to remain in those planes. One element through the wall thickness was used for most of the vessel and the nozzle extension; four elements were used through the thickness in the intersection region. The same type of coordinate system and element and node numbering scheme was used for this model as for the previous models.

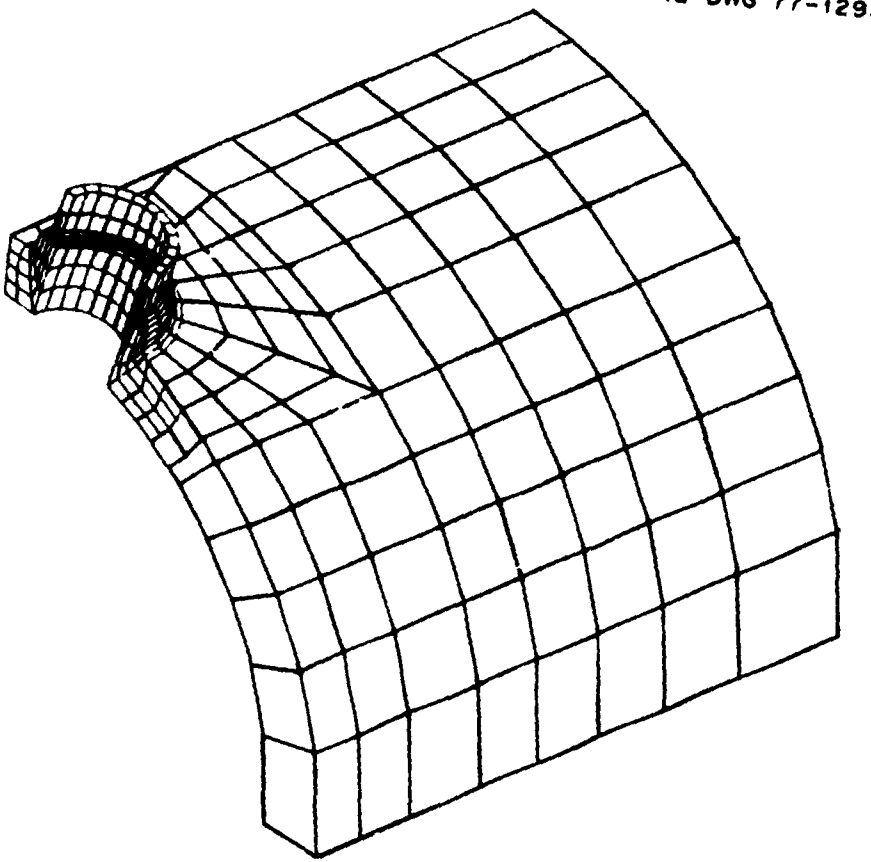

Fig. 7.2. Isometric view of the finite-element model for SH-23DD.

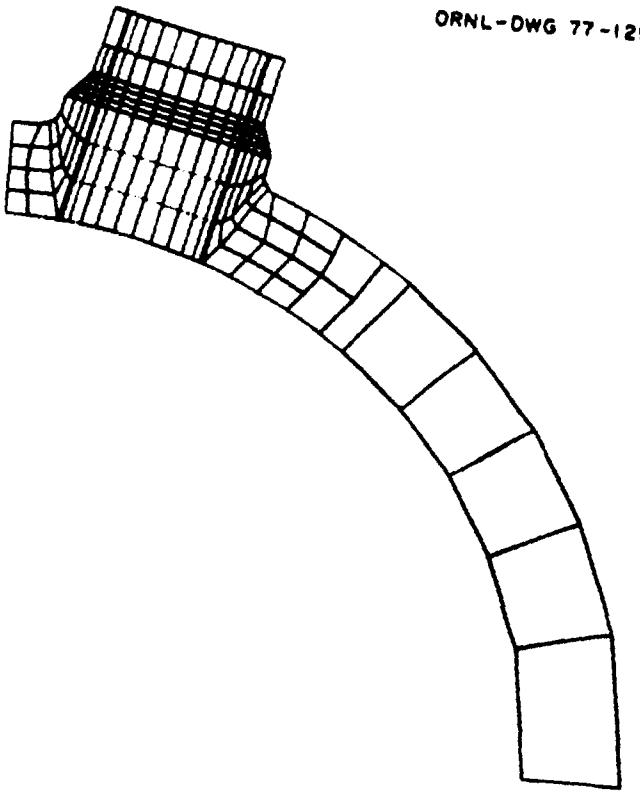

Fig. 7.3. End view of the finite-element model for SH-23DD.

ORNL-DWG-77-12929

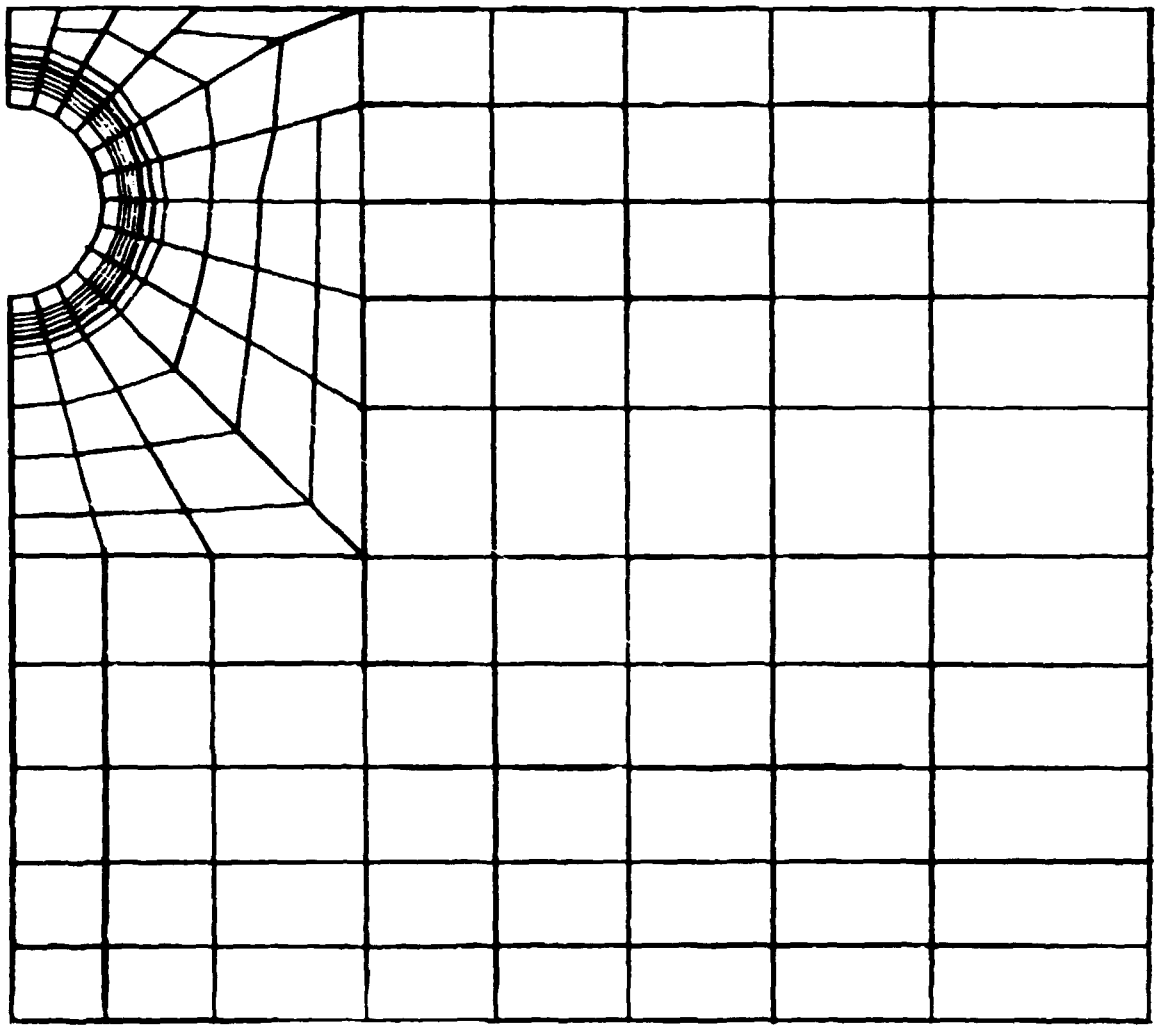

Fig. 7.4. Top view, along the z' axis, of the finite-element model SH-23DD.

Figures 7.5 and 7.6 illustrate the numbering sequence for the nodes and elements respectively. The nodal sequences for the elements in the nozzle and vessel regions are illustrated in Fig. 7.7.

7.2 Stress Analysis

This model was analyzed using 1.0 psi internal pressure for easy comparison with the photoelastic data. As with the other models, the

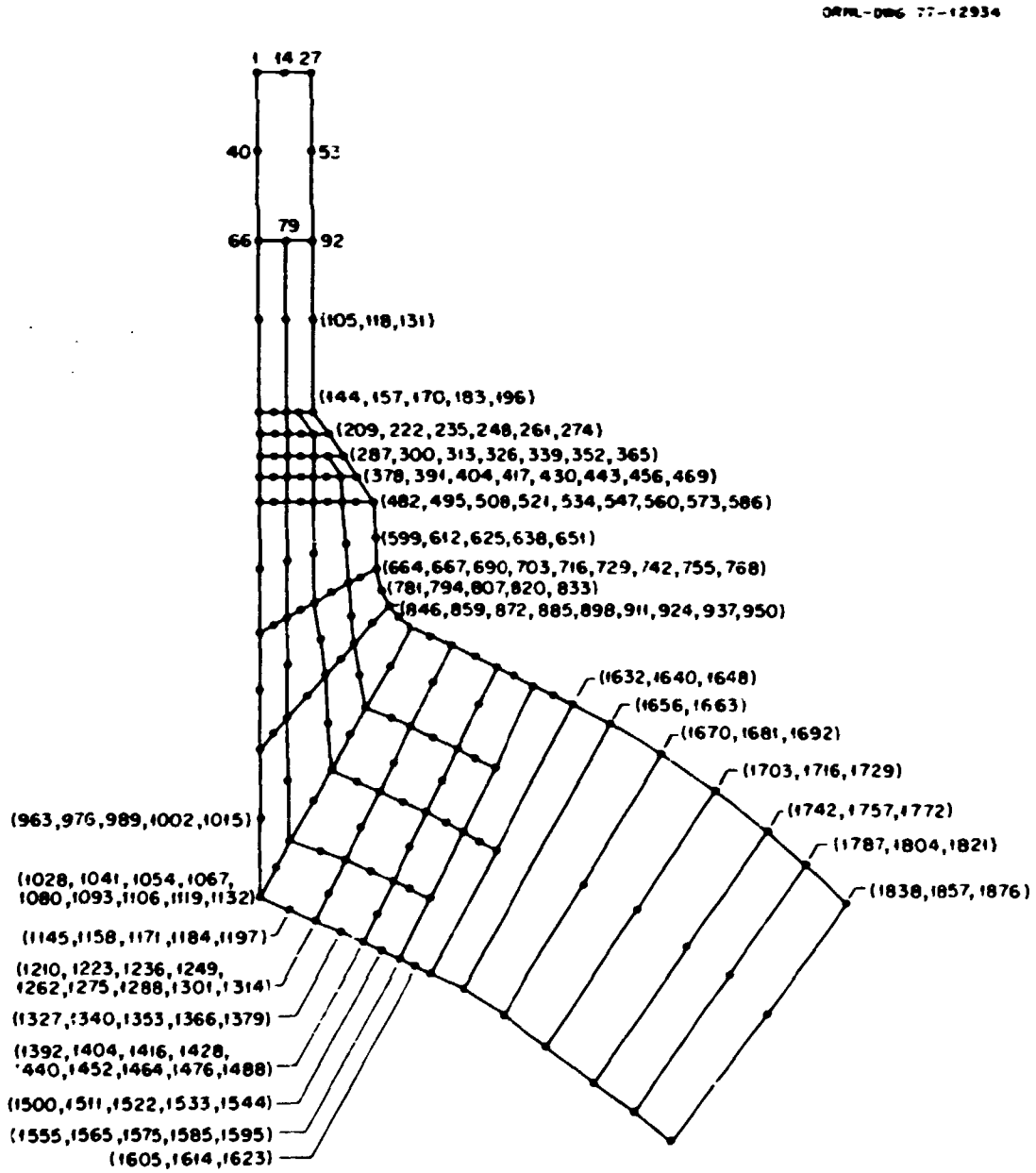

Fig. 7.5. Numbering of nodes in the transverse plane (90°) for model SH-23DD.

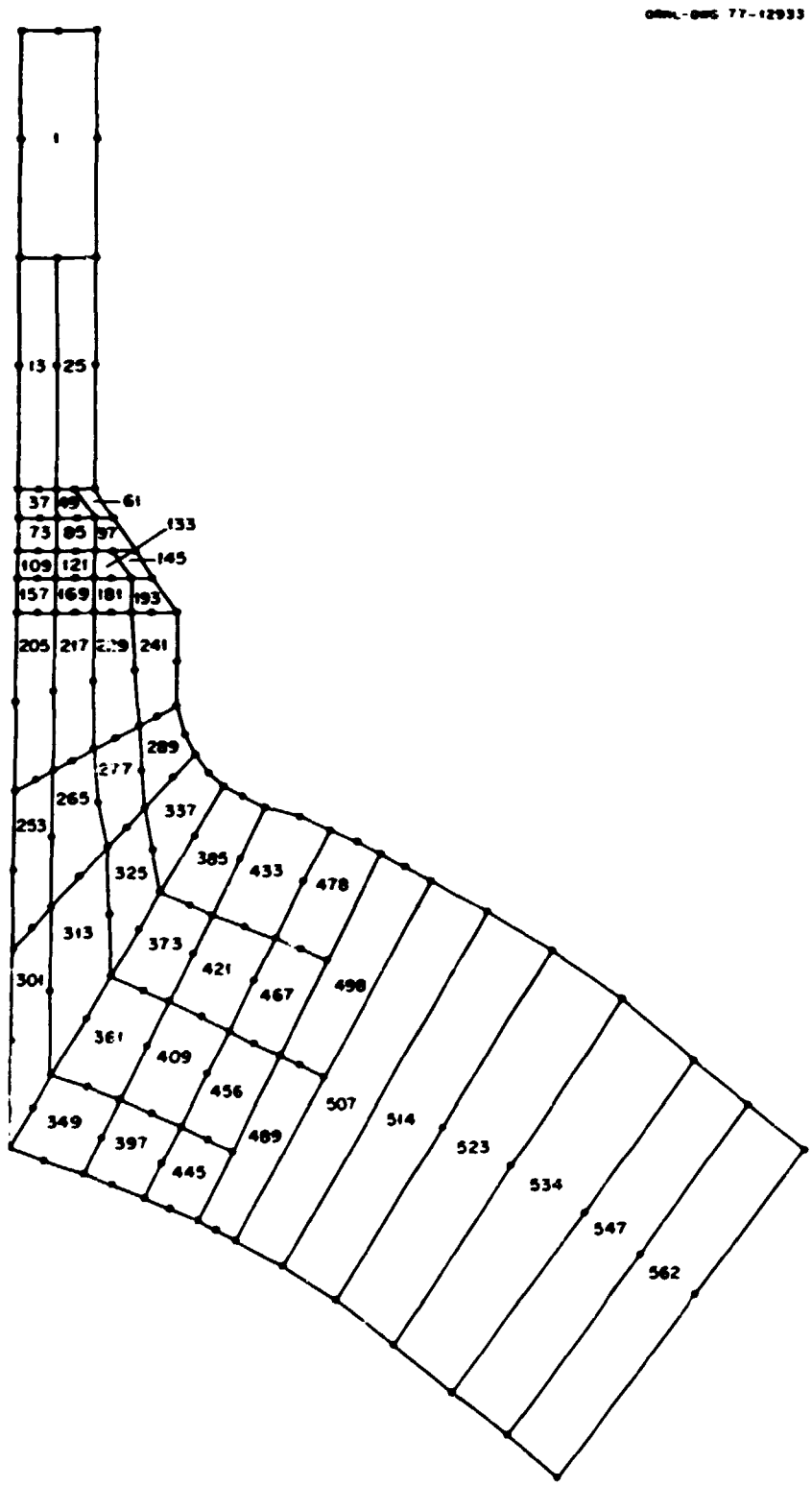

Fig. 7.6. Numbering of elements in the transverse plane (90°) for model SH-23DD.

ORNL-DWG 77-2635

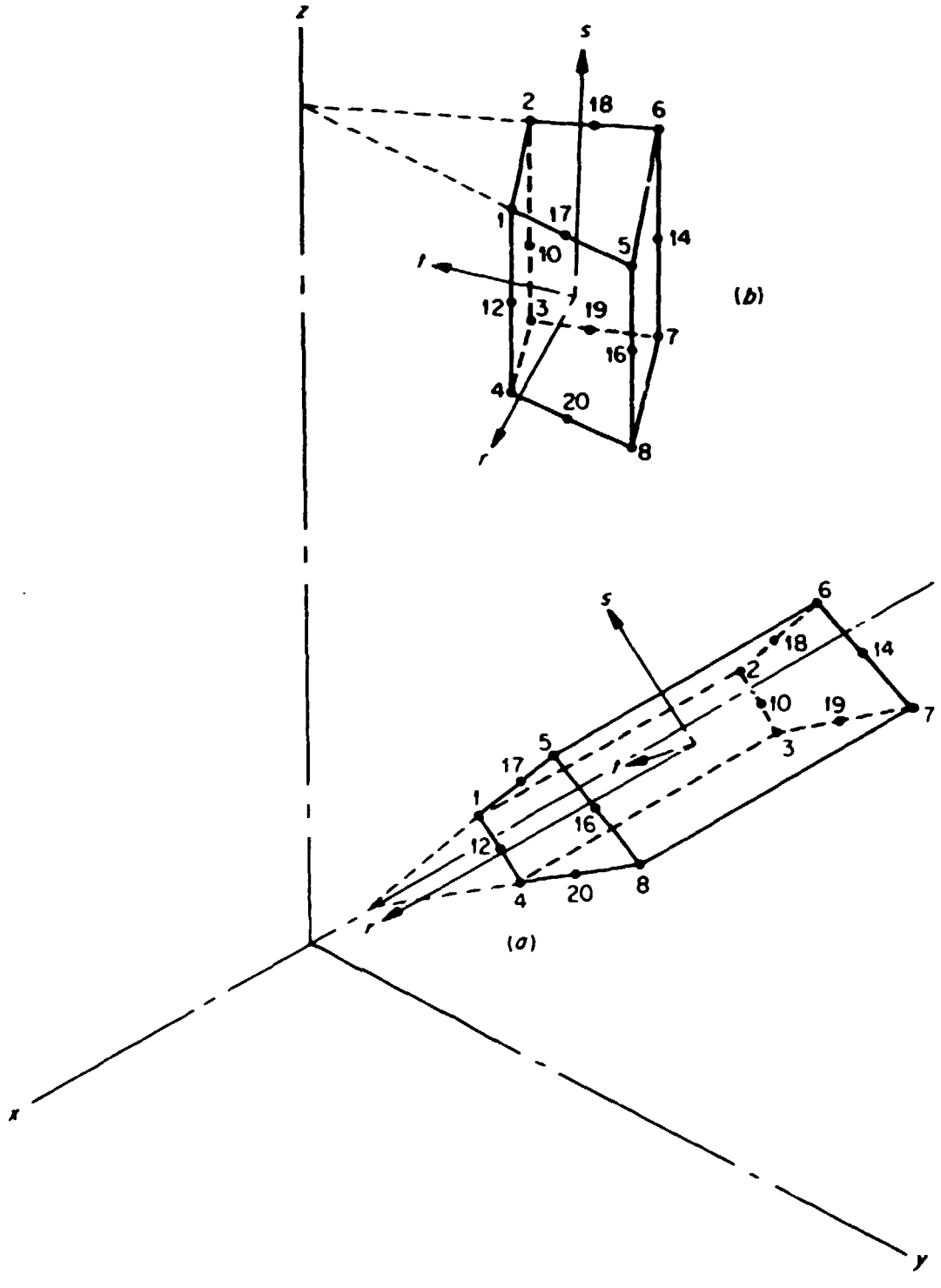

Fig. 7.7. Nodal sequence for elements (model SH-23DD): (*a*) elements in vessel zone; (*b*) elements in nozzle zone.

pressure caps on the ends of the run and nozzle were simulated by equivalent force loads on the open ends of the model. Isotropic material property values for Young's modulus and Poisson's ratio were set equal to E = 7500 and ν = 0.3, respectively. The influence of different values for ν was not investigated for this model because of experience with the previous models. Calculations for this model were made using the 2×2×2 integration rules.

7.3 Results

Summary comparisons between the finite-element results and the photoelastic data reported by Stone and Hochschild for nozzle 23 are given in Table 7.2 and Fig. 7.8. Tabulated values from the finite-element analysis are given in the appendix. Maximum principal stresses for both the longitudinal (180°) and transverse (90°) plane are listed in Table 7.2 with the differences at each point expressed as a percentage of the experimental values. Principal stress distributions for the inside and outside surfaces in the longitudinal plane are shown in Fig. 7.8.

Table 7.2. Comparison between experimental and finite-elements results[a] for SH-23DD

	Longitudinal plane (180°)				Transverse plane (90°)			
	Inside surface		Outside surface		Inside surface		Outside surface	
	σ_n/P	σ_t/P	σ_n/P	σ_t/P	σ_n/P	σ_t/P	σ_n/P	σ_t/P
Photoelastic data	17.9	−1.0	9.6	6.2	4.4	−4.2	10.6	8.6
Finite-element results	16.5	−1.09	6.7	4.2	5.2	−4.8	8.7	6.9
Percentage difference	7.8	9.0	30.2	32.3	18.2	14.3	17.9	19.8

[a]For nomenclature refer to Table 7.1.

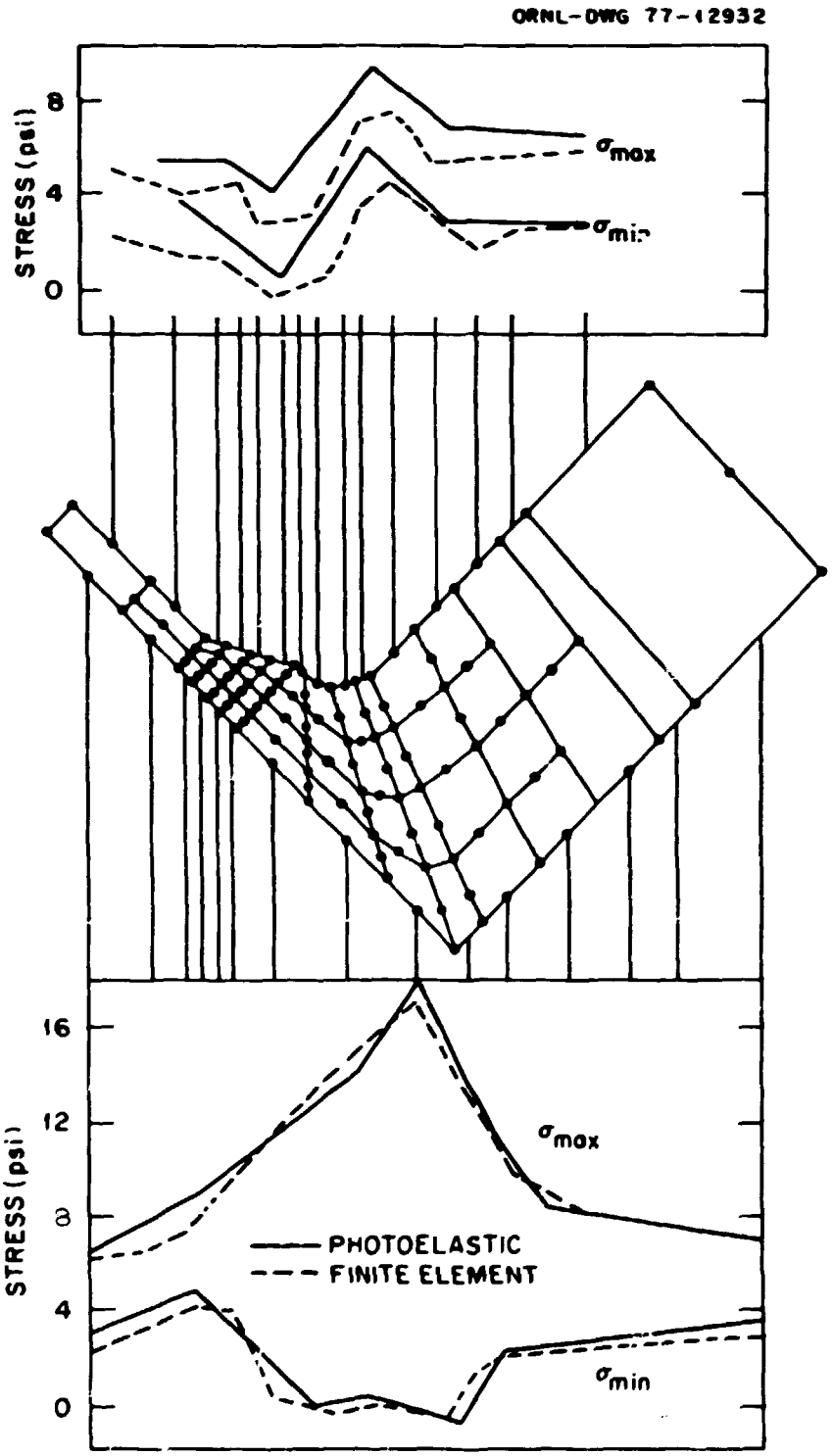

Fig. 7.8. Principal stress distributions for model SH-23DD at 180° section, internal pressure load = 1.0 psi.

In general, the finite-element results agree very well with the experimental data, especially for the inside surface in the longitudinal plane. The maximum calculated principal stress value, which occurred on the inside surface at the nozzle corner, differed from the experimental value by less than 8%. Larger differences, however, occurred for other positions — from about 15 to 20% for the transverse plane to about 30% for the outside surface in the longitudinal plane.

8. SUMMARY AND DISCUSSION

This report describes the development and validation of a three-dimensional finite-element computer program, MULT-NOZZLE, for analyzing cylindrical pressure vessels with closely spaced nozzles under internal pressure and external force and moment loadings. This first volume documents the analysis of pressure vessels with two identical nozzles for internal pressure loading. Volumes 2 and 3 (to be published) discuss external force and moment loadings on the nozzles and the analysis of pressure vessels with three closely spaced nozzles, respectively. A user's manual will be published as Volume 4.

MULT-NOZZLE consists of two subprograms which may be operated independently: an automatic mesh generator, FEMG, adapted from an earlier code written by Krishnamurthy;[6] and SAP3M, which is a modified and improved version of the SAP3 finite-element code written earlier by Wilson.[7] Output from MULT-NOZZLE is both printed and stored on tape for post-processing.

The major improvements to SAP3 include the addition of a variable 8- to 21-node isoparametric brick element, incorporation of a more efficient matrix equation solver, and implementation of an accurate local stress-smoothing algorithm for calculating element surface stresses. The variable-node element makes it possible to construct finite-element mesh layouts with variable densities to accommodate regions of higher and lower stress gradients using a minimum number of elements. The improved matrix equation solver, developed by Mondkar and Powell,[12] significantly reduces the computational time and cost required to solve the large sets of equations resulting from the finite-element idealization of vessel-nozzle structures. The local stress-smoothing technique, proposed earlier by Hinton and Campbell,[8] is an effective bilinear extrapolation procedure for improving the accuracy of the stresses calculated at the element surfaces and for decreasing the numerical sensitivity to Poisson's ratio.

The development and validation of the computer program for internal pressure loading discussed in this volume includes analyses for two classical elasticity problems and for three two-nozzle photoelastic pressure

vessel models. The relative influence of Poisson's ratio, finite-element distortion, numerical integration order, and element density or mesh size on the solution accuracy were investigated.

The two classical problems, a simply supported beam in plane-strain bending and a Lamé ring with internal pressure, were used primarily to validate the accuracy of the SAP3M module under the various options available for setting up the loading and boundary conditions. The effects of element distortion and different values for Poisson's ratio, which theoretically should not influence the solution, were also investigated and found to be negligible. Third-order (3×3×3) and reduced second-order (2×2×2) Gaussian quadrature numerical integration gave essentially the same results. All the finite-element results for these two problems agreed with the theoretical solutions to better than 2%, with most of the results within 1%.

The three two-nozzle pressure vessel models included two with the nozzles located in a longitudinal plane (WC-12DD and WC-100DD) and one with the two nozzles located in a transverse (circumferential) plane designated here as SH-23DD. Nominal dimensionless geometric parameters for the models are listed in Table 8.1. These models were studied to validate the entire MULT-NOZZLE program, including both the automated mesh

Table 8.1. Geometric parameters for MULT-NOZZLE validation models

Model	D_i/T[a]	d_i/t[b]	d_i/D_i[c]
WC-12DD	12.0	12.0	0.129
WC-100DD	100.0	100.0	0.110
SH-23DD	11.3		0.134

[a]Ratio of inner vessel diameter to vessel thickness.

[b]Ratio of inner nozzle diameter to nozzle thickness

[c]Ratio of inner nozzle diameter to vessel diameter.

generation module FEMG and the finite-element module SAP3M. Published experimental photoelastic data were used for judging the acceptability of the finite-element results.

In general, the finite-element results agreed very well with the experimental data, thus substantiating our claim for the validity of the computer program. The agreement between the experimental and analytical maximum values obtained using Poisson's ratio $\nu = 0.3$ are excellent, as summarized in Table 8.2. The best results were obtained for the relatively thick-walled model WC-12DD, for which MULT-NOZZLE gave exactly the same maximum value as the photoelastic data. Maximum calculated stress indices for the other two models, WC-100DD and SH-23DD, differed with the experimental values by about 8%, which is well within the 10% acceptance criterion.

Table 8.2. Maximum stress index comparison between photoelastic and finite-element results

Model	Experimental maximum σ_n/S[a]	Finite-element[b] maximum σ_n/S	Percentage error e[c]
WC-12DD	2.96	2.96	0%
WC-100DD	3.0	2.76	8.0%
SH-23DD	2.91	2.68	7.8%

[a] $S = \sigma_{nom} = p(D_i + T)/2T$.

[b] Determined using $\nu = 0.3$.

[c] $e = (E - F)/E$, where E is the experimental value and F is the finite-element value.

Analytical results obtained using Poisson's ratio other than 0.3 differed from the experimental data progressively as ν approached 0.5. These results are summarized in Table 8.3 along with the respective errors for the calculations. The discrepancies are consistent with previous experience[26,29-33] and reflect the difficulties encountered in using the classical finite-element displacement formulation to analyze structures of

Table 8.3. Maximum stress index comparisons for different values of Poisson's ratio ν

Model	Experimental maximum σ_n/S^a	Finite-element results (2×2×2) integration		
		ν = 0.3	ν = 0.4	ν = 0.485
WC-12DD	2.96	2.96, (0%)[b]		2.34 (21%)
WC-100DD	3.0	2.76 (7.8%)	2.67 (10.9%)	2.11 (29.7%)
SH-23DD	2.91	2.68 (8.0%)		

[a] $S = \sigma_{nom} = p(D_i + T)/2T$.

[b] Percentage error for the calculated values are given in parentheses.

nearly incompressible materials. This formulation, which is derived from the minimum potential energy principle, is known to yield results which can be greatly in error as Poisson's ratio approaches 0.5; and in the limiting case, ν = 0.5, the formulation is no longer valid. How close one may approach ν = 0.5 without encountering serious difficulty is apparently related to the size of the stiffness matrix (i.e., the number of elements in the analytical model) and the magnitude of the stress gradients. In the analyses for the classical beam and thick-walled ring problems, neither condition was severe and good results were obtained over a wide range of ν. In the analyses for the pressure vessel models, however, both the stress gradients at the intersection of the nozzle and vessel and the number of finite elements required to model the structure are relatively large and therefore the analysis is more sensitive to Poisson's ratio. We were able to decrease this sensitivity by adding the Gauss point stress extrapolation procedure discussed in Section 3.7; nevertheless, some prudence should be exercised in using values for Poisson's ratio much larger than 0.3. Fortunately, Bass et al.[29] have shown that using a value of Poisson's ratio equal to 0.3 with Gauss point stress extrapolation for

analyzing nozzles in cylindrical pressure vessels gives equally good results for both steel and photoelastic models. Further improvements would require reformulating the finite-element description as discussed by Malkus[31] and others[30,32,33] and the attendant reprogramming effort.

Detailed comparisons between the calculated and experimental stress distributions for the inside and outside surfaces in the longitudinal and transverse planes of the models showed that the finite-element results were generally in good agreement, although there were some areas for which the agreement was only fair. For the thinner-walled model WC-100DD, the results for the membrane region also appear to support Irons and Hellen's[27] contention that solid isoparametric elements may not be fully reliable for analyzing very thin shell structures. It thus appears that vessels with diameter-to-thickness ratios of about 100 represent a prudent upper limit for use of the finite-element formulation currently in MULT-NOZZLE.

The numerical integration order apparently had very little influence on the solution accuracy. For reasons of economy, we recommend using reduced 2×2×2 Gaussian quadrature in future studies.

The variable node isoparametric element installed in SAP3M appeared to perform satisfactorily, although some of the "raggedness" in the stress plots may have been caused by dropping nodes to accommodate the change in element density. Nevertheless, the advantage in being able to increase the element density in the high stress gradient region of the nozzle intersection appears to outweigh the disadvantages.

In summary, the results of the studies presented in this volume confirm the validity of the MULT-NOZZLE computer program for analyzing cylindrical pressure vessels with two closely spaced nozzles under internal pressure loading. Volumes 2 and 3 will discuss the use of the program for considering external loads applied to the nozzles and for three nozzle clusters, respectively. Complete user's instructions will be presented in Volume 4.

ACKNOWLEDGMENTS

The authors wish to express their gratitude to G. A. Greenbaum and N. E. Johnson of System Development Corporation for their encouragement and assistance in planning the development of MULT-NOZZLE; to L. S. Tong, C. Z. Serpan, and E. K. Lynn of the Nuclear Regulatory Commission for pointing out the need and providing the means for conducting the study; and to J. L. Mershon, E. C. Rodabaugh, and other members of the PVRC Subcommittee on Reinforced Openings and External Loadings for their keen interest and encouragement.

D. P. Mondkar and G. H. Powell at the University of California, Berkeley, wrote and incorporated the program subroutines for the variable 8 to 21 solid isoparametric finite element and for the solution to the structural stiffness equation; W. C. T. Stoddart, UCCND Engineering Division, and B. R. Bass, UCCND Computer Sciences Division, provided background material for the stress extrapolation procedure; P. G. Fowler, UCCND Computer Sciences Division, provided all the plotting routines for FEMG, and R. E. Textor, also of UCCND Computer Sciences Division, provided assistance in setting up the program to operate on the UCCND computer facility. Their help is gratefully acknowledged.

Finally, the authors gratefully acknowledge the efforts of F. M. O'Hara for the preliminary editing and Linda Dockery for typing the drafts and preparation of the manuscript. Final editing and processing were provided by the ETD Reports Office.

REFERENCES

1. *ASME Boiler and Pressure Vessel Code, Section III, Division I, Nuclear Power Plant Components*, American Society of Mechanical Engineers, New York, 1974.

2. J. L. Mershon and E. C. Rodabaugh, *Preliminary Evaluation of Closely Spaced Reinforced Openings in a Cylindrical Pressure Vessel Under Internal Pressure Loading*, ORNL/Sub/3131-10 (June 30, 1975).

3. F. K. W. Tso, R. A. Weed, and J. W. Bryson, *Stress Analysis of Cylindrical Pressure Vessels with Closely Spaced Nozzles by the Finite-Element Method, Vol. 2. Stress Analysis of Vessels with Two Closely Spaced Nozzles Loaded with External Forces and Moments*, ORNL/NUREG-18/V2 (to be published).

4. F. K. W. Tso, R. A. Weed, and J. W. Bryson, *Stress Analysis of Cylindrical Pressure Vessels with Closely Spaced Nozzles by the Finite-Element Method, Vol. 3. Stress Analysis of Vessels with Three Closely Spaced Nozzles Under Internal Pressure*, ORNL/NUREG-18/V3 (to be published).

5. F. K. W. Tso and R. A. Weed, *Stress Analysis of Cylindrical Pressure Vessels with Closely Spaced Nozzles by the Finite-Element Method, Vol. 4. User's Instructions for the Computer Program MULT-NOZZLE*, ORNL/NUREG-18/V4 (to be published).

6. N. Krishnamurthy, *Three-Dimensional Finite-Element Analysis of Thick-Walled Vessel-Nozzle Junctions with Curved Transitions*, ORNL-TM-3315 (Mar. 24, 1971).

7. E. L. Wilson, *Finite-Element Analysis of Mine Structures*, Final Report to Denver Mining Res. Ctr., U.S. Dept. Interior, Bureau of Mines, Contract No. H0110231, Dept. of Civil Engineering, University of California, Berkeley (September 1972).

8. E. Hinton and J. S. Campbell, "Local and Global Smoothing of Discontinuous Finite Element Functions Using a Least Squares Method," *Int. J. Num. Meth. Eng.* 8, 461-80 (1974).

9. I. Ergatoudis, B. M. Irons, and O. C. Zienkiewicz, "Curved Isoparametric Quadrilateral Elements for Finite Element Analysis," *Int. J. Solids Struct.* 4, 31-42 (1968).

10. D. P. Mondkar and G. H. Powell, *Static and Dynamic Analysis of Nonlinear Structures*, EERC 75-10, University of California, Berkeley (March 1975).

11. D. P. Mondkar and G. H. Powell, "Towards Optimal In-Core Equation Solving," *Comput. Struct.* 4, 531-48 (1974).

12. D. P. Mondkar and G. H. Powell, "Large Capacity Equation Solver for Structural Analysis," *Comput. Struct.* 4, 699-728 (1974).

13. E. Volterra and J. H. Gaines, *Advanced Strength of Materials*, Prentice-Hall, Englewood Clifts, N.J., 1971, pp. 76-9.

14. E. Volterra and J. H. Gaines, *Advanced Strength of Materials*, Prentice-Hall, Englewood Clifts, N.J., 1971, pp. 145-9.

15. M. M. Leven, *Stress Distribution at Two Closely Spaced Reinforced Openings in a Pressurized Cylinder*, 71-9E7-PHOTO-R1, Westinghouse Research Lab. (Apr. 9, 1971).

16. R. M. Stone and S. Hochschild, "The Effect of Nozzle Spacing on the Pressure Stresses at the Intersection of Cylindrical Nozzles and Shells," *Trans. ASME* 89, Ser. A, 360-68 (July 1967).

17. R. W. Clough, "Comparison of Three Dimensional Finite Elements," *Proc. Symp. Appl. Finite-Element Method in Civil Eng.*, Vanderbilt University, Nashville, Tenn., 1969.

18. E. Hinton and B. M. Irons, "Least Squares Smoothing of Experimental Data Using Finite Elements," *J. Br. Soc. Strain Meas.* 4, 24-27 (1968).

19. J. T. Oden, *Finite Elements of Nonlinear Continua*, McGraw-Hill, New York, 1971.

20. J. T. Oden and H. J. Branchli, "On the Calculation of Consistent Stress Distributions in Finite Element Applications," *Int. J. Num. Meth. Eng.* 4, 317-25 (1971).

21. J. T. Oden and J. N. Reddy, "Note on an Approximate Method for Computing Consistent Conjugate Stresses in Elastic Finite Elements," *Int. J. Num. Meth. Eng.* 6, 55-61 (1973).

22. D. Naylor, "Stresses in Nearly Incompressible Materials by Finite Elements with Application to the Calculation of Excess Pore Pressures," *Int. J. Num. Meth. Eng.* 8, 443-60 (1974).

23. L. R. Hermann, "Interpretation of Finite Element Procedure as Stress Error Minimization Procedure," *J. Eng. Mech. Div. ASCE* 98, 1330-35 (1972).

24. J. Barlow, "Optimal Stress Locations in Finite Element Models," *Int. J. Num. Meth. Eng.* 10, 243-51 (1976).

25. M. M. Leven, "Epoxy Resins for Photoelastic Use," *Epoxy Resins for Photoelastic Use, Symposium on Photoelasticity*, ed. by M. M. Frocht, Pergamon, Elmsford, N.Y., 1963.

26. I. Fried, "Influence of Poisson's Ratio on the Conditions of the Finite Element Stiffness Matrix," *Int. J. Solids Structures* 9, 323-29 (1973).

27. B. M. Irons and T. K. Hellen, "On Reduced Integration in Solid Isoparametric Elements When Used in Shells with Membrane Modes," *Int. J. Num. Meth. Eng.* 10, 1179-82 (1976).

28. O. C. Zienkiewicz, *The Finite Element Method in Engineering Science*, McGraw-Hill, New York, 1972.

29. B. R. Bass, J. W. Bryson, and S. E. Moore, "Validation of the Finite Element Stress Analysis Computer Program CORTES-SA for Analyzing Piping Tees and Pressure Vessel Nozzles," in *Pressure Vessels and Piping: Computer Program Evaluation and Qualification*, presented at the Joint Energy Technology Conference and Exhibition, Houston, Tex., Sept. 18-22, 1977.

30. L. R. Hermann, "Elasticity Equations for Incompressible and Nearly Incompressible Materials by a Variational Theorem," *AIAA J.* 3(10), 1896-1900 (1965).

31. D. S. Malkus, "A Finite Element Displacement Model Valid for Any Value of the Compressibility," *Int. J. Solids Struct.* 12, 731-38 (1976).

32. J. R. Booker and J. C. Small, "The Economical Solution of Elastic Problems for a Range of Poisson's Ratio," *Int. J. Num. Meth. Eng.* 9, 847-53 (1975).

33. R. L. Taylor, K. S. Pister, and L. R. Hermann, "On a Variational Theorem for Incompressible and Nearly-Incompressible Orthotropic Elasticity," *Int. J. Solids Structures* 4, 875-83 (1968).

Appendix

MULT-NOZZLE STRESS ANALYSIS DATA FOR THE WC-12DD, WC-100DD, AND SH-23DD MODELS

Tables A.1 to A.14 present stress distributions calculated for the three models with MULT-NOZZLE for differing values of Poisson's ratio and orders of Gauss integration. These tables can be used in conjunction with the element-number drawings to quantify the values shown in the stress-distribution figures of the text.

BLANK PAGE

Table A.1. Hoop stress on WC-12DD on inside surface at 0° section and stress location 12 (internal pressure load = 0.151 psi)

Element No.	Stress (psi)		
	$\nu = 0.3$	$\nu = 0.485$	
	3 × 3 × 3 Gauss rule	2 × 2 × 2 Gauss rule	3 × 3 × 3 Gauss rule
1	0.9519	0.9353	0.9522
13	0.9233	0.9386	0.9392
25	0.6991	0.7429	0.6264
49	0.5948	0.6503	0.6257
73	0.5025	0.5690	0.5728
109	0.4609	0.5059	0.6395
145	0.4810	0.5215	0.5242
193	0.5558	0.5762	0.5747
241	0.8627	0.8303	0.8568
289	1.5849	1.446[illegible]	1.4196
337	2.4164	1.9762	1.9499
385	2.8134	2.2661	2.2845
433	2.4491	2.0830	2.0884
481	1.8267	1.7328	1.7497
529	1.4642	1.3839	1.4182
577	1.2911	1.2146	1.3088
621	1.1828	1.0421	1.1872
639	1.1324	1.1156	1.1112
646	1.0656	1.0835	1.0788
656	0.9607	0.8519	0.8425
668	0.9073	0.8519	0.8404

Table A.2. Hoop stress on WC-12DD on outside surface at 0° section and stress location 16 (internal pressure load = 0.151 psi)

Element No.	Stress (psi)		
	ν = 0.3	ν = 0.485	
	3 × 3 × 3 Gauss rule	2 × 2 × 2 Gauss rule	3 × 3 × 3 Gauss rule
1	0.8251	0.8462	0.8344
13	0.8625	0.8740	0.8560
37	0.7044	0.6782	0.8291
61	0.4028	0.1699	0.2289
97	0.2147	−0.1759	−0.1598
133	0.1126	−0.1099	−0.1155
181	0.0265	−0.2441	−0.2612
229	−0.0076	−0.1309	−0.1446
277	0.0011	0.0070	−0.0012
325	0.0424	0.0582	0.0380
373	0.1392	0.1109	0.1173
421	0.3257	0.3169	0.3437
469	0.5801	0.6860	0.6828
517	0.7720	0.9639	0.9208
565	0.8214	0.9957	0.9819
610	0.7886	0.6733	0.7417
630	0.7737	0.5427	0.6908
639	0.7756	0.7191	0.6798
646	0.7674	0.6270	0.6333
656	0.7800	0.7566	0.7620
668	0.7427	0.7592	0.7665

Table A.3. Hoop stress on WC-12DD on inside surface at 180° section and stress location 10 (internal pressure load = 0.151 psi)

Element No.	Stress (psi)		
	$\nu = 0.3$	$\nu = 0.485$	
	3 × 3 × 3 Gauss rule	2 × 2 × 2 Gauss rule	3 × 3 × 3 Gauss rule
12	0.9519	0.9351	0.9522
24	0.9229	0.9388	0.9388
36	0.6960	0.7412	0.6252
60	0.5901	0.6490	0.6244
84	0.4960	0.5680	0.5718
120	0.4526	0.5060	0.5143
156	0.4708	0.5229	0.5251
204	0.5436	0.5794	0.5774
252	0.8474	0.8424	0.8682
300	1.5830	1.4656	1.4380
348	2.4909	2.0468	2.0070
396	2.9582	2.3408	2.3757
444	2.6042	2.2363	2.2080
492	2.1003	1.9677	1.9831
540	1.7436	1.7012	1.6926
587	1.3331	0.2101	0.3685

Table A.4. Hoop stress on WC-12DD on outside surface at 180° section and stress location 14 (internal pressure load = 0.151 psi)

Element No.	Stress (psi)		
	$\nu = 0.3$	$\nu = 0.485$	
	3 × 3 × 3 Gauss rule	2 × 2 × 2 Gauss rule	3 × 3 × 3 Gauss rule
12	0.8251	0.8462	0.8345
24	0.8626	0.8741	0.8560
48	0.7047	0.6810	0.8314
72	0.4029	0.1698	0.2290
108	0.2146	−0.1768	−0.1604
144	0.1125	−0.1115	−0.1168
192	0.0268	−0.2467	−0.2636
240	−0.0058	−0.1313	−0.1454
288	0.0050	0.0121	0.0064
336	0.0492	0.0704	0.0496
384	0.1459	0.1361	0.1467
432	0.3162	0.3421	0.3550
480	0.5561	0.6701	0.6769
528	0.7911	1.0692	1.0372
576	0.9272	1.2921	1.1754

Table A.5. Stresses on inside surface of WC-12DD at 90° section (internal pressure load = 0.151 psi)

Element No.	Stress location	Stress (psi)					
		ν = 0.3		ν = 0.485			
		3 × 3 × 3 Gauss rule		2 × 2 × 2 Gauss rule		3 × 3 × 3 Gauss rule	
		σ_x[a]	$\bar{\sigma}_x$[b]	σ_x	$\bar{\sigma}_x$	σ_x	$\bar{\sigma}_x$
18	10	1.0249	1.0250	1.0068	1.0076	1.0204	1.0211
19	12	1.0251		1.0083		1.0218	
30	10	0.8160	0.8166	0.8762	0.8893	0.8015	0.8041
31	12	0.8170		0.9024		0.8065	
54	10	0.6662	0.6671	0.6603	0.6642	0.6388	0.6423
55	12	0.6679		0.6681		0.6457	
78	10	0.5080	0.5001	0.5236	0.5283	0.5253	0.5299
79	12	0.4920		0.5330		0.5343	
114	10	0.3726	0.3745	0.3976	0.4031	0.3986	0.4043
115	12	0.3762		0.4086		0.4099	
150	10	0.2710	0.2736	0.3259	0.3322	0.3212	0.3282
151	12	0.2760		0.3383		0.3350	
198	10	0.1969	0.2004	0.2725	0.2792	0.2592	0.2677
199	12	0.2037		0.2859		0.2761	
246	10	0.1592	0.1644	0.2883	0.2935	0.3273	0.3366
247	12	0.1695		0.2987		0.3458	
294	10	0.1998	0.2043	0.4023	0.3832	0.3426	0.3355
295	12	0.2088		0.3640		0.3283	
342	10	0.3225	0.3170	0.7219	0.6327	0.6852	0.6208
343	12	0.3115		0.5433		0.5513	
390	10	0.4777	0.4672	0.9494	0.8485	0.9759	0.8973
391	12	0.4566		0.7475		0.8187	
438	10	0.5380	0.5347	0.7279	0.7173	0.7470	0.7390
439	12	0.5314		0.7067		0.7309	
486	10	0.5267	0.5226	0.4732	0.3942	0.4924	0.4084
487	12	0.5184		0.3150		0.3243	
534	10	0.4622	0.4450	0.3774	0.1366	0.3799	0.1443
535	12	0.4277		-0.1043		-0.0912	
582	10	0.3365	0.2976	-0.1473	-0.4074	0.1642	-0.0240
583	12	0.2586		-0.6673		-0.2083	
626	10	0.3191	0.3194	-0.2134	-0.1233	0.1203	0.1564
627	12	0.3197		-0.0332		0.1925	
644	10	0.3770	0.3755	0.1760	0.1871	0.2341	0.2594
645	12	0.3739		0.1980		0.2846	
651	10	0.3724	0.4022	-0.0137	0.3755	0.0313	0.3713
652	12	0.4320		0.7647		0.7112	

[a] Stress parallels the axis of the vessel.

[b] Average value.

Table A.6. Stresses on outside surface of WC-1200 at 90° section (internal pressure load = 0.151 psi)

Element No.	Stress location	Stress (psi)					
		ν = 0.3		ν = 0.485			
		3 × 3 × 3 Gauss rule		2 × 2 × 2 Gauss rule		3 × 3 × 3 Gauss rule	
		σ_x[a]	$\bar{\sigma}_x$[b]	σ_x	$\bar{\sigma}_x$	σ_x	$\bar{\sigma}_x$
18	14	0.8034	0.8034	0.8019	0.8013	0.7771	0.7766
19	16	0.8033		0.8007		0.7760	
42	14	0.6564	0.6562	0.3546	0.3533	0.4722	0.4707
43	16	0.6558		0.3518		0.4690	
66	14	0.4282	0.4278	0.1625	0.1610	0.2054	0.2038
67	16	0.4273		0.1593		0.2021	
102	14	0.2954	0.2948	−0.0505	−0.0519	−0.0381	−0.0398
103	16	0.2941		−0.0533		−0 0413	
138	14	0.2428	0.2422	0.0262	0.0255	0.0216	0.0206
139	16	0.2415		0.0246		0.0195	
186	14	0.2165	0.2158	0.0294	0.0303	0.0177	0.0181
187	16	0.2150		0.0311		0.0184	
234	14	0.2302	0.2296	0.0639	0.0667	0.0527	0.0551
235	16	0.2289		0.0695		0.0574	
282	14	0.2540	0.2538	0.1806	0.1882	0.1579	0.1648
283	16	0.2536		0.1958		0.1715	
330	14	0.3418	0.3426	0.2365	0.2510	0.2539	0.2672
331	16	0.3434		0.2654		0.2804	
378	14	0.4859	0.4914	0.4070	0.4177	0.4656	0.4762
379	16	0.4969		0.4284		0.4866	
426	14	0.6232	0.6199	0.5692	0.5681	0.5668	0.5700
427	16	0.6164		0.5668		0.5731	
474	14	0.7370	0.7308	0.7108	0.6994	0.6463	0.6436
475	16	0.7245		0.6879		0.6408	
522	14	0.7510	0.7431	0.6817	0.6606	0.6598	0.6465
523	16	0.7351		0.6394		0.6330	
570	14	0.6657	0.6567	0.4437	0.4285	0.5477	0.5229
571	16	0.6477		0.4131		0.4979	
615	14	0.5105	0.4875	−0.0490	−0.1116	0.4213	0.3925
616	16	0.4644		−0.1741		0.3635	
635	14	0.5258	0.5313	0.1113	0.2204	0.4040	0.4520
636	16	0.5367		0.3294		0.4999	
644	14	0.5321	0.5275	0.4145	0.4049	0.3936	0.4027
645	16	0.5227		0.3952		0.4118	
651	14	0.4841	0.4931	0.7177	0.5842	0.7766	0.5745
652	16	0.5020		0.4510		0.3722	

[a] Stress parallels the axis of the vessel.

[b] Average value.

Table A.7. Hoop stress on WC-100DD on inside surface at 0° section, stress location 12
(internal pressure load = 0.0195 psi)

Element No.	Stress (psi)				
	ν = 0.3		ν = 0.4	ν = 0.485	
	2 × 2 × 2 Gauss rule	3 × 3 × 3 Gauss rule	2 × 2 × 2 Gauss rule	2 × 2 × 2 Gauss rule	3 × 3 × 3 Gauss rule
1	0.8465	0.8501	0.8620	0.7557	0.6412
11	0.7089	0.6777	0.6491	0.1966	0.3791
21	0.1171	0.1584	0.1419	0.4026	0.3039
31	0.0367	0.0681	0.0834	0.3098	0.3556
51	0.1279	0.1496	0.1752	0.2716	0.3181
71	0.3982	0.4146	0.4650	0.5456	0.5563
91	0.8355	0.8462	0.9130	0.8629	0.8882
111	1.4081	1.4091	1.4628	1.3092	1.3162
131	2.0621	2.0462	2.0335	1.6540	1.5836
151	2.4192	2.4007	2.3486	1.8966	1.8629
171	1.9957	1.9833	1.9799	1.7852	1.7457
191	1.5249	1.5275	1.5269	1.3637	1.4089
211	1.3475	1.3563	1.3807	1.3292	1.3619
229	1.2245	1.2566	1.2440	1.1834	1.1576
236	1.1306	1.1372	1.1468	1.1047	1.1112

Table A.8. Hoop stress on WC-100DD on outside surface at 0° section, stress location 16
(internal pressure load = 0.0195 psi)

Element No.	Stress (psi)				
	ν = 0.3		ν = 0.4	ν = 0.485	
	2 × 2 × 2 Gauss rule	3 × 3 × 3 Gauss rule	2 × 2 × 2 Gauss rule	2 × 2 × 2 Gauss rule	3 × 3 × 3 Gauss rule
1	0.9037	0.9406	0.9293	1.2145	1.3253
11	0.8567	0.7900	0.9338	1.3701	1.2092
21	0.1193	0.1319	0.1068	−0.0378	−0.0696
41	−0.1145	−0.1137	−0.2240	−0.7065	−0.8027
61	−0.1372	−0.1396	−0.2133	−0.5010	−0.5244
81	−0.1089	−0.1149	−0.1639	−0.2192	−0.2212
101	−0.0126	−0.0176	−0.0794	−0.0891	−0.0936
121	0.2030	0.1965	0.1231	0.0896	0.1084
141	0.5450	0.5526	0.4696	0.4463	0.5338
161	0.9505	0.9410	0.9343	1.0648	1.0448
181	1.2388	1.2254	1.2798	1.6085	1.5682
201	1.2003	1.1931	1.2216	1.5033	1.4300
220	1.0694	1.0588	1.0627	1.1397	1.0970
229	1.0139	1.0185	1.0196	1.1041	1.1202
236	0.9792	0.9793	0.9887	1.0775	1.0807

Table A.9. Hoop stress on WC-100DD on inside surface at 180° section, stress location 10 (internal pressure load = 0.0195 psi)

Element No.	Stress (psi)				
	$\nu = 0.3$		$\nu = 0.4$	$\nu = 0.485$	
	2 × 2 × 2 Gauss rule	3 × 3 × 3 Gauss rule	2 × 2 × 2 Gauss rule	2 × 2 × 2 Gauss rule	3 × 3 × 3 Gauss rule
10	0.8392	0.8414	0.8553	0.7478	0.6296
20	0.6828	0.6458	0.6193	0.1435	0.3152
30	0.0637	0.1016	0.0921	0.3889	0.2715
40	0.0070	0.0196	0.0455	0.3217	0.3691
60	0.1080	0.1243	0.1642	0.3034	0.3550
80	0.4166	0.4275	0.4952	0.6112	0.6249
100	0.9022	0.9068	0.9902	0.9527	0.9764
120	1.5291	1.5261	1.5780	1.3951	1.3842
140	2.3089	2.2929	2.2569	1.7309	1.6590
160	2.7654	2.7589	2.6729	2.1006	2.1189
180	2.5169	2.4983	2.4525	2.0312	1.9616
200	2.1359	2.1189	2.0499	1.2904	1.2188

Table A.10. Hoop stress on WC-100DD on outside surface at 180° section, stress location 14 (internal pressure load = 0.0195 psi)

Element No.	Stress (psi)				
	$\nu = 0.3$		$\nu = 0.4$	$\nu = 0.485$	
	2 × 2 × 2 Gauss rule	3 × 3 × 3 Gauss rule	2 × 2 × 2 Gauss rule	2 × 2 × 2 Gauss rule	3 × 3 × 3 Gauss rule
10	0.8933	0.9356	0.9254	1.2269	1.3411
20	0.8433	0.7720	0.9293	1.4193	1.2754
30	0.0789	0.0907	0.0706	−0.0468	−0.0723
50	−0.1469	−0.1461	−0.2573	−0.7209	−0.8140
70	−0.1499	−0.1509	−0.2309	−0.5321	−0.5549
90	−0.0984	−0.1018	−0.1583	−0.2196	−0.2166
110	0.0372	0.0362	−0.0314	−0.0418	−0.0332
130	0.3243	0.3255	0.2477	0.2156	0.2529
150	0.7540	0.7751	0.6959	0.6719	0.7739
170	1.2507	1.2496	1.2621	1.3238	1.2819
190	1.7081	1.7097	1.8024	2.1265	2.1571
210	2.0486	2.0531	2.3174	3.4395	3.3098

Table A.11. Stresses on WC-100DD on inside surface at 90° section (internal pressure load = 0.0195 psi)

Element No.	Stress location	Stress (psi)									
		ν = 0.3				ν = 0.4		ν = .485			
		2 × 2 × 2 Gauss rule		3 × 3 × 3 Gauss rule		2 × 2 × 2 Gauss rule		2 × 2 × 2 Gauss rule		3 × 3 × 3 Gauss rule	
		σ_z[a]	$\bar{\sigma}_z$[b]	σ_z	$\bar{\sigma}_z$	σ_z	$\bar{\sigma}_z$	σ_z	$\bar{\sigma}_z$	σ_z	$\bar{\sigma}_z$
5	12	1.0320	1.0321	1.0212	1.0206	1.1138	1.1131	1.5468	1.5386	1.4429	1.4287
6	10	1.0321		1.0198		1.1124		1.5303		1.4144	
15	12	0.8477	0.8459	0.8070	0.8047	0.8573	0.8547	1.0821	1.0906	1.1175	1.1297
16	10	0.8441		0.8024		0.8519		1.0991		1.1417	
25	12	0.4021	0.4011	0.4338	0.4339	0.4486	0.4453	0.8350	0.8229	0.6813	0.6655
26	10	0.3999		0.4339		0.4420		0.8114		0.6496	
35	12	0.2885	0.2898	0.2978	0.2997	0.3399	0.3388	0.6007	0.5777	0.5827	0.5492
36	10	0.2909		0.3015		0.3375		0.5547		0.5156	
55	12	0.1780	0.1793	0.1755	0.1773	0.2060	0.2048	0.2728	0.2629	0.2529	0.2103
56	10	0.1805		0.1790		0.2034		0.2527		0.1677	
75	12	0.1336	0.1351	0.1302	0.1322	0.1533	0.1538	0.1347	0.1093	0.0984	0.0621
76	10	0.1366		0.1341		0.1542		0.0837		0.0258	
95	12	0.1604	0.1604	0.1573	0.1581	0.1558	0.1566	0.0520	0.0422	0.0780	0.1040
96	10	0.1608		0.1588		0.1569		0.0323		0.1329	
115	12	0.2411	0.2376	0.2345	0.2303	0.1938	0.1883	0.1936	0.2154	0.2335	0.2613
116	10	0.2323		0.2260		0.1828		0.2372		0.2891	
135	12	0.3394	0.3347	0.3263	0.3225	0.2311	0.2208	0.4606	0.4857	0.3974	0.3115
136	10	0.3299		0.3187		0.2104		0.5107		0.4236	
155	12	0.4713	0.4693	0.4650	0.4635	0.3256	0.3599	0.3021	0.4325	0.3758	0.4231
156	10	0.4652		0.5619		0.3452		0.4028		0.4703	
175	12	0.4809	0.4808	0.4911	0.4915	0.4210	0.3753	0.1751	0.2521	0.4554	0.4028
176	10	0.4805		0.4917		0.3295		0.1291		0.3500	
195	12	0.4380	0.4555	0.4421	0.4595	0.4035	0.4213	0.1546	0.2167	0.1258	0.1919
196	10	0.4729		0.4769		0.4390		0.0786		0.0578	
215	12	0.5218	0.5138	0.5151	0.5159	0.5184	0.4955	0.4064	0.2736	0.4149	0.3705
216	10	0.5017		0.5166		0.4724		0.1408		0.3219	
233	12	0.4979	0.4973	0.5014	0.4955	0.4982	0.4611	0.4706	0.3750	0.4386	0.3050
234	10	0.4967		0.4894		0.4727		0.2793		0.1714	
241	12	0.5179	0.5120	0.5192	0.5123	0.5228	0.5107	0.5924	0.5412	0.6197	0.5486
242	10	0.5060		0.5053		0.4985		0.4899		0.4775	

[a] Stress parallels the axis of the vessel.

[b] Average value.

Table A.12. Stresses on WC-100DD on outside surface at 90° section (internal pressure load = 0.0195 psi)

Element No.	Stress location	Stress (psi)									
		ν = 0.3				ν = 0.4		ν = 0.485			
		2 × 2 × 2 Gauss rule		3 × 3 × 3 Gauss rule		2 × 2 × 2 Gauss rule		2 × 2 × 2 Gauss rule		3 × 3 × 3 Gauss rule	
		σ_x[a]	$\bar{\sigma}_x$[b]	σ_x	$\bar{\sigma}_x$	σ_x	$\bar{\sigma}_x$	σ_x	$\bar{\sigma}_x$	σ_x	$\bar{\sigma}_x$
5	16	0.8420	0.8405	0.8789	0.8782	0.7997	0.7964	0.5766	0.5676	0.6414	0.6334
6	14	0.8390		0.8774		0.7930		0.5584		0.6253	
15	16	0.7996	0.7952	0.7350	0.7287	0.8028	0.7942	0.5886	0.5596	0.5871	0.5467
16	14	0.7907		0.7224		0.7856		0.5304		0.5061	
25	16	0.2601	0.2555	0.2802	0.2749	0.2385	0.2326	-0.0056	0.0141	0.0095	0.0054
26	14	0.2507		0.2695		0.2266		-0.0226		-0.0203	
45	16	0.0099	0.0658	0.0753	0.0701	0.0123	0.0181	-0.4387	-0.4476	-0.4232	-0.4378
46	14	0.0616		0.0649		-0.0237		-0.4563		-0.4523	
65	16	0.0861	0.0834	0.0864	0.0776	0.0461	0.0433	-0.1455	-0.1440	-0.1204	-0.1174
66	14	0.0805		0.0887		0.0404		-0.1424		-0.1144	
85	16	0.1118	0.1099	0.1228	0.1199	0.0932	0.0902	0.1195	0.1103	0.1615	0.1539
86	14	0.1080		0.1169		0.0871		0.1010		0.1462	
105	16	0.1887	0.1893	0.2035	0.2027	0.1716	0.1704	0.2570	0.2505	0.3065	0.2897
106	14	0.1898		0.2017		0.1691		0.2239		0.2728	
125	16	0.3288	0.3351	0.3469	0.3521	0.3069	0.3132	0.3528	0.3434	0.4266	0.4211
126	14	0.3413		0.3571		0.3194		0.3340		0.4156	
145	16	0.4888	0.5020	0.5251	0.5285	0.4745	0.4959	0.5100	0.5544	0.6048	0.6439
146	14	0.5152		0.5419		0.5172		0.5986		0.6829	
165	16	0.7155	0.7237	0.7079	0.7244	0.7716	0.7924	1.0080	1.0944	1.0636	1.1980
166	14	0.7317		0.7408		0.8131		1.1807		1.3323	
185	16	0.8352	0.8451	0.8228	0.8381	0.9009	0.9350	1.2576	1.4208	1.0274	1.0618
186	14	0.8549		0.8533		0.9690		1.5839		1.0961	
205	16	0.8117	0.7827	0.7879	0.7592	0.8856	0.8625	1.2297	1.2643	1.1780	1.2502
206	14	0.7536		0.7303		0.8394		1.2987		1.3223	
224	16	0.6036	0.6256	0.6171	0.6277	0.6123	0.6578	0.7078	0.8259	0.7719	0.7822
225	14	0.6475		0.6383		0.7032		0.9440		0.7923	
233	16	0.5690	0.5683	0.5678	0.5685	0.5844	0.5800	0.6907	0.6626	0.7130	0.7257
234	14	0.5675		0.5691		0.5754		0.6344		0.7384	
241	16	0.5295	0.5318	0.5269	0.5314	0.5346	0.5340	0.5162	0.5293	0.4766	0.5174
242	14	0.5339		0.5358		0.5333		0.5424		0.5582	

[a] Stress parallels the axis of the vessel.

[b] Average value.

Table A.13. Maximum and minimum in-plane principal stresses at 180° section on the inside surface of SH-23DD (internal pressure load = 1.0 psi, $\nu = 0.3$, 2×2×2 Gauss rule)

Element No.	Stress location	σ_{max} (psi)	σ_{min} (psi)
6	10	6.0305	2.4833
18	10	6.7422	3.0821
42	10	7.6039	3.8054
78	10	8.1459	3.9699
114	10	8.6538	3.7802
162	10	9.2734	3.3868
210	10	11.4077	0.8748
258	10	14.6939	−0.4381
306	10	16.5154	−0.4305
354	10	12.7909	1.0477
402	10	9.2781	2.1827
450	10	7.9681	2.0782
494	10	7.3831	2.2969
512	10	7.154	2.7474
519	10	6.3166	2.1642

Table A.14. Maximum and minimum in-plane principal stresses at 180° section on the outside surface of SH-23DD (internal pressure load = 1.0 psi, $\nu = 0.3$, 2×2×2 Gauss rule)

Element No.	Stress location	σ_{max} (psi)	σ_{min} (psi)
6	14	4.3589	2.3642
30	14	3.9761	1.7797
90	14	4.2152	0.9612
102	14	2.6472	−0.4544
150	14	2.5059	−0.5465
198	14	2.7200	−0.1774
246	14	3.2894	−0.0105
294	14	4.5053	1.3972
342	14	6.0364	3.3293
390	14	6.65[illegible]	4.1273
438	14	6.1479	3.0974
483	14	5.3592	1.9921
503	14	4.7998	1.4887
512	14	5.2204	2.3943
519	14	5.4910	2.5993